

2009-12-21

Behavior of Full-Scale Reinforced Concrete Members with External Confinement or Internal Composite Reinforcement under Pure Axial Load

Antonio De Luca

University of Miami, adeluca@miami.edu

Follow this and additional works at: https://scholarlyrepository.miami.edu/oa_dissertations

Recommended Citation

De Luca, Antonio, "Behavior of Full-Scale Reinforced Concrete Members with External Confinement or Internal Composite Reinforcement under Pure Axial Load" (2009). *Open Access Dissertations*. 348.
https://scholarlyrepository.miami.edu/oa_dissertations/348

This Open access is brought to you for free and open access by the Electronic Theses and Dissertations at Scholarly Repository. It has been accepted for inclusion in Open Access Dissertations by an authorized administrator of Scholarly Repository. For more information, please contact repository.library@miami.edu.

UNIVERSITY OF MIAMI

BEHAVIOR OF FULL-SCALE REINFORCED CONCRETE MEMBERS WITH
EXTERNAL CONFINEMENT OR INTERNAL COMPOSITE REINFORCEMENT
UNDER PURE AXIAL LOAD

By

Antonio De Luca

A DISSERTATION

Submitted to the Faculty
of the University of Miami
in partial fulfillment of the requirements for
the degree of Doctor of Philosophy

Coral Gables, Florida

December 2009

©2009
Antonio De Luca
All Rights Reserved

UNIVERSITY OF MIAMI

A dissertation submitted in partial fulfillment of
the requirements for the degree of
Doctor of Philosophy

BEHAVIOR OF FULL-SCALE REINFORCED CONCRETE MEMBERS WITH
EXTERNAL CONFINEMENT OR INTERNAL COMPOSITE REINFORCEMENT
UNDER PURE AXIAL LOAD

Antonio De Luca

Approved:

Antonio Nanni, Ph.D.
Professor of the Civil, Architectural
and Environmental Engineering

Terri A. Scandura, Ph.D.
Dean of the Graduate School

Ronald Zollo, Ph.D.
Professor of Civil, Architectural
and Environmental Engineering

Brian Metrovich, Ph.D.
Assistant Professor of
Civil, Architectural and
Environmental Engineering

Fabio Matta, Ph.D.
Research Assistance Professor of
Civil, Architectural and
Environmental Engineering

Nestore Galati, Ph.D.
Design Engineer
Structural Group
Baltimore, Maryland

DE LUCA, ANTONIO
Behavior of Full-Scale Reinforced Concrete Members
with External Confinement or Internal Composite
Reinforcement under Pure Axial Load.

(Ph.D., Civil Engineering)
(December 2009)

Abstract of a dissertation at the University of Miami.

Dissertation supervised by Professor Antonio Nanni.
No. of pages in text. (178)

The need to satisfy aerospace industry's demand not met by traditional materials motivated researchers and scientists to look for new solutions. The answer was found in developing new material systems by combining together two or more constituents. Composites, also known as fiber reinforced polymers (FRP) consisting of a reinforcing phase (fibers) embedded into a matrix (polymer), offered several advantages with respect to conventional materials. High specific modulus and strength together with other beneficial properties, corrosion resistance and transparency to electrical and magnetic fields above all, made FRP also suitable for use as construction materials in structural engineering. In the early years of the twenty-first century, the publication by the American Concrete Institute (ACI) of design guidelines for the use of FRP as internal reinforcement and for external strengthening of concrete members accelerated their implementation for structural engineering applications. To date, FRP have gained full acceptance as advanced materials for construction and their use is poised to become as routine as the use of conventional structural materials such as masonry, wood, steel, and concrete. However, new concrete columns internally reinforced with FRP bars and FRP

confinement for existing prismatic reinforced concrete (RC) columns have currently important unsolved issues, some of which are addressed in this dissertation defense.

The dissertation is articulated on three studies. The first study (Study 1) focuses on RC columns internally reinforced with glass FRP (GFRP) bars; the second (Study 2) on RC prismatic columns externally confined by means of FRP laminates using glass and glass/basalt fibers; and the third (Study 3) is a theoretical attempt to interpret and capture the mechanics of the external FRP confinement of square RC columns.

Study 1 describes an experimental campaign on full-scale GFRP RC columns under pure axial load undertaken using specimens with a 24 by 24 in. (0.61 by 0.61 m) square cross section. The study was conducted to investigate whether the compressive behavior of longitudinal GFRP bars impacts the column performance, and to understand the contribution of GFRP ties to the confinement of the concrete core, and to prevent instability of the longitudinal reinforcement. The results showed that the GFRP RC specimens behaved similarly to the steel RC counterpart, while the spacing of the ties strongly influenced the failure mode.

Study 2 presents a pilot research that includes laboratory testing of full-scale square and rectangular RC columns externally confined with glass and basalt-glass FRP laminates and subjected to pure axial load. Specimens that are representative of full-scale building columns were designed according to a dated ACI 318 code (i.e., prior to 1970) for gravity loads only. The study was conducted to investigate how the external confinement affects ultimate axial strength and deformation of a prismatic RC column. The results showed that the FRP confinement increases concrete axial strength, but it is more effective in

enhancing concrete strain capacity. The discussion of the results includes a comparison with the values obtained using existing constitutive models.

Study 3 proposes a new theoretical framework to interpret and capture the physics of the FRP confinement of square RC columns subjected to pure compressive loads. The geometrical, physical and mechanical parameters governing the problem are analyzed and discussed. A single-parameter methodology for predicting the axial stress – axial strain curve for FRP-confined square RC columns is described. Fundamentals, basic assumptions and limitations are discussed. A simple design example is also presented.

*To my Mom
for her unconditional love,
support and guidance*

*To my Dad
who gave me the love of science*

*To my Brother
for his friendship*

*To Professor Nanni
who gave me a chance
and believed in me*

Acknowledgements

These few lines are not enough to pay tribute to all the individuals who, with their support and cooperation, have contributed to the completion of this dissertation. But, at least, they give me the opportunity to express to them my sincere gratitude and heartfelt thanks.

First of all, I would like to thank my advisor, Dr. Antonio Nanni, who gave me a chance and believed in me. His teachings will be engraved in my mind forever. I can only hope one day to be for someone what he has been for me.

Many thanks go to Dr. Ronald Zollo, Dr. Brian Metrovich, Dr. Fabio Matta and Dr. Nestore Galati for the kindness of being on my committee.

Special thanks go to Dr. Fabio Matta whose continuous support, encouragement and guidance have made an important difference in my work, and to Dr. Nestore Galati who provided thoughtful advice and help throughout.

I am very grateful to Dr. Ronald Zollo and Dr. Carol Hays whose experience and knowledge contributed to make this work much better; and to Dr. Gian Piero Lignola and Dr. Andrea Prota for their “overseas” support and precious assistance.

A special recognition for the assistance in planning and conducting the tests is extended to the Fritz Engineering Laboratory at Lehigh University, in particular to Mr. Frank Stokes and Mr. Gene Matlock; and to the Building and Fire Research Laboratory at the

National Institute for Standards and Technology (NIST), in particular to Mr. Steven Cauffman and Mr. Frank Davis.

The financial support of the NSF Industry/University Cooperative Research Center for “Repair of Buildings and Bridges with Composites” (RB²C) at the University of Miami, and of the “REte dei Laboratori Universitari di Ingegneria Sismica” (RELUIS) at the University of Naples “Federico II” is acknowledged. The assistance of Hughes Brothers, Inc. and Pultrall, Inc. in supplying the FRP bars; and of Mapei S.p.A. and Fyfe Co. LCC in providing the FRP sheet is also acknowledged.

Sincere thanks go to Rossella Ferraro for being a good friend and for sharing with me most of this experience; to Derek Schesser for his priceless help in the laboratory and in the field; to Fabio Nardone for his friendship and the work enjoyed together; to Ms. Carole Kavooras for her maternal support; to Christian Aquino, Francisco De Caso and Matthew Trussoni for sharing with me time, knowledge and experience; to David Gerber, Marco Osorio, Mikel Solupe for their kind friendship and cooperation; Paul Lopez, Alexander Suma and Annalisa Napoli for their support.

Many thanks also go to my friend Francesco Travascio; to Mr. David Poole for his friendship; to Dr. Fernando Tinoco for sharing with me his experience and knowledge during our chats at the Rat; to Layla Siegel; to all my great friends who contributed to make this dream come true: Janelle Hygh, Patrick Kaimrajh, Omar De Leon, Vanessa Garcia, Cynthia Donna, Cristina Ortega, Daniela Delgado, Jose Cueto, Monica Maher, Thomas Kiger, Joseph Paquette, and Seana Campbell; to Sandra and Leslie Space for

friendship; to my best friend Vittorio Pasquino; to my dear cousin Mariarosa Libonati; to Spartacus for his company during the dissertation write-up.

Last, but not least, I am greatly indebted to my Parents, Angela and Giuseppe, and to my Brother, Gianluca, for their love and guidance without which I would never have made it through.

Table of Contents

List of Tables	ix
----------------------	----

List of Figures	x
-----------------------	---

Chapters:

Chapter 1: Introduction	1
-------------------------------	---

Chapter 2: Study 1 – Behavior of Full-Scale Glass Fiber Reinforced Polymer Reinforced Concrete Columns under Axial Load	8
---	---

Chapter 3: Study 2 – Structural Evaluation of Full-Scale Fiber Reinforced Polymer Confined Reinforced Concrete Columns	36
--	----

Chapter 4: Study 3 – Single-Parameter Methodology for the Prediction of the Stress-Strain Behavior of Fiber Reinforced Polymer Confined Reinforced Concrete Square Columns	79
--	----

Chapter 5: Conclusions	107
------------------------------	-----

Appendices:

Appendix 1: Study 1 and Study 2 – Specimen Preparation, Instrumentation and Test Setup	113
--	-----

Appendix 2: Study 1 – Photographs of Failed Specimens	127
---	-----

Appendix 3: Study 1 – News Releases	132
---	-----

Appendix 4: Study 2 – Photographs of Failed Specimens	133
---	-----

Appendix 5: Study 3 – Example Algorithm	145
---	-----

Appendix 6: Study 2.1 – Structural Evaluation of GFRP-Confined Reinforced Concrete Hollow Columns	147
---	-----

Appendix 7: Study 2.2 – Structural Evaluation of GFRP-Confined Reinforced Concrete Wall-like Columns	160
Bibliography	172

List of Tables

Table 1: Test matrix	27
Table 2: Test results	28
Table 3: Strain on longitudinal bars and concrete at peak load	28
Table 4: Test matrix	61
Table 5: Concrete nominal strength.....	62
Table 6: FRP system properties	63
Table 7: Test results	64
Table 8: Example of design table.....	101
Table A - 1: Test matrix.....	152
Table A - 2: GFRP system properties.....	152
Table A - 3: Test results.....	153
Table A - 4: Test matrix.....	164
Table A - 5: GFRP system properties.....	164
Table A - 6: Test results.....	165

List of Figures

Fig. 1: Reinforcement layout of Specimen S-16 (a), A-12 and B-12 (b), and A-3 and B-3 (c); cross-section layout for all specimens (d); details of Bar A (e) and Bar B (f).....	29
Fig. 2: Test setup.....	30
Fig. 3: Specimen S-16: normalized axial stress-normalized axial deformation response where the thick line shows the envelope curve (a); photograph of failed specimen (b); close-up of buckled steel bars (c).....	31
Fig. 4: Specimen A-12: normalized axial stress-normalized axial deformation response where the thick line shows the envelope curve (a); photograph of failed specimen (b); close-up of buckled GFRP bars (c).....	32
Fig. 5: Specimen B-3: normalized axial stress-normalized axial deformation response where the thick line shows the envelope curve (a); photograph of failed specimen (b); close-up of failed GFRP tie and bulged bar (c).	33
Fig. 6: Normalized axial stress-axial deformation.....	34
Fig. 7: Volumetric strain-axial strain.....	35
Fig. 8: Dilation versus axial strain.....	35
Fig. 9: Reinforcement layout for series S-1.....	65
Fig. 10: Reinforcement layout for series R-1.....	66
Fig. 11: Reinforcement layout for series R-0.5.....	67
Fig. 12: Normalized concrete axial stress vs. axial deformation (series S-1). Failed specimens S-1-control and S-1-8H are also showed.....	68
Fig. 13: Normalized concrete axial stress vs. axial deformation (series R-1). Failed specimens R-1-control and R-1-8H are also showed.....	69
Fig. 14: Normalized concrete axial stress vs. axial deformation (series R-0.5). Failed specimens R-0.5-control, R-0.5-5GB and R-0.5-8H are also showed.....	70
Fig. 15: Volumetric strain-axial strain relationships [series S-1 (a) and R-0.5 (b)].	71

Fig. 16: Dilation ratio-axial strain relationships [series S-1 (a) and R-0.5 (b)].	72
Fig. 17: Dilation ratio-axial strain relationships [specimens S-1-control (a) and R-0.5-control (b)].	73
Fig. 18: Dilation ratio-axial strain relationships [specimens S-1-8H (a) and R-0.5-8H (b)].	74
Fig. 19: Change in volume of representative one-quarter unit element for Specimen S-1-8H at peak load (a) and at failure (b) and Specimen R-0.5-8H at peak load (c) and at failure (d).	75
Fig. 20: Typical volumetric strain – normalized axial stress relation for FRP-confined prismatic concrete column.	76
Fig. 21: Predicted concrete axial strength enhancement based on f_c and strength of control column (square columns).	77
Fig. 22: Predicted concrete axial strength enhancement based on f_c and strength of control column (rectangular columns).	78
Fig. 23: Experimental transverse and diagonal dilation ratio – axial strain relationship (a). Change in volume of Specimen S-1-8H at peak load (b) and at failure (c).	102
Fig. 24: Theoretical dilation ratio – axial strain curves.	103
Fig. 25: Experimental versus theoretical transverse dilation ratio for specimen S-1-2GB.	104
Fig. 26: Qualitative cross-section deformed shape at different levels of axial strain.	105
Fig. 27: Experimental curves for specimen S-1-control (a), S-1-2GB (b) and S-1-8H (b) compared with the theoretical ones, for α equal to 0, 0.333 and 0.3, respectively.	106
Fig. A - 1: Casting of a specimen.	114
Fig. A - 2: Cured specimens.	114
Fig. A - 3: Preparation of the GFRP cages (a-d).	115
Fig. A - 4: Chamfering of the corners: grinding of the corner (a); corner before chamfering (b); corner after chamfering (c).	116

Fig. A - 5: Wrapping of the column specimens: cutting of the fiber sheet (a); installation of the fiber sheet (b-d).....	117
Fig. A - 6: Specimen preparation.....	118
Fig. A - 7: Type of fibers: Glass A (a); Glass B (b); Hybrid (c).....	119
Fig. A - 8: Sketch illustrating the position of the vertical LVDTs (all specimens in Study 1 and Study2).	120
Fig. A - 9: Sketch illustrating the position of the horizontal LVDTs: all specimens in Study 1 and control specimens in Study2 (a); confined specimens in Study 2 (b).....	120
Fig. A - 10: Sketch illustrating the position of the strain gauges attached to the vertical bars at the level of the mid-height cross-section: all specimens in Study 1 and S-1 and R-1 specimens in Study2 (a); R-0.5 specimens in Study 2 (b).	121
Fig. A - 11: Sketch illustrating the position of the strain gauges attached to the ties at the level of the mid-height cross-section: all specimens in Study 1 and S-1 and R-1 specimens in Study2 (a); R-0.5 specimens in Study 2 (b).	121
Fig. A - 12: Testing equipment at the Fritz Laboratories.	122
Fig. A - 13: Test setup: column specimen centered in the machine (a); column specimen centered and plumbed (b); hydro-stoning of the bottom surface (c); hydro-stoning of the top surface (d).	123
Fig. A - 14: Testing equipment at the NIST Laboratories.	124
Fig. A - 15: Test setup: grouting of top (a) and bottom (b) surface (NIST Laboratory).	125
Fig. A - 16: Final setup: Fritz Laboratory (a); NIST Laboratory (b).	126
Fig. A - 17: Failure of Specimen S-16 (a-d).	127
Fig. A - 18: Failure of Specimen A-12 (a-d).	128
Fig. A - 19: Failure of Specimen B-12 (a-d).....	129
Fig. A - 20: Failure of Specimen A-3 (a-d).	130
Fig. A - 21: Failure of Specimen B-3 (a-d).....	131
Fig. A - 22: Failure of Specimen S-1-control (a-c).....	133

Fig. A - 23: Failure of Specimen S-1-5GA (a-c).	134
Fig. A - 24: Failure of Specimen S-1-2GB (a-d).	135
Fig. A - 25: Failure of Specimen S-1-8H (a-d).	136
Fig. A - 26: Failure of Specimen R-1-control (a-b).	137
Fig. A - 27: Failure of Specimen R-1-5GA (a-d).	138
Fig. A - 28: Failure of Specimen R-1-8H (a-d).	139
Fig. A - 29: Failure of Specimen R-0.5-control (a-d).	140
Fig. A - 30: Failure of Specimen R-0.5-5GA (a-d).	141
Fig. A - 31: Failure of Specimen R-0.5-2GB (a-d).	142
Fig. A - 32: Failure of Specimen R-0.5-5GB (a-d).	143
Fig. A - 33: Failure of Specimen R-0.5-8H (a-d).	144
Fig. A - 34: Algorithm to calculate the ultimate concrete axial strain (Part 1 of 2).	145
Fig. A - 35: Algorithm to calculate the ultimate concrete axial strain (Part 2 of 2).	146
Fig. A - 36: Axial load vs. axial deformation diagram: Specimen HR-control.	154
Fig. A - 37: Axial load vs. axial deformation diagram: Specimen HR-5GA.	154
Fig. A - 38: Axial load vs. axial deformation diagram: Specimen HR-8GA.	155
Fig. A - 39: Photographs of failed Specimen HR-control (a-c).	156
Fig. A - 40: Photographs of failed Specimen HR-5GA (a and b).	157
Fig. A - 41: Photographs of failed Specimen HR-8GA (a and b).	158
Fig. A - 42: Normalized axial stress vs. axial deformation response of all specimens. .	159
Fig. A - 43: Axial load vs. axial deformation diagram: Specimen WL-control.	166
Fig. A - 44: Axial load vs. axial deformation diagram: Specimen WL-5GA.	166
Fig. A - 45: Axial load vs. axial deformation diagram: Specimen WL-8GA.	167

Fig. A - 46: Photographs of failed Specimen WL-control (a-c). 168

Fig. A - 47: Photographs of failed Specimen WL-5GA (a and b). 169

Fig. A - 48: Photographs of failed Specimen WL-8GA (a and b). 170

Fig. A - 49: Normalized axial stress vs. axial deformation response of all specimens. . 171

Chapter 1: Introduction

Background

Over the second half of the twentieth century, the issue of the deterioration due to chloride-ion induced corrosion on reinforced concrete (RC) bridge decks and the market demand for internal reinforcement that provides electromagnetic insulation for specific constructions (such as facilities for special medical equipments, seawall construction, substation reactor bases, airport runways and electronic laboratories) made desirable the development of bars constructed of non corrosive and insulating materials (ACI 440.1R-06 2006).

During the same period, many existing RC buildings and bridges were found to be in need of repair and strengthening due to several causes, among them the deterioration caused by environmental effects such as corrosion initiated by water and salt solutions, damages and change in use of the structures, higher load capacity demand as a consequence of more severe code requirements, and higher strength and ductility demand to correct design or construction errors (ACI 440.2R-08 2008).

The need to satisfy aerospace industry demand not met by traditional materials induced researchers and scientists to look for new solutions. The answer was found in developing new material systems by combining together two or more constituents. Composites – also

known as fiber reinforced polymers (FRP) – consisting of a reinforcing phase (fibers) embedded into a matrix (polymer), offered several advantages with respect to conventional monolithic materials (Kaw 2005). High specific modulus and strength together with other beneficial properties such as corrosion resistance and transparency to electromagnetic fields, made FRP also suitable for use as construction materials in structural engineering (Nanni 1993).

During the 1980s, the use of FRP bars as internal reinforcement in concrete members became particularly attractive to improve the durability of a structure (Nanni 2001). However, given the intuitive unsuitability of FRP bars to compressive loads, because of the anisotropic and non-homogeneous nature of FRP materials, their use was limited to members subjected only to flexure and shear (ACI 440.1R-06 2006).

At the same time, strengthening of concrete members with externally bonded FRP laminates or near surface mounted (NSM) bars gained relevant attention. FRP were used for strengthening of bridge girders and piles, parking garages, office buildings and silos (Nanni 2001). In particular, the external confinement of concrete columns became one of the most attractive applications of FRP laminates for repair and upgrading. This new technology found in the ease and flexibility of installation the most remarkable driver for its development and became soon a competitive option to steel jackets and welded wire fabrics (Nanni and Bedford 1995).

In FRP-confined concrete, the interaction between the two materials allows for the enhancement of concrete strength and deformability. Several experimental studies have

been carried out and several analytical models have been proposed to describe the behavior of FRP-confined concrete. These models satisfactorily capture the mechanics of the phenomenon for circular columns. The same cannot be said for prismatic¹ columns, for which these models do not converge to the same predicted values, and their validity for full-scale columns still has to be proven (Rocca et al. 2008).

In the early years of the twenty-first century, the publication by the American Concrete Institute (ACI) of design guidelines for the use of FRP as internal reinforcement and for external strengthening of concrete members accelerated their adoption. To date, FRP systems have gained considerable acceptance in construction, and their use is poised to become as routine as the use of conventional structural materials such as masonry, wood, steel, and concrete (Bank 2006).

Today, the design of new concrete columns internally reinforced with FRP bars and the mechanics of FRP confinement of existing prismatic RC columns are still important unsolved issues to be addressed.

Dissertation outline

The dissertation is articulated on three studies. The first study (Study 1) focuses on RC columns internally reinforced with glass FRP (GFRP) bars; the second (Study 2) on RC

¹ A “prismatic” cross-section is herein defined as a planar convex cross-section generated by a chain of straight-line segments.

prismatic columns externally confined by means of FRP laminates using glass and glass-basalt fibers; and the third (Study 3) is a theoretical attempt to interpret and capture the mechanics of the external FRP confinement of square RC columns.

Study 1 describes an experimental campaign on full-scale GFRP RC columns under pure axial load undertaken using specimens with a 24 by 24 in. (0.61 by 0.61 m) square cross section. The study produces new experimental evidence to underpin rational design methodologies and to eventually incorporate this solution into current ACI design guidelines.

Study 2 presents a pilot research that includes laboratory testing of full-scale square and rectangular RC columns externally confined with glass and basalt-glass FRP laminates and subjected to pure axial load. Specimens that are representative of full-scale building columns were designed according to a dated ACI 318 code (i.e., prior to 1970) for gravity loads only.

Study 3 discusses a single-parameter methodology for predicting the axial stress–axial strain curve of a square concrete column confined with FRP. Methodology fundamentals, assumptions and limitations are presented and discussed.

Tests done on rectangular hollow-core columns and wall-like columns externally confined by means of GFRP laminates and subjected to pure axial load only are described in the Appendix 6 and 7, respectively.

Objectives

Study 1 aims to:

1. investigate whether the compressive behavior of longitudinal GFRP bars impacts the column performance;
2. understand the contribution of GFRP ties to confine the concrete core and prevent instability of the longitudinal reinforcement; and
3. assess the equivalence of column performance when different GFRP bars of comparable quality are used.

Design-related issues, such as creep and fire rating, are not part of this study.

Study 2 aims to:

1. explore the effectiveness of the external FRP confinement on the axial strength and axial deformation of a prismatic RC column under pure compressive load;
2. evaluate whether the confinement is able to prevent and delay the instability of the longitudinal bars;
3. understand limitations due to the cross-sectional shape; and
4. provide more experimental evidence to remedy the lack thereof in the literature.

Study 3 aims to:

1. propose a new theoretical framework to analyze the behavior of FRP-confined RC square columns;

2. introduce an innovative methodology to predict the axial stress–axial strain diagram for concrete to be used for developing strength interaction (P-M) diagrams.

Research significance

The use of FRP reinforcement is particularly attractive for structures that operate in aggressive environments, such as in coastal regions, or for buildings supporting magnetic resonance imaging (MRI) units or other equipment sensitive to electromagnetic fields. Thus far, few studies have been devoted to laboratory experiments on full-scale concrete columns reinforced with FRP bars. Because of the scarcity of relevant research outcomes and experimental evidence, current guidelines and codes of practice such as in the USA, Canada and Italy, with the only exception of Japan, do not recommend to rely on FRP bars as longitudinal reinforcement in columns nor as compression reinforcement in flexural members.

Confinement effectiveness in increasing concrete strength and ultimate deformation has been experimentally proven since the late 1980s. Confinement of prismatic columns still enhances concrete strength and ultimate strain, but its effectiveness is not as tangible as that of a circular cross-section. Several experimental studies have been carried out on FRP-confined RC prismatic columns in the past years, and several analytical models have been proposed. These models, however, do not converge to the same predicted values, and their validity for full-scale columns still has to be proven.

Full-scale experiments are limited by high cost and low availability of high-capacity testing equipment. Most of the time, the design of real concrete structures relies on the extrapolation from experimental results of laboratory tests conducted on scaled sample structures. Quasibrittle failures of concrete structures exhibit a large statistical scatter (Bažant and Yavari 2005). Full-scale experiments are, therefore, critical to ensure that design equations are truly representative of the actual behavior of full-scale members.

The nominal concrete compressive strength does not represent the actual strength of the concrete in the test columns due to several phenomena: the difference in cross-section sizes of the columns and the companion cylinders; the partial confinement provided by the ties; the fact that bars promote axial splitting cracks along the bar surface; and the brittle or quasi-brittle failure which is governed mainly by the rate of release of the stored-strain energy (Bažant and Kwon 1994). These phenomena are influenced by the size of the column. In particular, tensile brittleness is characterized by concentration of deformation into a narrow zone of dimensions comparable with the dimension of the aggregate size. The energy accumulated in the structure is dissipated through these narrow zones. Differently, compression brittleness develops in areas of dimensions comparable to the dimensions of the structure (Nemecek and Bittnar 2003).

The full-scale of the column specimens is a key novelty of this research.

Chapter 2: Study 1 – Behavior of Full-Scale Glass Fiber Reinforced Polymer Reinforced Concrete Columns under Axial Load

Background

Glass fiber reinforced polymer (GFRP) bars are a competitive option as reinforcement in reinforced concrete (RC) members subjected to flexure and shear due to their compelling physical and mechanical properties, corrosion resistance and electromagnetic transparency above all. The use of GFRP reinforcement is particularly attractive for structures that operate in aggressive environments, such as in coastal regions, or for buildings that host magnetic resonance imaging (MRI) units or other equipment sensitive to electromagnetic fields. Nonetheless, the behavior of GFRP bars as longitudinal reinforcement in compression members is still a relevant issue to be addressed. Different modes of failure (transverse tensile failure, fiber microbuckling or shear failure) may characterize the response of the fiber reinforced polymer (FRP) bars in compression, depending on the type of fiber, fiber volume fraction, and type of resin (ACI 440.1R-06). Testing of FRP bars in compression is typically complicated by the occurrence of fiber microbuckling due to the anisotropic and non-homogeneous nature of the FRP material, and can lead to inaccurate measurements (Choo et al. 2006). Therefore, standard test methods are not yet established (ACI 440.1R-06). For the case of GFRP bars, reductions in the compressive strength and elastic modulus by up to 45% and 20% with respect to

the values in tension, respectively, have been reported (Mallick 1988; Wu 1990). The reduced compressive strength and stiffness of FRP bars contribute to make FRP RC columns more susceptible to instability. Because of the scarcity of relevant research outcomes and experimental evidence, the American Concrete Institute (ACI) “Guide for the Design and Construction of Structural Concrete Reinforced with FRP Bars” (ACI 440.1R-06) recommends not to rely on FRP bars as longitudinal reinforcement in columns nor as compression reinforcement in flexural members.

Alsayed and others (1999) investigated the effect of replacing longitudinal steel bars (reinforcement ratio of 1.07%) and ties with an equal amount of GFRP bars and ties. Based on the results of tests performed on $17.7 \times 9.8 \times 47.2$ in. ($450 \times 250 \times 1200$ mm) columns under concentric loads, it was reported that replacing longitudinal steel bars with GFRP bars by maintaining the same reinforcement ratio reduced the capacity by 13%, irrespective of the type of ties (steel or GFRP). Replacing only the steel ties with GFRP ties reduced the capacity by 10%, with no influence on the load-deformation response up to approximately 80% of the ultimate capacity. Mirmiran and his group (2001) conducted a parametric study for the analysis of slender FRP RC columns. It was shown that even though FRP RC columns are more susceptible to instability failure than steel RC columns, the design practice of using moment magnification factors is also applicable to FRP RC columns. In another research program by Mirmiran (1998), it was concluded that the slenderness limits should be lowered when using longitudinal FRP reinforcement, when maintaining a minimum reinforcement ratio of 1%.

The ACI Building Code (ACI 318-08) bases the axial load capacity equation and the tie

requirements for steel RC columns on research carried out at Lehigh University and the University of Illinois in the early 1930's (Slater and Lyse 1931a; Slater and Lyse 1931b; Slater and Lyse 1931c; Lyse and Kreidler 1932; Lyse 1933; Richart 1933). The maximum concrete stress was found to be about 85% of the compressive strength of a 6 in. diameter by 12 in. (152.4 by 308.4 mm) concrete cylinder, at a strain where the yield stress of the reinforcing steel, f_y , was attained (McGregor and Wight 2004). The nominal capacity of an axially loaded RC column, P_n , was defined as the sum of the forces carried by the concrete, P_c , and the steel, P_s , as given by the following equation:

$$P_n = P_c + P_s = 0.85f'_c \cdot (A_g - A_s) + f_y \cdot A_s \quad (1)$$

where A_g is the gross cross sectional area of the column, A_s is the area of the longitudinal steel reinforcement, and f'_c is the nominal compressive strength of the concrete. ACI 318-08 requires that the vertical spacing of ties does not exceed 16 longitudinal bar diameters to prevent bar buckling (Bresler and Gilbert 1961; Pfister 1964; Hudson 1966), 48 tie diameters to ensure sufficient tie area to restrain the lateral displacement of the longitudinal bars (Bresler and Gilbert 1961; Pfister 1964), or the least lateral dimension of the column to develop the maximum strength of the concrete core (Bresler and Gilbert 1961). Experimental studies performed between the late 1950's and early 1960's showed that ties provide transverse constraint to the concrete core, causing the column to fail in a more gradual manner than without ties (Pfister 1964). It was also found that ties offered sufficient restraint against buckling of the longitudinal bars up to compressive failure of the concrete, with negligible influence on the ultimate load (Hudson 1966).

In order to focus on the compressive behavior of GFRP bars, the research presented herein addresses full-size, tied RC columns subjected to pure axial loads and sufficiently stocky to ignore slenderness effects. The condition of pure axial load is atypical for RC columns given that they always transmit axial compressive loads together with bending moments, but this condition represents the first step to understand whether or not GFRP bars can be used as internal reinforcement for RC columns. In particular, this study aims at: (1) investigating the impact of the compressive behavior of longitudinal GFRP bars on strength and failure mode; (2) investigating the contribution of GFRP ties to concrete confinement and to prevent instability of the longitudinal reinforcement; and (3) assessing the equivalence of column performance when different GFRP bars of comparable quality are used.

An important novelty is the size of the column specimens, which provides the opportunity to investigate and validate the technology on the basis of experimental evidence indicative of real case scenarios. Few experimental works have studied the influence of the size of RC columns on their structural behavior. Bažant and Kwon (1994) tested a total of 26 scaled RC columns of different sizes under eccentric axial load. The existence of a size effect on the ultimate loads was observed that was consistent with the fracture mechanics based mathematical formulation derived by Bažant (1984a). Sener and others (2004) tested a total of 27 square RC columns with different scales and slenderness ratios under concentric axial loads. The largest cross section had dimensions 7.9 in. \times 7.9 in. (200 \times 200 mm), and reinforcement ratio of 4.91%. It was found that a reduction in strength occurred at increasing size and slenderness, which was in good

agreement with Bažant's size effect law (1984a). Nemecek and Bittnar (2004) tested square RC columns of three different scales, with maximum size of $11.8 \times 11.8 \times 78.7$ in. ($300 \times 300 \times 2000$ mm) and reinforcement ratio of 2.18%, under eccentric axial load. No significant size effect was observed in the ultimate capacity. The current ACI design specifications for RC columns (ACI 318-08) neglect any size effect on the nominal axial strength.

Except for the Japan Society of Civil Engineers (Sonobe et al 1997b) which established a design procedure specifically for the use of FRP reinforcement in RC columns, current guidelines and codes of practice such as in the USA (ACI 440.1R-06), Canada (CAN/CSA-S6-02) and Italy (CNR-DT 203/2006), do not recommend the use of FRP bars as reinforcement in compression members. In this study, the behavior of GFRP bars in RC columns is investigated based on laboratory tests on full-scale specimens. Although generally limited by high costs and availability of high-capacity testing machines, full-scale experiments are critical to validate the technology, and to produce compelling evidence to underpin rational design methodologies.

Experimental program

The experimental program included testing of full-scale GFRP and steel RC columns under pure axial load. The specimens had a square cross-section with 24 in. (0.61 m) sides, and length of 10.0 ft (3.0 m). The test matrix is shown in Table 1. Two different types of GFRP bars and ties were used and are herein denoted as Bar A and Bar B. Both

bar types have the same nominal cross section and different surface preparation: deformed shape using helicoidal wraps for Bar A [Fig. 1 (e)], and sand coating for Bar B [Fig. 1(f)]. Column specimens were cast at a precast plant located in Miami (Fig. A - 1, Appendix 1) and let cure at the South Campus of the University of Miami (Fig. A - 2, Appendix 1). The GFRP bar cages were assembled at the Structural Laboratory of the Civil, Architectural and Environmental Engineering of the University of Miami (Fig. A - 3, Appendix 1).

Specimen design

Five specimens were tested: one benchmark steel RC column, and four GFRP RC columns. The GFRP RC specimens were subdivided into two sets of two, each set identical to the other but using Bar A and Bar B, respectively. The purpose of the duplication is to show that GFRP bars of comparable quality, but from different manufacturers, produce similar responses.

The steel RC column had the minimum amount of longitudinal reinforcement, and the minimum tie cross sectional area at the maximum spacing mandated by ACI 318-08 in Section 10.9.1 and Section 7.10.5.2, respectively. In particular, the total area of longitudinal bars was taken as 1.0% of the gross section area, A_g , using eight No. 8 (25.4 mm diameter) bars; No. 4 (12.7 mm diameter) ties were used, spaced at 16 in. (406 mm) on center (which corresponds to the requirement to prevent bar buckling). The same amount of longitudinal reinforcement was used for all the GFRP RC specimens. The same bar size was used for the GFRP ties, with the spacing being reduced to 12 in. (305

mm) and 3 in. (76 mm). The 12 in. (305 mm) spacing was defined to prevent buckling of the longitudinal bars, whereas the 3 in. (76 mm) spacing was selected as the minimum practical spacing.

Fig. 1a-d shows the reinforcement layouts. The cross section layout is identical for all the specimens. Two No. 4 (12.7 mm diameter) cross-ties were used to provide additional lateral support for the longitudinal bars. Since closed loop GFRP tie cannot be manufactured, the GFRP ties were made by assembling pairs of C-shaped No. 4 bars, and were staggered to avoid having the overlapped legs on the same side for two consecutive layers. No. 4 (12.7 mm diameter) steel ties spaced at 2 in. on center (50.8 mm) were used at the two ends of the specimens to prevent premature failures due to the concentration of compressive stresses.

Materials

A nominal 5,000 psi (34.5-MPa) concrete was used. The specimens were cast one at a time using different concrete batches. The average concrete strength for each batch was based on cylinder samples. The average concrete compressive strength, f_c , and standard deviation for each specimen, based on the results of compression tests on six 6 in. diameter by 12 in. (150 by 304 mm) cylinder samples per ASTM C 39, are reported in the second column of Table 1. ASTM Grade 60 steel bars and ties were used for Specimen S-16. The mechanical properties of the GFRP bars were provided by the manufacturers. Bar A had an average ultimate tensile strength of 88.2 ksi (608 MPa), strain of 1.38 %, and modulus of elasticity of 6,405 ksi (44.2 GPa). Bar B had an average

ultimate tensile strength of 103.3 ksi (712 MPa), strain of 1.60 %, and modulus of elasticity of 6,440 ksi (44.4 GPa). The ultimate tensile strain and the tensile strength reported by the manufacturers were defined as the mean value of a sample of test specimens minus three times the standard deviation, while the tensile modulus of elasticity was taken equal to the mean value of the same sample of test specimens.

Test setup and procedure

The tests were conducted using a 5 million lbf (22,241 kN) testing machine. When ready to be tested, the column specimen was raised to a vertical position with the use of a crane and wheeled to the machine on a pallet jack. Once placed in the machine, the specimen was hung to the head of the machine. Special care was taken that the column specimen was directly at the center of the machine and was plumb. In order to ensure uniformity of the applied load, bottom and top surfaces of the column specimens were hydro-stoned. As each specimen was hung and centered under the crosshead of the machine, a thin layer of hydro-stone grouting paste was cast on the base platen and below the specimen. Then, the specimen was lowered and placed on the hydro-stone grout layer. Another hydro-stone layer was cast on the top surface of the specimen, and a compressive load of about 10 kips (44.5 kN) was applied to allow the hydro-stone to set.

A photograph of the test setup is shown in Fig. 2. Several strain gauges were mounted onto the internal reinforcement prior to casting of the concrete, and onto the concrete surface before testing. One strain gauge was attached on each longitudinal bar at the level of the mid-height cross section and a number of five strain gages was mounted onto

either the steel tie or the GFRP C-shaped bars located at mid-height of the column specimen. A total of eight linear variable differential transformer (LVDT) displacement sensors were used. Four vertical LVDTs (V1 through V4) were used to measure axial deformations, and four in-plane LVDTs (H1 through H4) were mounted at the level of the mid-height cross section to measure transverse deformations at the center of each column side. The load was applied concentrically in displacement control mode at a rate of 0.020 in/min (0.51 mm/min). The loading was conducted in either five or six cycles with increments of 500 kips (2,225 kN). Upon reaching 75% of the expected maximum capacity, the displacement rate was reduced to 0.012 in/min (0.30 mm/min) in order to increase the resolution of the post-peak measurement dataset. Each test lasted about 5 hours.

Experimental results and discussion

Strength and failure modes

The GFRP RC specimens behaved similarly to the benchmark steel RC specimen. Failure typically initiated with vertical cracks followed, first, by lateral deflection of the longitudinal bars contributing to the splitting of the concrete cover and, then finally, by crushing of the concrete core and buckling of the longitudinal bars.

Specimen S-16 — The peak load was attained when the average axial stress (defined as the ratio between the applied load and the gross cross sectional area) was equal to 90.4%

of the average concrete compressive strength. Fig. 3a plots the normalized axial stress (defined as the ratio between the average axial stress and the average concrete compressive strength from cylinder tests) versus the axial deformation normalized with respect to the axial deformation, ϵ_{peak} , recorded when the peak load, P_{peak} , was reached. The axial deformation is rendered as the average of the four measurements from the vertical LVDTs. The load stabilized at the level of the peak load before it suddenly dropped. Cracking of the concrete was observed before the concrete cover split and the longitudinal bars buckled. The ultimate (post-peak) axial deformation recorded, ϵ_u , was about 135% the value at peak load, while the load dropped to 70% of the peak load. The failure was brittle and occurred at the center of the upper half of the column specimen. Crushing of the concrete core and buckling of the longitudinal bars are documented in Fig. 3b and Fig. 3c.

Specimens A-12 and B-12 — The GFRP RC specimens with 12 in. (305 mm) tie spacing exhibited the same behavior as the steel RC counterpart. When the peak load was reached, the normalized axial stress was 93.2% and 85.9% for A-12 and B-12, respectively. In both cases failure was sudden and accompanied by an explosive noise. Fig. 4a shows the normalized axial stress-normalized axial deformation plot for Specimen A-12. Once the peak load was attained, the load dropped almost instantly without early warning, as no cracking of the concrete was observed until the final crushing. The failure occurred at the entire lower half of the specimen, as shown in Fig. 4b. Fig. 4c shows a close-up photograph of the failure area: the concrete cover is completely separated, and the longitudinal GFRP bars are buckled and frayed.

Specimens A-3 and B-3 — Upon attaining the peak load level, the GFRP RC specimens with smaller tie spacing experienced an increase in axial deformation without crushing of the concrete core, due to the confining action exerted by the closely spaced ties. The normalized axial stress at the peak was 89.0% and 91.1% for A-3 and B-3, respectively. The normalized axial stress-normalized axial deformation plot for Specimen B-3 is shown in Fig. 5a. Failure occurred as the fifth load-unload cycle was being repeated, at a smaller load than the peak load in the previous cycle. The load decreased steadily with increasing axial deformation. The test was halted when the load decreased to about 50% of the peak load, and the axial deformation reached a value twice that measured at peak load. Fig. 5b shows a photograph of failed specimen. The photograph in Fig. 5c was taken after removing the concrete cover, and shows a close-up of a failed GFRP tie and a bulged longitudinal bar.

Fig. 6 compares the response of all specimens in terms of normalized axial stress and deformation. Each curve is the envelope of the entire load-unload cycles imparted. The initial slope is identical for all the curves. The GFRP specimens exhibit a gradual decrease in stiffness as the load reaches about 60% of the peak load, whereas for the steel RC specimen (S-16) the stiffness starts decreasing as the load reaches approximately 80% of its peak. The axial deformations measured in correspondence to the peak loads were similar for all the specimens, ranging between 0.26 and 0.32 in. (6.60 and 8.13 mm). For all specimens, when the peak load was attained, the average axial stress ranged between 85.9% and 93.2 % of the average concrete strength.

Influence of longitudinal bars

Table 2 reports the following results for each specimen: average concrete compressive strength, f_c , and standard deviation; peak load, P_{peak} ; axial deformation at peak, Δ_{peak} ; axial deformation when the peak load is reached, Δ_u ; average vertical strain measured in the longitudinal reinforcement at peak, $\varepsilon_{bar,peak}$; load carried by the reinforcement, P_{bar} (computed by multiplying the area of longitudinal reinforcement by the average strain and modulus of elasticity of the bar material); load carried by the concrete (computed as the difference between the peak load and the load carried by the reinforcement) and normalized with respect to the net area of concrete multiplied by the average concrete compressive strength, $(P_{peak} - P_{bar}) / (f_c A_c)$; ratio between the load carried by the reinforcement and the peak load, P_{bar}/P_{peak} . In all the columns, the concrete compressive stress at peak was close to $0.85 f_c$, which is the value defined in ACI 318-08 as the average concrete compressive stress when an adequately tied column reaches its axial strength. The average load carried by the longitudinal GFRP reinforcement ranged between about 2.9% and 4.5% of the ultimate load, whereas the average load carried by the vertical steel reinforcement was about 11.6% of the peak load. The results discussed above are based on the assumption that the modulus of elasticity of a GFRP bar in tension and compression are similar.

The axial strain in the longitudinal bars and the vertical strain on the external concrete surface at peak are summarized in Table 3. The range of minimum-maximum strain values, the average value and the number of readings are reported. For all the GFRP RC

specimens, the axial strain in the bars and that in the concrete are greater than those of the steel RC specimen. These results can be explained considering the fact that failure of the steel RC specimen seems to be ultimately caused by the buckling of the longitudinal bars rather than crushing of the concrete core. Conversely, in the case of the GFRP RC specimens with smaller tie spacing, failure is attributed to the crushing of the concrete core, while for all the GFRP RC specimens the relatively low contribution of the GFRP bars to the load-carrying capacity resulted in higher strains compared with the steel RC counterpart.

Experimental results are in agreement with what one could predict by considering the following. Assumed that plane sections remain plane and considered that the low reinforcement ratio makes the column stiffness to be controlled by the concrete section, for all column specimens axial deformation and peak load remain the same. In the case of the GFRP RC column specimens with large tie spacing and their steel counterpart, failure is controlled by vertical bar buckling because of the light confinement provided by the ties. Also, GFRP bars carry less stress than the steel ones because of the lower modulus of elasticity and concrete carries more stress than in the case of the steel counterpart due to its reserve capacity. For GFRP RC column specimens with small tie spacing, vertical bar buckling is restrained by the high confinement provided by the GFRP ties and higher post-peak axial deformations are achieved.

Influence of lateral ties

It has been widely recognized that axially loaded unconfined concrete contracts in

volume up to about 90% of its peak strength, and then expands at a higher rate as the softening branch develops until failure occurs (Hsu et al. 1963; Pantazopoulou and Mills 1995; Mirmiran et al. 1998b; Spoelstra and Monti 1999; Pessiki et al. 2001; Harries and Kharel 2002; Carey and Harries 2005). Plain concrete dilation ratio (defined as the ratio of transverse to axial strain) has an initial value (Poisson's ratio) generally found to be about 0.20 and increases up to 0.50 when the axial strain is about 0.002, and grows almost with vertical slope past this point. The following discussion is meant to highlight the impact of the internal confinement provided by the ties on the post-peak deformability of the column specimens. The analysis in terms of volumetric strain and dilation ratio seems to be helpful to justify the less brittle behavior of the GFRP RC column specimens with small tie spacing when compared with the ones with large tie spacing.

Fig. 7 and Fig. 8 show the volumetric strain-axial strain response and the dilation ratio-axial strain response, respectively, of all the specimens. The axial strain was considered as the measured axial deformation averaged along the entire height of the column. The volumetric strain (change in volume per unit volume of concrete) was calculated as sum of the axial strain and the two transverse strains at the mid-height cross-section, along the orthogonal directions of the LVDTs H1-H2 and H3-H4, respectively (Fig. 2). It must be noted that the volumetric strain discussed herein is "ideal" since not all cross sections behave as the mid-height one due to restraints provided by the loading platens. The mid-height cross section is thought to be the one who suffer the least of the effects of the boundary conditions. It is assumed that a positive volumetric strain indicates volume

reduction, whereas a negative value indicates expansion. The dilation ratio was defined as the ratio between the average transverse strain along the orthogonal directions of the LVDTs H1-H2 and H3-H4, respectively, and the axial strain.

Fig. 7, the initial slope of all the curves is close to $1-2\nu$ (where ν is the Poisson's ratio of the concrete assumed equal to 0.20), which corresponds to the perfectly elastic condition. The curves deviate from this line and reach their maximum (point of reversal in volumetric strain) as the load approaches its peak value. This point corresponds to the onset of uncontrolled crack growth leading to failure. In the cases of the GFRP RC specimens with larger tie spacing (A-12 and B-12) and of the steel RC specimen (S-16), the post-peak branch has a limited extent and rapidly develops into failure. In the case of the GFRP RC specimens with smaller tie spacing (A-3 and B-3), the larger development of the post-peak branch clearly shows that crack progression is more stable. In fact, the small spacing of the ties provides a lateral constraint for the cracked concrete core and delays unstable crack propagation.

In Fig. 8, the dilation ratio for all the specimens ranges between 0.15 and 0.30 up to axial strains of about 0.002. In the case of the GFRP RC specimens with larger tie spacing (A-12 and B-12), the dilation ratio remains constant between 0.15 and 0.20 up to a strain of about 0.0020, past which it increases indefinitely. The dilation ratio for the steel RC specimen (S-16) has an average value of 0.25 through axial strains up to 0.0028, past which it rapidly increases. No readings are available to describe the increasing branch because the loss of confinement, crushing of concrete and buckling of longitudinal bars occurred almost instantaneously. The dilation ratio for Specimen A-3, with smaller tie

spacing, starts from a value of 0.20 and increases fairly linearly up to an axial strain of about 0.0028, where it reaches a value of about 0.40. Past this level, the dilation ratio increases more rapidly and reaches a limit value near failure of about 0.90. In the case of Specimen B-3, the dilation ratio is approximately 0.20 up to an axial strain of about 0.003, and then rapidly increases up to about 0.90 at failure. It is noted that the dilation ratio-axial strain curve for the GFRP RC specimens with small tie spacing has a similar trend as in case of lightly confined concrete (Hsu et al. 1963; Pantazopoulou and Mills 1995; Mirmiran et al. 1998b; Spoelstra and Monti 1999; Pessiki et al. 2001; Harries and Kharel 2002; Carey and Harries 2005).

In Appendix 1, more evidence of the specimen failures is provided.

Conclusions

Based upon the experimental evidence gained through the full-scale experiments presented in this paper, the following conclusions are drawn.

1. The behavior of RC columns internally reinforced with GFRP bars is similar to that of conventional steel RC columns if the longitudinal reinforcement ratio is equal to 1.0%. No appreciable difference was observed in terms of peak load. Failure of the steel RC specimen happened due to buckling of the longitudinal reinforcement when still in the elastic range, whereas the GFRP RC specimens failed due to the crushing of the concrete core at axial strains higher than those

measured in the steel RC counterpart.

2. The use of longitudinal GFRP bars is not detrimental to the performance of RC columns. However, the contribution of the GFRP bars to the column capacity was less than 5% of the ultimate load, which is significantly lower than that of about 12% of the steel bars in the steel RC counterpart. It is concluded that the contribution of the GFRP bars may be ignored when evaluating the nominal capacity of an axially loaded RC column.
3. The 3 in. (305 mm) spacing of the GFRP ties does not contribute to increasing the peak load, but strongly influences the failure mode by delaying the buckling of the longitudinal bars, initiation and propagation of unstable cracks, and crushing of the concrete core.
4. Difference in the GFRP bar manufacturers does not affect the performance when bars are of comparable quality.

The limitation to specimens subjected to pure axial loading conditions precludes this research from proposing an immediate change of the ACI 440.1R guidelines to include design criteria for compression members in terms of definition of longitudinal and transverse reinforcement. However, as a first step towards the inclusion of the GFRP reinforced columns into the current ACI practice, the following considerations can be made.

1. The largest axial load a GFRP RC column can support (corresponding to the point of pure axial load in the column interaction diagram) can be computed neglecting the contribution of the internal GFRP reinforcement and considering the only

force carried by the concrete, which is equal to $0.85f'_cA_c$.

2. Given the fact that the GFRP RC column specimens and the steel one experienced the same behavior in terms of peak load, the same strength-reduction factor for pure compression as in the case of conventional steel may be adopted.
3. Use of GFRP bars as internal reinforcement in concrete columns becomes uneconomical when lateral loading conditions produce bending moments equivalent to vertical loads with an eccentricity which does not remain within the middle third of the cross section. Further research should include the effect of flexure and shear and be limited to the case of vertical loads applied with an eccentricity which does not exceed the boundaries of the cross sectional kernel.
4. Given the low contribution to column capacity, limiting the area of GFRP reinforcement to 1.0% of the gross sectional area appears reasonable.
5. The design of transverse reinforcement for GFRP RC columns cannot be based on the same criteria on which requirements for conventional steel transverse reinforcement are based. The brittle failure experienced by the GFRP RC column specimens with large tie spacing, which was defined by adapting ACI 318 requirements to the case of GFRP ties, is not desirable. Further investigation is needed in order to define a GFRP tie spacing which is more economically-efficient than the 3 in. (305 mm) one proposed in this work and, at the same time, able to prevent brittle failure of the concrete column.

A press release in the University of Miami (UM) website covers the research presented in this Study. The UM website and other website links related to this research are listed in Appendix3.

Table 1: Test matrix

Specimen ID	Longitudinal reinforcement	Transverse reinforcement	Bar type
S-16	8 #8 (25 mm diameter) bars	#4 ties @ 16 in.	ASTM Grade 60 steel
A-12		#4 ties @ 12 in.	GFRP Bar A
B-12	[$\rho = 1\%$]		#4 ties @ 3 in.
A-3		GFRP Bar A	
B-3		GFRP Bar B	

Note: 1 in = 25.4 mm.

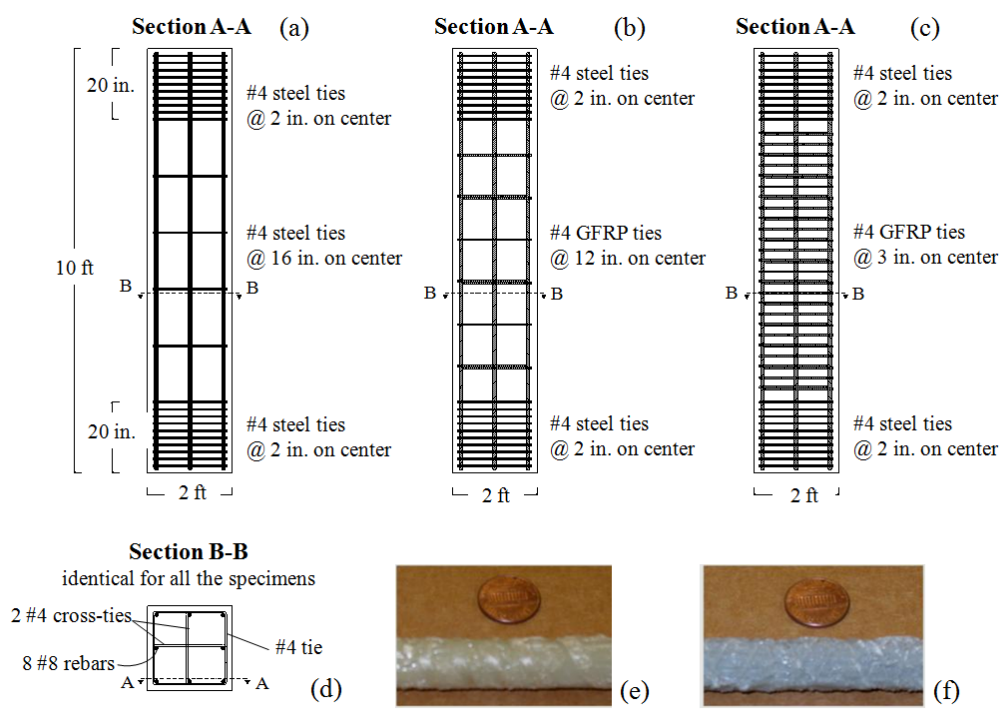
Table 2: Test results

Spec. ID	f_c [psi] (standard deviation [psi])	P_u [kip]	Δ_u [in]	Δ_{max} [in]	$\epsilon_{bar,u}$ [μ]	$P_{bar,u}$ [kip]	$(P_u - P_{bar,u}) / (f_c A_c)$ [%]	$P_{bar,u} / P_u$ [%]
S-16	5,413 (352)	2,818	0.262	0.357	1800	328	80.9	11.6
A-12	6,340 (307)	3,425	0.308	0.322	2890	109	90.9	3.2
B-12	5,885 (345)	2,911	0.286	0.320	2070	83.2	84.1	2.9
A-3	5,236 (204)	2,681	0.319	0.529	3000	113	86.7	4.2
B-3	4,763 (295)	2,417	0/285	0.561	2650	106	84.5	4.4

Note: 1,000 psi = 6.895 MPa; 1,000 kip = 4,448 kN; 1 in = 25.4 mm.

Table 3: Strain on longitudinal bars and concrete at peak load

Spec. ID	Axial strain on longitudinal bars			Vertical strain on concrete surface				
	Min. [μ]	Max. [μ]	Average [μ]	# of readings	Min. [μ]	Max. [μ]	Average [μ]	# of readings
S-16	1590	1960	1800	7	1660	1740	1690	4
A-12	2330	3300	2900	7	1560	2700	2130	6
B-12	1820	2270	2070	9	1640	2400	2030	6
A-3	2410	3510	3000	5	1950	2470	2160	4
B-3	2020	3150	2650	6	1520	3130	2230	6



Note: 1 in = 25.4 mm; 1 ft = 304.8 mm.

Fig. 1: Reinforcement layout of Specimen S-16 (a), A-12 and B-12 (b), and A-3 and B-3 (c); cross-section layout for all specimens (d); details of Bar A (e) and Bar B (f).

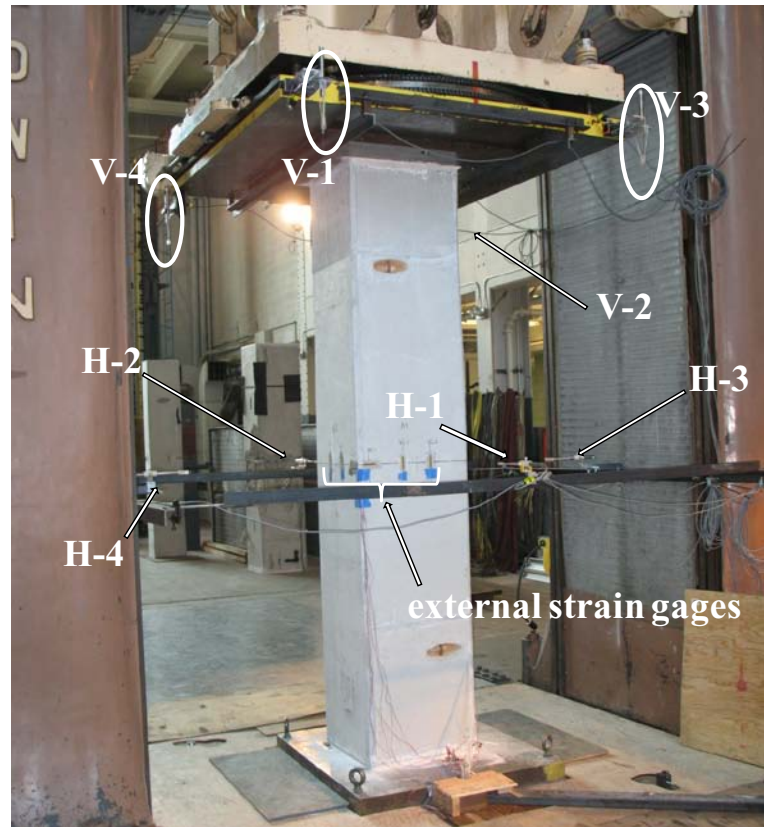
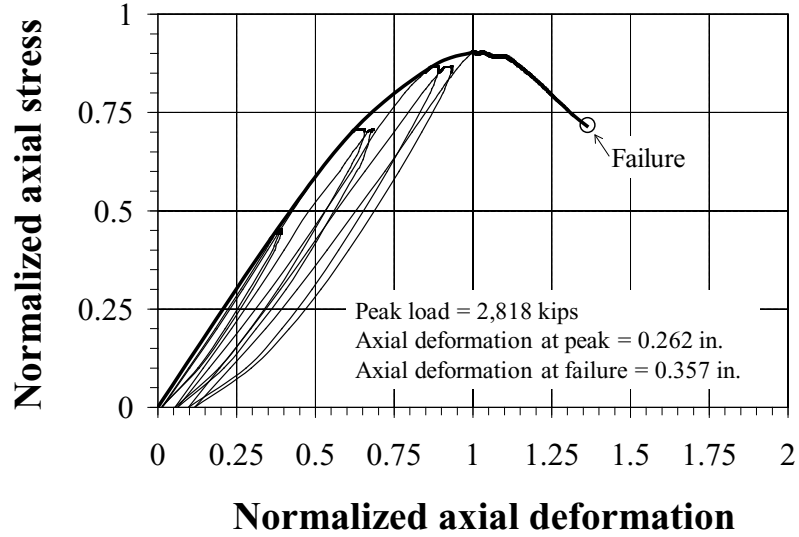


Fig. 2: Test setup



(a)



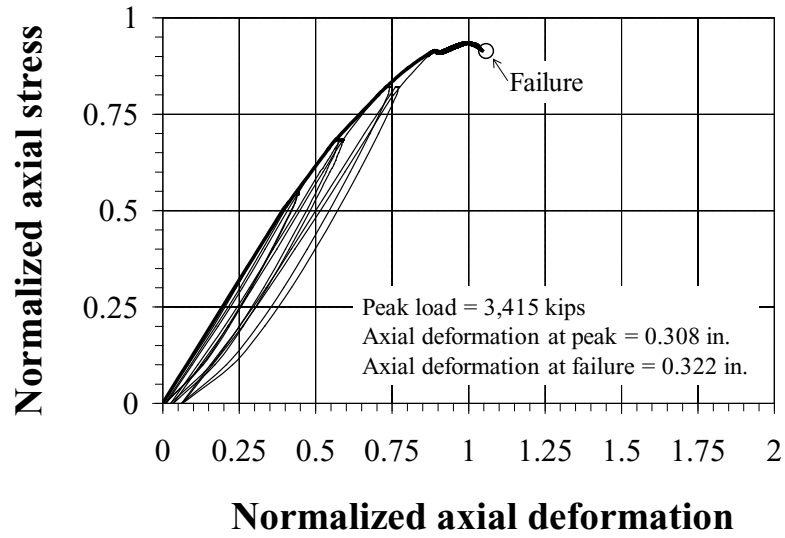
(b)



(c)

Note: 1,000 kip = 4,448 kN; 1 in = 25.4 mm.

Fig. 3: Specimen S-16: normalized axial stress-normalized axial deformation response where the thick line shows the envelope curve (a); photograph of failed specimen (b); close-up of buckled steel bars (c).



(a)



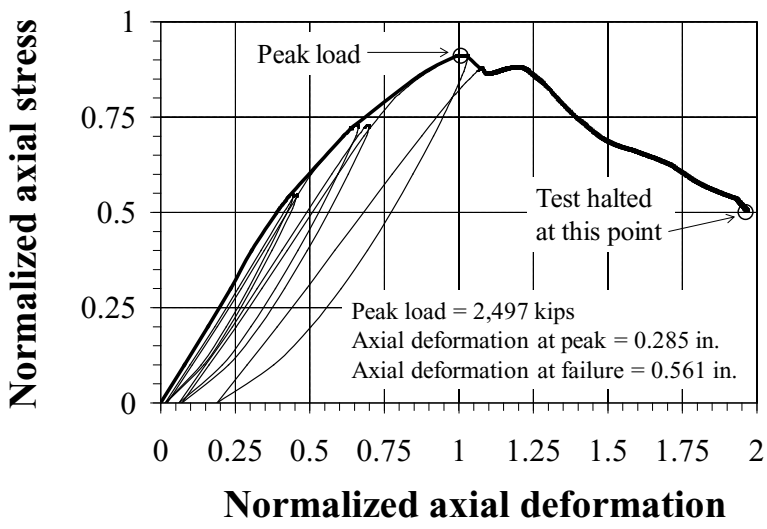
(b)



(c)

Note: 1,000 kip = 4,448 kN; 1 in = 25.4 mm.

Fig. 4: Specimen A-12: normalized axial stress-normalized axial deformation response where the thick line shows the envelope curve (a); photograph of failed specimen (b); close-up of buckled GFRP bars (c).



(a)



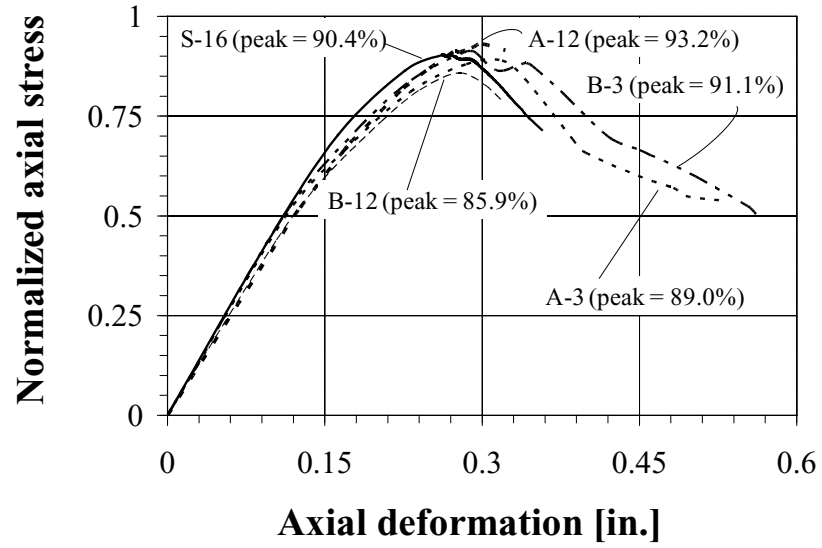
(b)



(c)

Note: 1,000 kip = 4,448 kN; 1 in = 25.4 mm.

Fig. 5: Specimen B-3: normalized axial stress-normalized axial deformation response where the thick line shows the envelope curve (a); photograph of failed specimen (b); close-up of failed GFRP tie and bulged bar (c).



Note: 1 in = 25.4 mm.

Fig. 6: Normalized axial stress-axial deformation.

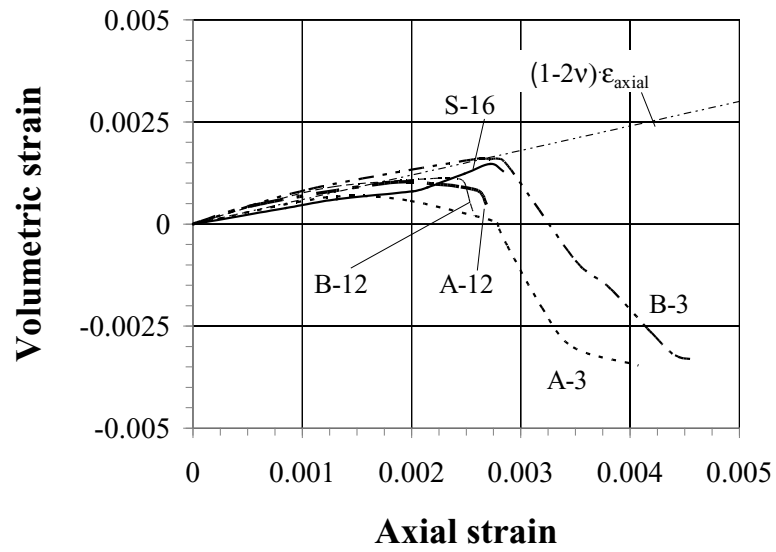


Fig. 7: Volumetric strain-axial strain.

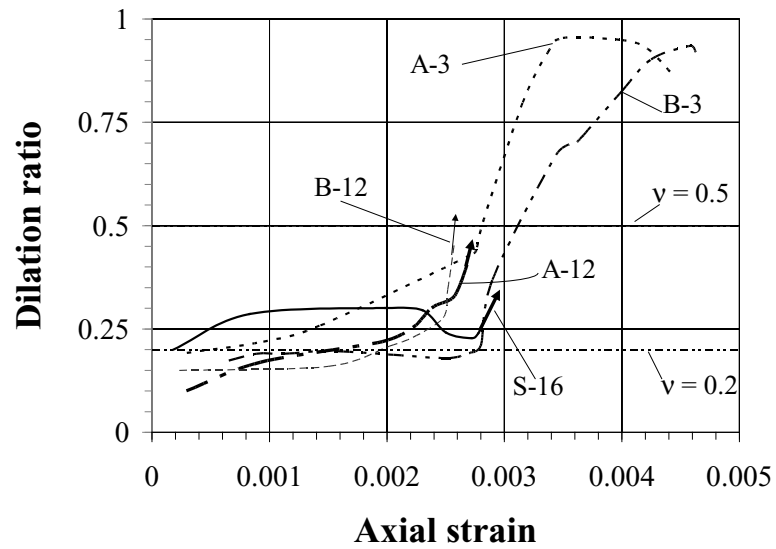


Fig. 8: Dilation versus axial strain.

Chapter 3: Study 2 – Structural Evaluation of Full-Scale Fiber Reinforced Polymer Confined Reinforced Concrete Columns

Background

A growing number of reinforced concrete (RC) building and bridge structures are in need of retrofitting and strengthening. There is a number of causes for this need: deterioration caused by environmental effects; damage; change in use of the structures; higher load demand as a consequence of more severe code requirements; and, higher strength and ductility demand to correct design or construction errors. The use of fiber reinforced polymer (FRP) composite materials has become a competitive alternative to conventional rehabilitation techniques, whereby confinement of RC columns is one of the most attractive applications. In FRP-confined concrete, the interaction between the two materials allows for the enhancement of concrete strength and ultimate strain. In the case of small plain concrete cylinders, the properties of the two materials are used in the most desirable and successful way: (a) the transverse FRP is loaded in tension due to concrete dilation, thus containing concrete after its internal cracking and providing lateral confining pressure; (b) the concrete is loaded in triaxial compression due to the restraining action of the FRP laminate, thus leading to a substantial improvement in strength and ultimate strain. The behavior of confined plane concrete cylinders subjected to pure axial loads has been extensively studied, and confinement effectiveness has been

experimentally proven since the late 1970's (e.g., Kurt 1978; Fardis and Khalili 1981; Nanni and Bradford 1994; Mirmiran and Shahawy 1996; Karbhari and Gao 1997; Spoelstra and Monti 1999; Fam and Rizkalla 2001; Shehata et al. 2002; Campione and Miraglia 2003; Lam and Teng 2003; Matthys et al. 2005; Harajli 2006; Saenz and Pantelides 2007; Wu et al. 2009). In concrete columns with circular cross-section, the confining effectiveness of the FRP jacket is optimal since the geometrical configuration allows the fibers to be effective on the entire cross section (Lam and Teng 2003). Prismatic cross-sections behave differently: as it is well recognized, the confining pressure is high at the corners and low along the flat sides, and the cross-section is only partially confined (Mander et al. 1988; Lam and Teng 2003b). Confinement of a rectangular cross-section still enhances concrete strength and ultimate strain, but its effectiveness is not as tangible as that of a circular cross-section (Rocca et al., 2006; Rocca et al., 2008). A number of studies have been conducted on FRP-confined RC prismatic columns, and several analytical models have been proposed (e.g., Mirmiran et al 1998; Wang and Restrepo 2001; Campione and Miraglia 2003; Lam and Teng 2003b; Kumutha et al 2007; Wu and Wang 2009). These models, however, do not converge to similar predicted values, and their validity for full-scale columns still has not been proven. In addition, the predictive equations are based on models originally devised for circular cross-sections, and modified by means of factors intended to account for the change in cross-sectional shape and its effect on the confining pressure.

Two databases reported by Hassan and Chaallal (2007) and Rocca et al. (2008) assemble relevant experimental data reported by several authors on RC prismatic columns

externally confined with FRP laminates and tested under compressive axial load from 1994 to 2007. The following can be noted: only 16 of the 113 column specimens included in the two databases (14% of the entire population) have short section sides larger than 12 in. (25.4 mm); only 1 column specimen is higher than 8 ft (2.44 m); the ratio between specimen height and short section side is always smaller than 5; 82 out of 113 column specimens (73%) are square; 16 (14%) are rectangular with a side-aspect ratio (ratio between large and short section sides) of about 1.5; 13 (13%) are rectangular with a side-aspect ratio of about 2; 86 column specimens (76%) were confined with carbon FRP (CFRP), 9 (8%) with glass FRP (GFRP), and 16 (18%) with aramid FRP (AFRP).

Existing experimental evidence on full-scale RC prismatic columns is scarce. Full-scale experiments are generally limited by high cost and availability of high-capacity testing equipment. Predictive design equations for concrete elements are usually first derived by fitting small-scale empirical data and then extended to full-scale (Bažant and Yavari 2004). Full-scale experiments are therefore critical not only to validate a new technology, but also to produce compelling evidence to justify rational design methodologies. It is herein defined as full-scale column an element with a minimum side larger than 12 in. (0.30 m) and a height-to-minimum side ratio greater than 5.

In terms of column confinement, glass fibers are particularly attractive. First, they have the highest ultimate strain of any “high-modulus” fiber; second, their low fatigue and creep-rupture resistance are not a detrimental factor in this type of application. In addition, the shortage of carbon fiber supplies that recently affected the market, as well as the development of high-performance glass fibers with lower manufacturing costs made

GFRP cost-competitive with CFRP laminates, thereby inducing an important increase in the demand of glass fibers over the last years. At the same time, continuous basalt fibers started to become commercially available. Basalt fibers offer an alternative to glass fibers due to their desirable characteristics, including, for example, thermal stability.

The research program presented herein aims at providing experimental evidence to remedy the lack of data needed to characterize the behavior of full-scale RC columns strengthened with FRP laminates subjected to pure compressive load. The condition of pure axial load is atypical for RC columns given that they always transmit axial compressive loads together with bending moments, but this condition represents the first step to understanding the mechanics of FRP confinement. An important novelty of this experimental campaign is the size of the column specimens, which provides the opportunity to investigate and validate the use of glass and glass-basalt hybrid laminates as confining systems on the basis of experimental evidence representative of real cases. In particular, this study aims at:

- investigating the effectiveness of the FRP confinement in relation to different cross-sectional geometries and sizes;
- studying the deformability enhancement due to FRP confinement;
- investigating the contribution of GFRP and hybrid glass-basalt FRP (HFRP) laminates to concrete confinement;
- assessing the equivalence of confined column performance when different glass fibers of comparable quality are used;

- assessing the contribution of the glass-basalt hybrid system on concrete confinement;
and
- comparing the experimental values of the normalized axial strength with those obtained using selected analytical models.

Experimental campaign

The test matrix, summarized in Table 4, was designed considering different factors, namely: shape factor (side-aspect ratio), volume factor (volume-aspect ratio based on a benchmark volume of $24 \times 24 \times 120 \text{ in}^3$ [$610 \times 610 \times 3050 \text{ mm}^3$]), FRP volumetric ratio (ratio between the total volume of confining FRP and volume of confined concrete), type and amount of FRP plies. The specimens were intended to represent real size building columns designed according to a dated ACI 318 code (i.e., prior to 1970) for gravity loads only.

Three series of column specimens were considered: series S-1 cross-section corresponds to a shape factor of 1.0 and a volume factor of 1.0; series R-1 cross-section to a shape factor of 1.45 and a volume factor of 1.0; series R-0.5 cross-section to a shape factor of 1.43 and a volume factor of 0.5. Three different types of fiber fabrics were used: two types of conventional glass fiber sheets from two different manufacturers (which are denoted herein as “type A” and “type B”); and a hybrid glass-basalt fiber sheet (glass-to-basalt fiber ratio 2:1). For each series one specimen was kept as-built and used as benchmark. For the first series (S-1), three specimens were confined with both the glass

FRP systems (types A and B) and with the HFRP system; for the second series (R-1), one specimen was confined with type A glass FRP and the other with the HFRP; for the third series (R-0.5), one specimen was confined with type A glass FRP, two specimens with type B glass FRP (with different number of plies), and one specimen with the HFRP system.

A three-part denomination is used to identify each specimen. The first part identifies the cross-sectional geometry: “S” stands for square (shape factor of 1.0) and “R” for rectangular (shape factor of either 1.45 or 1.43). The digits of the second part indicate the volume factor (1 or 0.5). The third part identifies type and number of plies: GA for type-A glass, GB for type-B glass and H for hybrid, with 2, 5 or 8 plies.

Specimen design

The column specimens were designed using the ACI 318-63 code-mandated minimum amount of longitudinal reinforcement and minimum tie area at maximum spacing. ACI 318-63 requires that the total area of longitudinal bars be larger than 1.0% of the gross section area, A_g ; and that the vertical spacing of the ties be the smallest of 16 longitudinal bar diameters (to prevent bar buckling), 48 tie diameters (to ensure sufficient tie area to restrain the lateral displacement of the longitudinal bars), and the least lateral dimension of the column (to develop the maximum strength of the concrete core). Column specimens were cast at a precast plant located in Miami (Fig. A - 1, Appendix 1) and let cure at the South Campus of the University of Miami (Fig. A - 2, Appendix 1).

Fig. 9, Fig. 10 and Fig. 11 show the reinforcement layout and the cross-section layout for series S-1, R-1 and R-0.5, respectively. The total cross-sectional area of the longitudinal bars was kept at 1.0% using eight No. 8 (25.4-mm diameter) bars for series S-1 and R-1, and four No. 8 (25.4-mm diameter) bars for series R-0.5. For series S-1 and R-1, No.4 (12.7-mm diameter) ties were used, spaced at 16 in. (406 mm) on-center, which corresponds to the requirement to prevent bar buckling. For series R-0.5, No. 4 (12.7-mm diameter) ties were spaced at 14 in. (356 mm) on-center, which corresponds to the requirement to develop the maximum strength of the concrete core. The specimens' dimensions were also selected to ignore slenderness effects. No. 4 (12.7-mm diameter) steel ties spaced at 2 in. (50.8 mm) on-center were used at the two ends of the specimens to prevent failure in these zones.

The FRP plies were applied by manual lay-up in the transverse direction. Prior to the application of the FRP, all corners were rounded with a radius of about 1 in (25.4 mm). The number of FRP plies was five in the case of the type A glass fiber sheets, two in the case of the type B glass fiber sheets, and eight in the case of the hybrid glass-basalt fiber sheets. Given that the fiber types were all of comparable quality, the number of plies was designed in order to have the same FRP volume ratio for all column specimens, with the exception of specimen R-0.5-5GB. In typical field applications, the number of plies ranges between 3 and 6 in the case of 1.1 lb/sq.yd (600 grams per square meter) yield, and between 2 and 3 in the case of 1.7 lb/sq.yd (900 grams per square meter) yield. Specimen R-0.5-5GB was designed to have a data point at a high FRP confinement ratio.

Column specimens were prepared at the South Campus of the University of Miami (Fig. A - 4 through Fig. A - 7, Appendix 1).

Materials

The specimens were fabricated at a precast plant one at a time using the same concrete mix design. The average nominal concrete compressive strength, f_c , and standard deviation for each specimen are reported in Table 5. Concrete strength is based on the results of compression tests on 6 by 12 in. (150 mm diameter by 304 mm) cylinder samples, 4 by 8 in. (100 mm diameter by 202 mm) cylinder samples, or 3.71 by 7.50 in. (92.7 mm diameter by 114 mm) core samples, per ASTM C 39. ASTM Grade 60 steel bars and ties were used for all specimens. Unidirectional continuous fiber sheets were used for the FRP systems, where the properties of the fiber sheets as provided by the manufacturers are summarized in Table 6.

Test setup and procedure

The instrumentation in all the specimens consists of electrical strain gauges located on the longitudinal and transverse steel reinforcement at the level of the mid-height cross section, and on the external surface of the specimen: onto the concrete surface at the mid-height section for the control specimens, and on the FRP jacket at critical locations (corner areas and mid-section on each face of the prismatic specimens) along the perimeter of the cross-section at mid-height of the strengthened specimens. Additionally, linear variable differential transformer (LVDT) sensors were used to measure the vertical displacement of the specimen, and to evaluate the horizontal (in-plane) dilation at the

mid-height cross-section, along the two side and the two diagonal directions. The control specimens were tested using a 5 million lbf (22.2 MN) testing machine. The tests of the strengthened specimens were conducted using a 12 million lbf (53.4 MN) testing machine. Special care was taken such that each specimen was plumb and centered with respect to the cross head of the machine. A thin layer of high-strength grouting paste was cast onto the base platen (below the specimen) and another one was cast on the top surface of the specimen. The load was applied concentrically with a displacement control rate of 0.02 in/min (0.5 mm/min). The loading sequence included five load cycles, each of which was repeated once, with increments of one fifth of the expected capacity. Fig. A - 8 through Fig. A - 11 (Appendix 1) sketch the position of the LVDTs and the location of the internal strain gauges. Photographs documenting testing equipments, test preparation and finale test setup are shown in Fig. A - 12 through Fig. A - 15 (Appendix 1).

Experimental results and discussion

The test results are summarized in Table 7. For each specimen, the following is reported: average nominal concrete compressive strength, f_c ; maximum load applied, P_{peak} ; load at failure, P_u ; ratio between load at failure and maximum load, P_u / P_{peak} ; axial deformation when the maximum load (peak) was reached, Δ_{peak} ; ultimate axial deformation, Δ_u ; ratio between ultimate axial deformation and axial deformation at peak, Δ_u / Δ_{peak} ; concrete axial stress at peak, $\sigma_{c,peak}$, normalized with respect to the average concrete compressive

strength, f_c , ($\sigma_{c,peak}/f_c$); ratio between normalized concrete axial stress at peak and corresponding value of the control specimen for the reference series. The axial deformation is rendered as the average of the measurements from the LVDTs. The concrete axial stress at peak is computed as the difference between the peak load (P_{peak}) and the load carried by the reinforcement (P_{bar}), divided by the net area of concrete (A_c), where P_{bar} is given as the total area of reinforcing steel (A_s) times the nominal yield stress (f_y).

Strength and failure modes

Failure of the control specimens initiated with vertical cracks followed, first, by lateral displacement of the longitudinal bars that contributed to the splitting of the concrete cover and, finally, by crushing of the concrete core and buckling of the longitudinal bars. All FRP-confined columns failed due to rupture of the FRP jacket; cracking of the concrete core developed after the maximum load was attained, and longitudinal bar buckling was visible after the post-mortem removal of the ruptured FRP jacket and concrete cover. In evaluating the increment in concrete strength due to confinement (last column in Table 7), instead of using the cylinder compressive strength as the benchmark, the strength of the control column specimen normalized with respect to f_c was used.

Series S-1 — Fig. 12 plots the normalized concrete axial stress (defined as the ratio between $\sigma_{c,peak}$ and f_c) with respect to the axial deformation of the specimens of series S-1. The failure of the benchmark specimen S-1-control, was brittle and occurred at the center of the upper half of the specimen. The ultimate capacity was attained when the

average concrete axial stress was equal to about 78% of the average concrete compressive strength, f_c . The load stabilized at the level of the peak load before it suddenly dropped. Cracking of the concrete was observed before splitting of the concrete cover and buckling of the longitudinal bars. The ultimate axial deformation recorded, u , was about 137% the value at peak load, u_{peak} , while the load dropped to 78% of the peak load. Crushing of the concrete core and buckling of the longitudinal bars are documented in Fig. 12. The confined specimens behaved similarly with respect to each other: upon attaining the peak load, the load steadily decreased while the axial deformation continued increasing due to the confining action of the FRP wrap. Failure occurred by rupture of the FRP laminates. In particular, fiber rupture always initiated in the proximity of a corner and then propagated towards the sides. The average concrete axial peak stress, $\sigma_{c,peak}$ ranged between 82 and 89% of the average concrete compressive strength, f_c , when the ultimate capacity was reached. The increment in concrete strength due to confinement was 14%, 5% and 8% for S-1-5GA, S-1-8H and S-1-2GB, respectively. An important improvement in deformability in the post-peak behavior was experienced by the confined specimens. The ultimate axial deformation recorded, u , was about 176% and 289% of u_{peak} for S-1-8H and S-1-2GB, respectively. While testing specimen S-1-5GA, a problem on the data acquisition system occurred that caused the loss of the data post-peak. Fig. 12 also shows the failure of the FRP wrap in specimen S-1-8H.

Series R-1 — Fig. 13 shows the normalized concrete axial stress versus axial deformation plot for the specimens of series R-1. Failure of the benchmark specimen, R-1-control, was sudden and accompanied by an explosive noise. The ultimate capacity was attained

at an average concrete axial stress equal to about 83% of f_c . Once the ultimate load was attained, the load dropped almost instantly without early warning, as no cracking of the concrete was observed until the final crushing. The ultimate axial deformation recorded, u_s , was only about 109% of $u_{s, peak}$. Failure occurred at the lower half of the specimen, as shown in Fig. 13. Specimen R-1-5GA experienced a premature failure localized at the top of the specimen due to stress concentration and has not been taken into account in this study. A 4 inch wide strip at the top end of specimen R-1-5GA was left unconfined: the splitting of the concrete cover in this region caused the premature rupture of the FRP jacket. Failure of specimen R-1-8H occurred due to rupture of the FRP laminate. Failure started at one of the corners at the higher half of the specimen and then expanded to the adjacent sides (Fig. 13). The peak load was reached when the average concrete axial stress was about 86% of f_c . The increment of concrete strength due to confinement was 4%, while the ultimate axial strain was about 169% of $u_{s, peak}$.

Series R-0.5 — The normalized concrete axial stress versus axial deformation plot for the specimens of series R-0.5 is shown in Fig. 14. Specimen R-0.5-control failed similarly to specimen S-1-control. The failure affected the entire upper half of the column. Concrete cracking was heard before that the concrete cover spalled and the steel bars buckled. The peak load was reached when the average concrete axial stress was about 75% of f_c . The failure was brittle, with a measured ultimate axial strain of 106% of $u_{s, peak}$. Specimens R-0.5-5GA, R-0.5-8H and R-0.5-5GB behaved similarly to each other. The average concrete axial stress ranged between 84% and 88% of f_c when the peak load was reached. The increment in concrete strength was 13% for both R-0.5-5GA and R-0.5-8H, and 17%

for R-0.5-5GB, as result of a higher FRP confinement ratio. After the peak load was attained, for both R-0.5-5GA and R-0.5-8H, the load gradually decreased with increasing axial deformations. R-0.5-5GA failed when the axial deformation almost doubled the value at peak. In the case of specimen R-0.5-8H, instead, the load stabilized at about 80% of the peak load, and the specimen failed when the axial deformation was about 346% of Δ_{peak} . For specimen R-0.5-5GB, the load remained nearly constant after reaching the peak load, with increasing axial deformations; following, the load decreased quite suddenly and stabilized at about 90% of the peak load. The specimen failed when the axial deformation was about 336% of Δ_{peak} . The failure mode was similar to that of the specimens of series S-1 and R-1, as documented in Fig. 14 for specimens R-0.5-5GB and R-0.5-8H. Specimen R-0.5-2GB did not experience any gain in concrete strength. The peak load was reached when the average concrete axial stress was about 75% of f_c and the ultimate axial deformation was about 266% of Δ_{peak} . Factors contributing to this strength result may include those affected by preparation, setup and execution of the test itself.

Vertical strain in reinforcing bars

Strain gages were attached on the longitudinal steel bars at the level of the mid-height cross-section at the mid-distance between two adjacent ties. The average axial strain on the bars recorded for the unstrengthened specimens is close to the yield strain and slightly higher than the one measured for confined specimens. This can be explained as follows. In the case of unconfined specimens, the strain gages stopped reading immediately after the concrete cover split since they were located at the interface between bar and concrete

cover. The compressive strain recorded on the steel bars by the strain gages was not affected by the lateral displacement of the bars since concrete failure and bar buckling happened concurrently. For confined specimens, instead, the confining action provided by the FRP jacket delayed the column failure and the strain gages continued reading after concrete cover splitting. Strain readings were affected by the lateral deflection of the steel bars. The compressive strain was therefore reduced by the tensile strains induced by the lateral bending of the bars since the strain gages were located on the exterior side of the rebars. Experimental measurements were not used for the analysis, and, given also the small percentage of steel reinforcement, the assumption of yielded steel is considered reasonable for analysis purposes.

Volumetric response

The impact of the external confinement provided by the FRP jacket on column strength enhancement and post-peak deformability is analyzed with respect to the volumetric response. It has been widely recognized (Pantazopoulou and Mills, 1995; Spoelstra and Monti, 1999) that axially loaded unconfined concrete contracts in volume up to about 90% of its ultimate strength; then, the direction of the volume change reverses and results in an inelastic volume expansion when the ultimate strength is reached. Beyond this point, the volume expansion grows at a higher rate as the softening branch develops until failure occurs. When concrete is confined with FRP jackets, the volume expansion may be effectively constrained, and the unstable crack growth controlled. Provided that the jacket is sufficiently thick, concrete expansion can be curtailed (Mirmiran et al. 1998; Spoelstra and Monti 1999; Pessiki et al. 2001; Harries and Kharel 2002; Carey and

Harries 2003; Lam and Teng 2003a-b). Plain concrete dilation ratio (defined as the ratio of transverse to axial strain) has an initial value (Poisson's ratio) generally found to be about 0.20, begins to increase non-linearly when concrete starts cracking, and grows indefinitely until failure. The presence of the FRP jacket affects the concrete dilation ratio before and after the concrete reaches its ultimate capacity by significantly restraining the growth in volume and allowing large axial deformations (Mirmiran et al. 1998; Pessiki et al. 2001).

Herein, the axial strain is derived from the the LVDT-measured axial deformation over the entire height of the column. The volumetric strain (change in volume per unit volume of concrete) is calculated as the sum of the axial strain and the two transverse strains at the mid-height cross-section (measured along the two orthogonal directions in the plane of the cross-section). A positive volumetric strain indicates volume reduction, whereas a negative value indicates expansion. The volumetric strain represents a parameter indicative of the response of the cross-section in its entirety, unlike the dilation ratio which indicates how the cross-section tends to deform along different directions. The dilation ratio is defined as the ratio between the average transverse strain along each of the two orthogonal directions in the plane of the cross-section and the axial strain. The mid-height cross section is less affected by the boundary conditions and, even though failure may occur elsewhere, it is taken as representative of the behavior of the column.

Series S-1 — Fig. 15a and Fig. 16a show the volumetric strain-axial strain response and the dilation ratio-axial strain response, respectively, of the specimens of series S-1 with the exception of specimen S-1-5GA, for which the data for the post-peak branch were not

available. The initial slope of all the curves in Fig. 15a is close to $(1-2\nu)$ (where ν is the Poisson's ratio of the concrete assumed equal to 0.20), which corresponds to the elastic condition. The curves deviate from this line and reach their maximum (point of reversal in volumetric strain) as the load approaches its peak value. This point corresponds to the onset of uncontrolled crack growth leading to failure in the case of the control specimen (S-1-control), whose post-peak branch has a limited extent and rapidly develops into failure. In the case of the externally confined specimens (S-1-2GB and S-1-8H), the larger development of the post-peak branch clearly shows that the external FRP jacket provides a lateral constraint for the cracked concrete and reverses the dilation process of the concrete. In Fig. 16a, the dilation ratio for the control specimen has an average value of about 0.2 through axial strains up to 0.0028, past which it rapidly increases. No readings are available in the post-peak zone because the loss of confinement, crushing of concrete and buckling of longitudinal bars occurred almost instantaneously. The dilation ratio for specimens S-1-2GB and S-1-8H (Fig. 16a) ranges between 0.15 and 0.25 up to axial strains of about 0.002. Past this level, the dilation ratio for both specimens increases rapidly and reaches a limit value of about 1.5 when the axial strain is about 0.0035. Beyond this point, both curves begin to decrease almost with the same slope. Specimen S-1-2GB failed when the axial strain was about 0.005 and the dilation ratio dropped to about 0.8. Specimen S-1-8H reached an axial strain at failure of about 0.009 with a dilation ratio dropping to about 0.5. Fig. 17a shows the plot of the dilation ratio of specimen S-1-control measured along the two transverse directions, whereas Fig. 18a shows the dilation ratio of specimen S-1-8H measured along one of the two transverse directions and along the two diagonals. In case of the control specimen, the dilation ratio

along both transverse directions is similar, that is, the cross-section deforms symmetrically along these axes. For specimen S-1-8H, after reaching its ultimate capacity, the concrete core tends to expand much more along the transverse directions rather than along the two diagonals. As expected for a square column, the dilation ratio is symmetrical along the two diagonals.

Series R-0.5 — To describe the volumetric response of specimens of series R-0.5, specimens R-0.5-control, R-0.5-5GB and R-0.5-8H were selected. Fig. 15b and Fig. 16b show the volumetric strain-axial strain and the dilation ratio-axial strain relations, respectively. The volumetric response of specimen R-0.5-control is similar to that experienced by specimen S-1-control. In the case of the confined column specimens, the FRP jacket constrains the volume dilation of the concrete core, but its effectiveness is not sufficient to reverse the volumetric expansion as for the square columns. For specimen R-0.5-5GB, given the higher FRP amount compared to specimen R-0.5-8H, a reversal point is reached but not maintained. The dilation ratio for the control specimen has a constant average value of about 0.30 until failure occurs (Fig. 16b). The dilation ratio for specimens R-0.5-5GB and R-0.5-8H (Fig. 16b) ranges between 0.30 and 0.45 up to axial strains of about 0.0015. Past this level, the dilation ratio for both specimens increases at a high rate until a value of about 2 at axial strains of about 0.003. Beyond this point, the dilation ratio continues to increase at a low rate until failure. Specimen R-0.5-5GB failed when the axial strain was about 0.009 and the dilation ratio was about 2.1. Specimen R-0.5-8H reached an axial strain at failure of about 0.008 with a dilation ratio close to 2.3, whereas its square counterpart (S-1-8H) reached an axial strain at failure of about 0.009

with a dilation ratio close to 0.5. Fig. 17b plots the dilation ratio of specimen R-0.5-control measured along the two transverse directions, while Fig. 18b illustrates the dilation ratio for specimen R-0.5-8H measured along the two transverse directions (short and long side) and along one of the two diagonals. The dilation ratio along the long side is much smaller than the one along the short side for both the control and confined specimens. In the case of the control specimen, the development of unstable cracks makes the long side dilation ratio to rapidly increase until failure.

Fig. 19a-d shows the change in volume of a representative one-quarter unit element of specimens S-1-8H and R-0.5-8H, respectively, when the peak load is reached (a and c) and at failure (b and d) by plotting the displacements of the mid-points of the two sides and of the corner and the axial shortening. To make the change in volume visible, all changes in length are amplified using the same magnification factor. Given the symmetry, only one quarter of the cross-section is drawn. For both square and rectangular shapes, when the peak load of the column is reached no significant cross-sectional shape change is noted (Fig. 19a and Fig. 19c), namely: the displacements of the mid-points of the two sides are of the same order of magnitude and the displacement of the corner is smaller, but comparable to the transverse ones. For the square column, the transverse expansion at failure is significantly higher than the diagonal one (Fig. 19b). This experimental observation confirms the generally accepted assumption that in prismatic cross-sections the confining pressure is higher at the corners than along the flat sides. For the rectangular column under failure load (Fig. 19d), instead, the displacements of the mid-point on the long side and of the corner are of about the same magnitude and much

larger than the displacement of the mid-point on the short side, respectively. The commonly accepted assumption is that the area of effective confinement is defined by four parabolas within which the concrete is fully confined (and outside of which negligible confinement occurs). Based on this experimental evidence, it appears that the two parabolas along the short sides may be disregarded, being the dilation in the direction orthogonal to the short side small. As the rectangular column has more FRP than the square one, and yet the jacket is less effective, the lower level of performance has to be attributed to the cross sectional shape. Moreover, it appears that for a prismatic cross-section, the increment in concrete strength is only possible when concrete contracts in volume. Fig. 20 shows a common axial stress-volumetric strain relationship for FRP-confined prismatic columns. The FRP confinement allows the reversal in volume change, and, during the process of volume dilation, concrete experiences large axial deformations without increasing its axial strength.

In Appendix 4, more evidence of the specimen failures described in Study 2 is provided. Failed specimens belonging to Series S-1 are showed in Fig. A - 22 through Fig. A - 25, failed specimens belonging to Series R-1 in Fig. A - 26 through Fig. A - 28, and failed specimens belonging to Series R-0.5 in Fig. A - 29 through Fig. A - 33.

Review of existing constitutive models for FRP-confined prismatic columns

Models' theoretical prediction of the increment in concrete strength

The increment of concrete strength achieved by each specimen is compared with the theoretical prediction given by the analytical models proposed by Mirmiran et al. (1998), Wang and Restrepo (2001), Campione and Miraglia (2003), Lam and Teng (2003b), Kumutha et al. (2007), and Wu and Wang (2009). In evaluating the theoretical increment in concrete strength due to confinement, both the cylinder strength and the strength of the control column reduced by the contribution of the longitudinal reinforcing steel and normalized with respect to f_c were used. Theoretical predictions are plotted in Fig. 21 and Fig. 22. The ordinates of the histograms represent the following:

$$\left(\frac{f_{cc}}{f_c} \right)_{THEOR} / \left(\frac{f_{cc}}{f_c} \right)_{EXP} \quad (2)$$

where $(f_{cc}/f_c)_{THEOR}$ is the theoretical ratio between the confined concrete strength and the unconfined concrete strength, and $(f_{cc}/f_c)_{EXP}$ is the experimental ratio between the increment in concrete strength and the unconfined concrete strength. In computing $(f_{cc}/f_c)_{EXP}$, when the cylinder strength is at the denominator of the ratio, the experimental results are overestimated by the models. Conversely, the predictions tend to underestimate the experimental results if the strength of the control specimen is used. All models rely on the assumption that the concrete strength of an as-built unconfined column is equal to that of a control cylinder, f_c . This assumption was not verified in this

study as f_c was found to be about 20% higher than the axial concrete strength of an as-built column. This issue had never been addressed before because the models base their predictions on scaled cylinders with height-to-diameter ratio equal to 2, whereas the work presented herein refers to full-scale elements with a height-side ratio equal or larger than 5, as representative of building columns.

The following discussion is limited to the comparison of the theoretical models with the predictions based on the strength of the control column. As can be noted from the histograms reported in Fig. 21, Mirmiran et al.'s, Wang and Restrepo's, Campione and Miraglia's and Wu and Wang's models tend to underestimate the increment in concrete capacity for the square column specimens. Kumutha et al.'s model always overestimates the experimental results. Lam and Teng's and Wang and Restrepo's models are also quite accurate in predicting the concrete capacity enhancement for the rectangular column specimens which is instead overestimated by Kumutha et al.'s model (Fig. 22). Campione and Miraglia's and Lam and Teng's models also provide a closed-form formula to predict the ultimate concrete strain, but the predictions are not in agreement with the experimental results.

Lateral pressure and strain in the FRP

The definition of the lateral confining pressure exerted by the FRP jacket on the concrete core is key to the prediction of the increment in concrete strength. The lateral pressure depends on the strain in the FRP and varies depending on the cross-sectional shape (circular or prismatic). For circular cross-sections, the lateral pressure is “ideally”

uniformly distributed around the perimeter and, therefore, it can be derived based on equilibrium considerations. For prismatic cross-sections, it is not uniform along the perimeter: it is high in proximity of the corners and low along the sides. However, in the most commonly adopted confinement models for prismatic columns, the lateral pressure is derived by using the same expression used for circular cross-sections adjusted to take into account the different shape. It is widely acknowledged that for FRP-confined circular columns (for commonly used numbers of FRP plies), the final point in the stress-strain relationship defines both the peak load and the ultimate axial strain. The peak stress is reached when the FRP ruptures, and the lateral confining pressure is the maximum attained. Therefore, it is reasonable to express the lateral confining pressure in terms of the ultimate strain in the FRP when failure occurs. On the contrary, as shown previously and in agreement with earlier research (Pessiki et al. 2001; Shehata et al. 2002; Rocca et al. 2008), in the case of FRP-confined prismatic concrete columns, while failure coincides with rupture of the FRP, the peak capacity of the column occurs at an FRP strain much lower than its ultimate value. Consequently, it does not appear logical to relate the lateral pressure to the ultimate strain in the FRP.

Conclusions

Based upon the experimental evidence gained through the full-scale experiments presented in this paper, the following conclusions are drawn.

1. The axial load-axial deformation behavior of a prismatic concrete column

laterally confined by means of an FRP jacket of thickness representative of field applications is characterized by a linear elastic branch almost up to the peak load, and a descending post-peak branch until failure. In prismatic columns, the FRP confinement effectiveness is more significant in terms of enhancement of concrete axial deformation rather than increment in axial strength. The presence of the FRP jacket allows a “growth” in volume of the concrete core by offsetting buckling of the longitudinal bars and by delaying unstable crack propagation.

2. The shape of the cross-section influences the effectiveness of the confinement. Effectiveness is higher for square shapes than for rectangular ones, and decreases as the side aspect ratio of a rectangular cross-section increases. The transverse expansion of the concrete core in the plane of the cross-section, defined by means of the dilation ratio, changes with the direction along which it is evaluated. For square cross-sections the dilation ratio is smaller along the diagonals than along the two transverse directions, whereas for rectangular cross-sections it is high if measured along the short transverse direction and along the diagonals, and low along the long transverse direction.
3. Existing semi-empirical prediction models do not converge to the same predictions for the ultimate axial capacity of full-scale FRP-confined prismatic concrete columns. The limitations of the analyzed models can be summarized as follows:
 - use of the same methodology developed for circular cross-sections and adjustment to the case of prismatic shapes by means of correction factors;
 - increment in strength due to the FRP confinement based on the strength of




a control concrete cylinder, f_c , rather than the concrete strength of the as-built unconfined column;

- lack of accuracy in the prediction of the ultimate concrete axial strain.
4. Difference in the FRP material manufacturers does not affect performance when confining materials are of comparable quality. The contribution to column confinement of the hybrid glass-basalt FRP laminates was similar to that of the GFRP laminates.

Notation

A_g	gross section area
A_c	net area of concrete
A_s	total area of reinforcing steel
f_c	average cylinder compressive strength
f_y	nominal steel yield stress
P_{peak}	maximum load applied
P_{bar}	load carried by the reinforcement
P_u	load at failure
P_u / P_{peak}	ratio between load at failure and maximum load
Δ_{peak}	axial deformation when the maximum load (peak) was reached
Δ_u	ultimate axial deformation
Δ_u / Δ_{peak}	ratio between ultimate axial deformation and axial deformation at peak
σ_c	concrete axial stress
$\sigma_{c,peak}$	concrete axial stress at peak,
σ_c / f_c	normalized concrete axial stress
$\sigma_{c,peak} / f_c$	normalized concrete axial stress at peak
ν	Poisson's ratio of the concrete (assumed equal to 0.20)
$(f_{cc} / f_c)_{THEOR}$	theoretical ratio between the confined concrete strength and the unconfined concrete strength
$(f_{cc} / f_c)_{EXP}$	experimental ratio between the increment in concrete strength and the unconfined concrete strength

Table 4: Test matrix

Specimen code	Cross-section Geometry	Internal steel reinforcement	Shape factor	Volume factor	FRP		
					volumetric ratio (%)	Type of fibers	No. of plies
S-1-control	 24 by 24 in				-	-	-
S-1-5GA	corners chamfered with a radius of about 1 in	8 #8	1.0	1.0	1.57	GLASS A	5
S-1-2GB	corners chamfered with a radius of about 1 in	longitudinal bars and #4 ties			1.67	GLASS B	2
S-1-8H	corners chamfered with a radius of about 1 in	at a spacing of 16 in			1.49	HYBRID	8
R-1-control	 20 by 29 in				-	-	-
R-1-5GA	corners chamfered with a radius of about 1 in	1.45	1.0		1.60	GLASS A	5
R-1-8H	corners chamfered with a radius of about 1 in				1.51	HYBRID	8
R-0.5-control					-	-	-
R-0.5-5GA	 14 by 20 in	4 #8			2.29	GLASS A	5
R-0.5-2GB	corners chamfered with a radius of about 1 in	longitudinal bars and #4 ties	1.43	0.5	2.43	GLASS B	2
R-0.5-5GB	corners chamfered with a radius of about 1 in	at a spacing of 14 in			6.07	GLASS B	5
R-0.5-8H	corners chamfered with a radius of about 1 in				2.18	HYBRID	8

Note: 1 in = 25.4 mm; #8 bar = 25.4-mm diameter bar; #4 bar = 12.7-mm diameter bar

Table 5: Concrete nominal strength

Specimen code	Concrete sample (diameter and height are in inches)	No. of tests	Average strength, f_c [psi]
S-1-control	6 by 12	6	5,414
S-1-5GA	6 by 12	3	7,051
S-1-2GB	3.71 by 7.50 (core)	3	5,384
S-1-8H	6 by 12	3	6,440
R-1-control	6 by 12	3	6,953
R-1-5GA	3.71 by 7.50 (core)	3	8,180
R-1-8H	3.71 by 7.50 (core)	3	6,902
R-0.5-control	4 by 8	3	5,032
R-0.5-5GA	4 by 8	3	7,802
R-0.5-2GB	4 by 8	6	6,730
R-0.5-5GB	4 by 8	6	7,211
R-0.5-8H	4 by 8	3	6,786

Note: 1,000 psi = 6.895 MPa 1 in. = 25.4 mm. According to the ASTM C39 Standards, if the specimen length to diameter ratio is higher than 1.75, the concrete compressive strength can be taken as is and no correction factor has to be applied.

Table 6: FRP system properties

Filament yarn properties	Glass A fabric	Glass B fabric	Hybrid fabric
Type of fibers	Glass	Glass	Basalt – Glass
Ratio in volume	100%	100%	33.3% – 66.6%
Tensile modulus (ksi)	11,160	10,500	12,900 – 11,160
Tensile strength (ksi)	493	470	702 – 493
Tensile strain (%)	4.7	4.5	3.15 – 4.7

Sheet properties	Glass A fabric	Glass B fabric	Hybrid fabric
Ply thickness (in)	0.00968 [0.0189]	0.0232 [0.05]	0.00472 [0.0112]
Weight (lb/yd ²)	1.1	1.7	0.6

Note: 1 ksi = 6.895 MPa; 1 in = 25.4 mm; 1 lb/yd² = 0.542 g/m²; in square brackets gross laminate properties.

Table 7: Test results

Spec. ID	f_c [psi]	P_{peak} [kip]	P_u [kip]	$\frac{P_u}{P_{peak}}$	Δ_u^{peak} [in]	Δ_u [in]	$\frac{\Delta_u}{\Delta_{peak}}$	$\frac{\sigma_{c,peak}}{f_c}$	$\frac{\sigma_{c,peak}}{(\sigma_{c,peak}/f_c)_{control}}$
S-1-control	5,414	2,810	2,219	0.789	0.257	0.352	1.37	0.779	1.00
S-1-5GA	7,051	4,002	N/A	N/A	0.276	N/A	N/A	0.893	1.15
S-1-2GB	5,384	2,923	2,201	0.753	0.357	0.627	1.76	0.821	1.05
S-1-8H	6,440	3,507	2,720	0.775	0.240	1.11	4.61	0.843	1.09
R-1-control	6,953	3,710	3,665	0.987	0.279	0.304	1.09	0.826	1.00
R-1-8H	8,180	3,822	2,878	0.750	0.340	0.576	1.69	0.870	1.05
R-0.5-control	6,902	1,241	1,135	0.915	0.315	0.330	1.06	0.746	1.00
R-0.5-5GA	5,032	1,947	1,459	0.750	0.303	0.603	1.99	0.847	1.13
R-0.5-2GB	7,802	1,598	1,205	0.754	0.269	0.717	2.66	0.748	1.00
R-0.5-5GB	6,730	1,963	1,542	0.785	0.360	1.21	3.36	0.879	1.18
R-0.5-8H	7,211	1,792	1,358	0.758	0.315	1.09	3.46	0.844	1.13

Note: 1,000 psi = 6.895 MPa; 1,000 kip = 4,448 kN; 1 in = 25.4 mm; $\sigma_{c,peak} = (P_{peak} - P_{bar}) / A_c$.

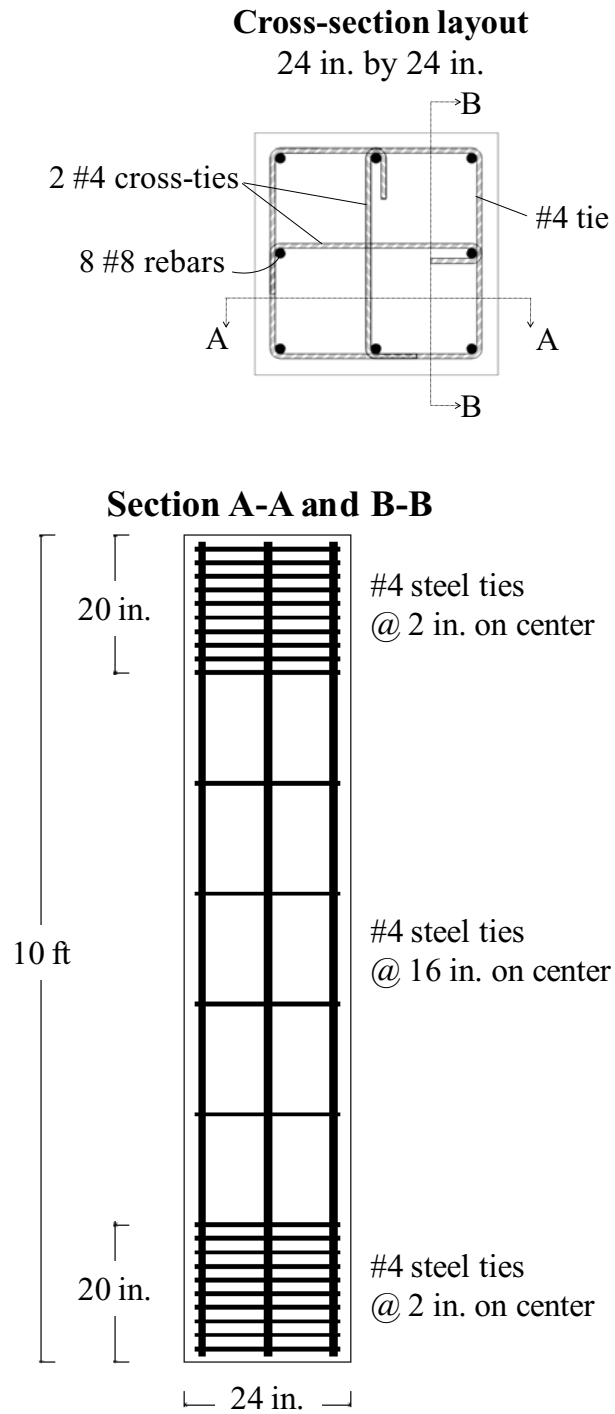


Fig. 9: Reinforcement layout for series S-1.

Cross-section layout
20 in. by 29 in.

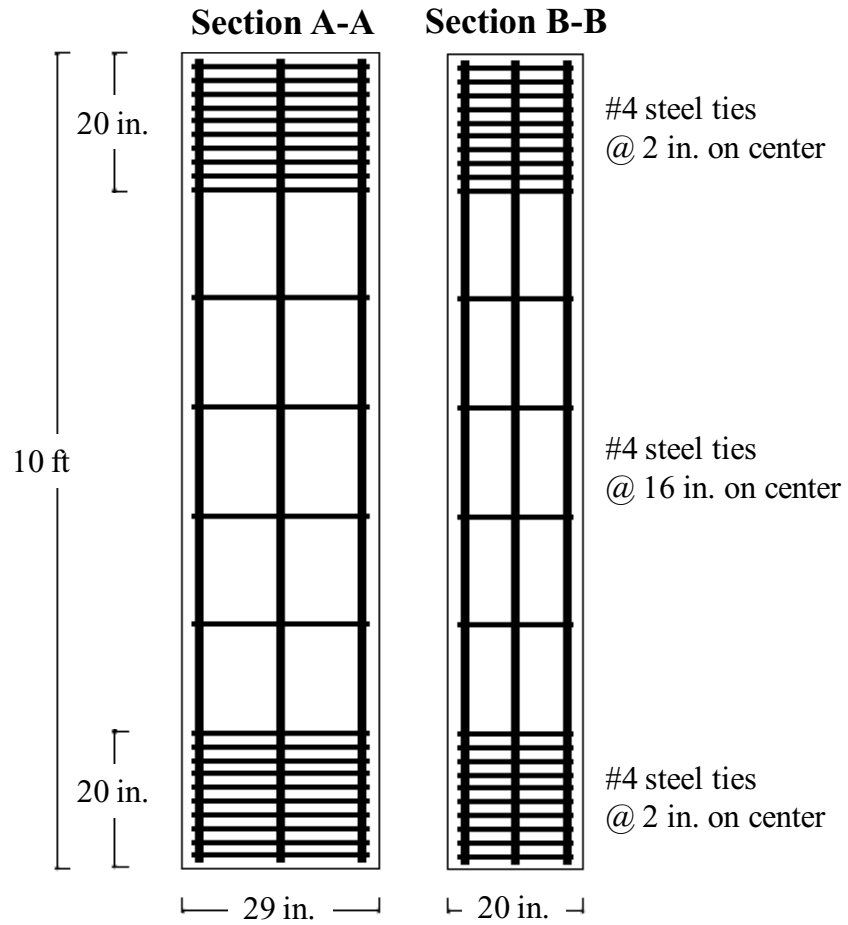
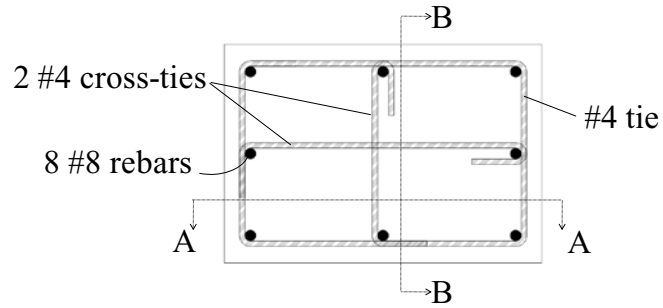


Fig. 10: Reinforcement layout for series R-1.

Cross-section layout
14 in. by 20 in.

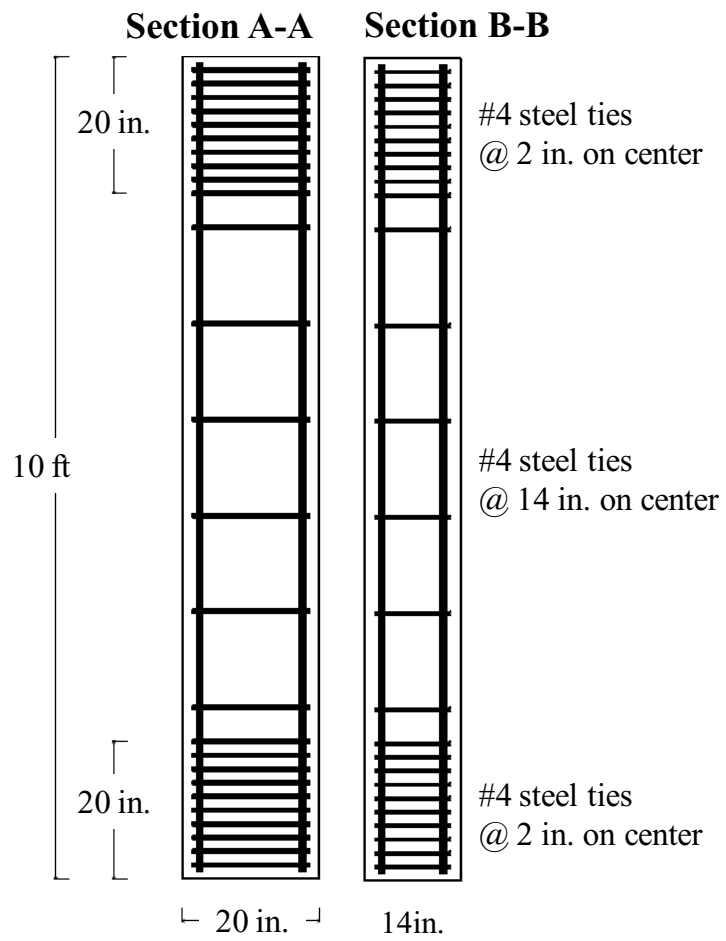
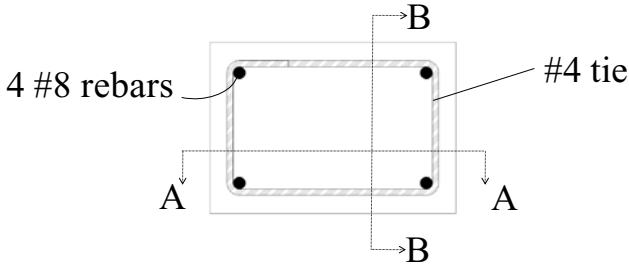


Fig. 11: Reinforcement layout for series R-0.5.

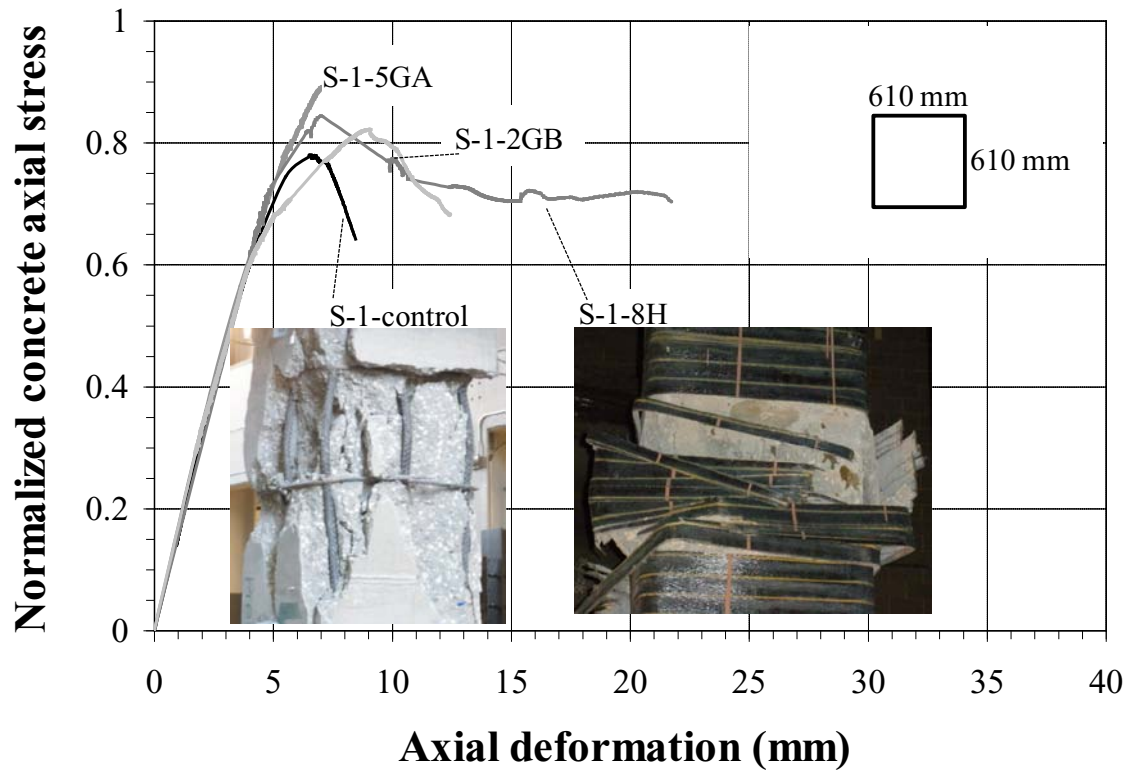


Fig. 12: Normalized concrete axial stress vs. axial deformation (series S-1). Failed specimens S-1-control and S-1-8H are also showed.

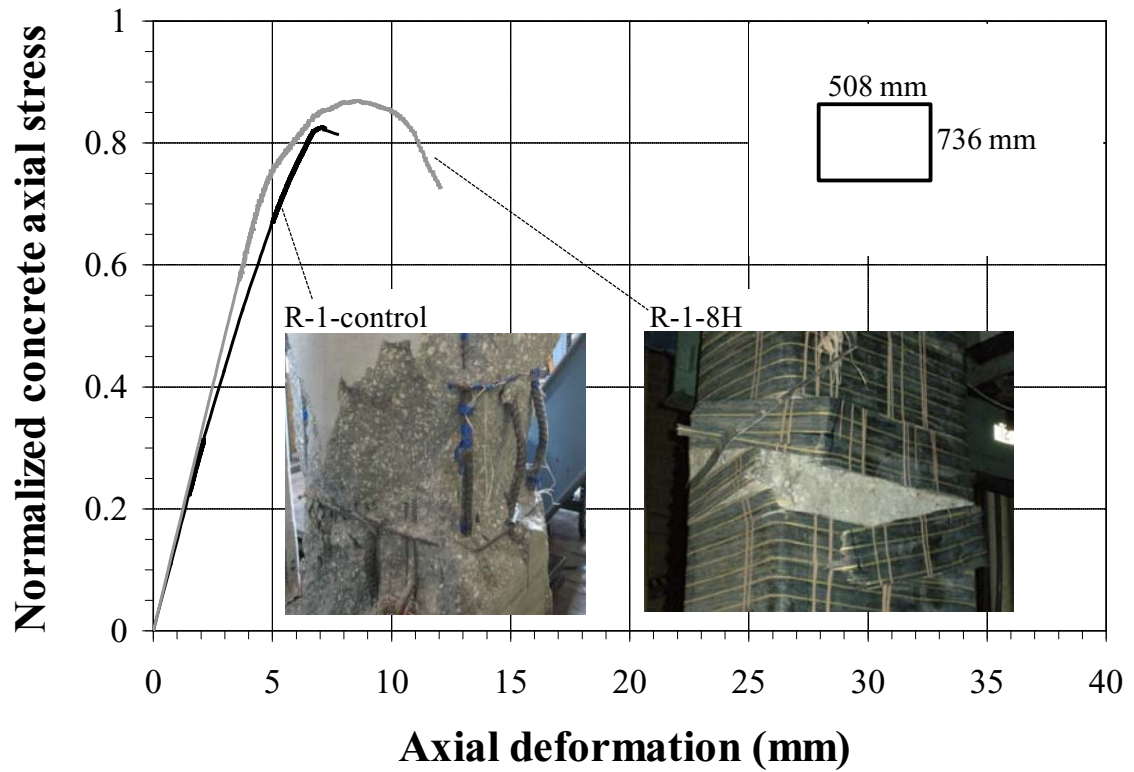


Fig. 13: Normalized concrete axial stress vs. axial deformation (series R-1). Failed specimens R-1-control and R-1-8H are also showed.

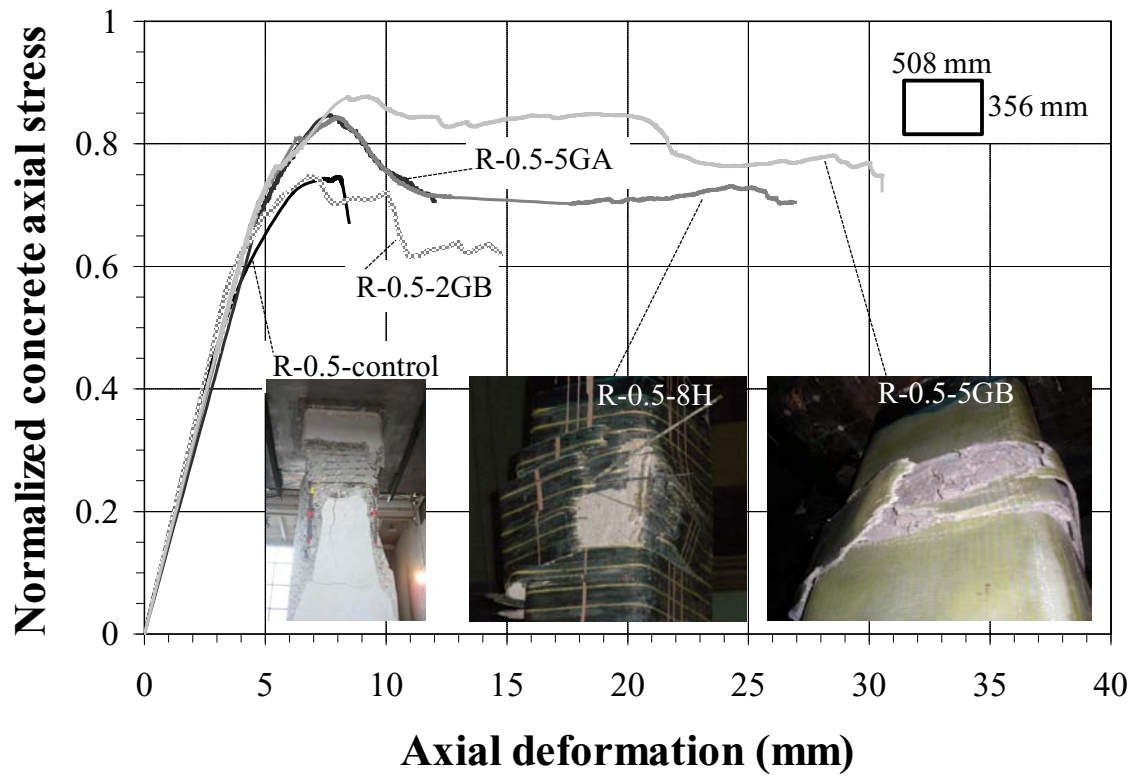


Fig. 14: Normalized concrete axial stress vs. axial deformation (series R-0.5). Failed specimens R-0.5-control, R-0.5-5GB and R-0.5-8H are also showed.

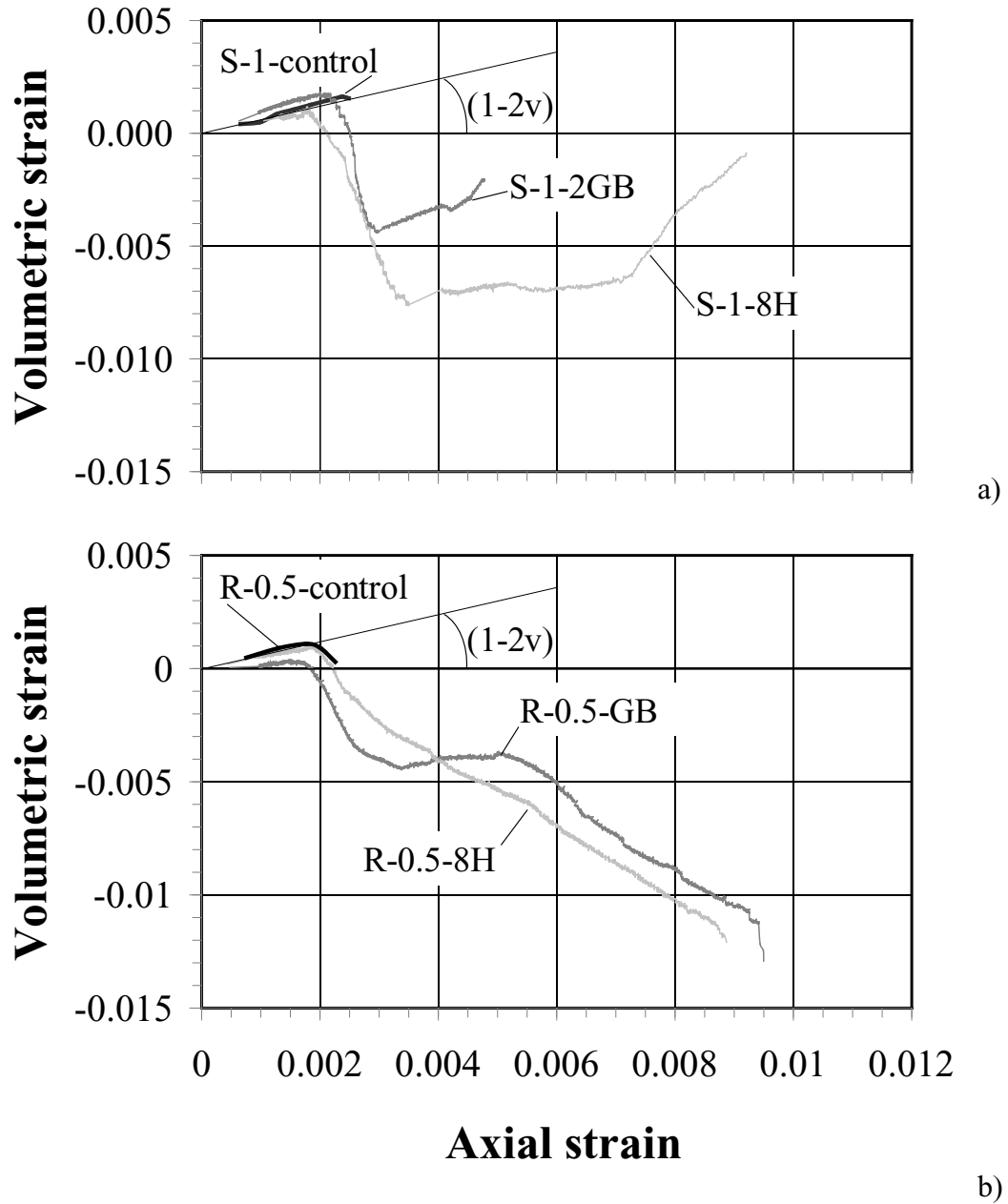


Fig. 15: Volumetric strain-axial strain relationships [series S-1 (a) and R-0.5 (b)].

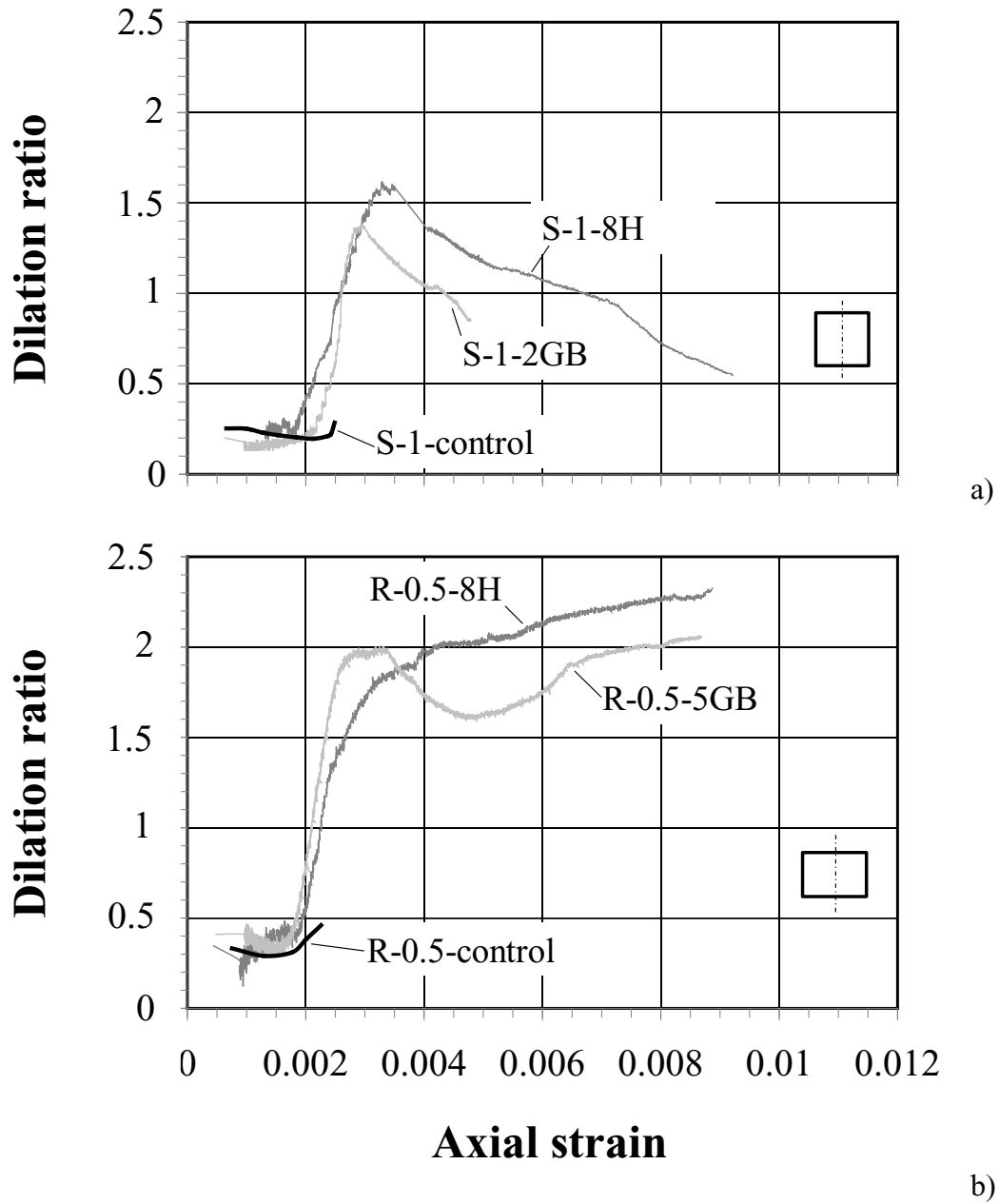


Fig. 16: Dilation ratio-axial strain relationships [series S-1 (a) and R-0.5 (b)].

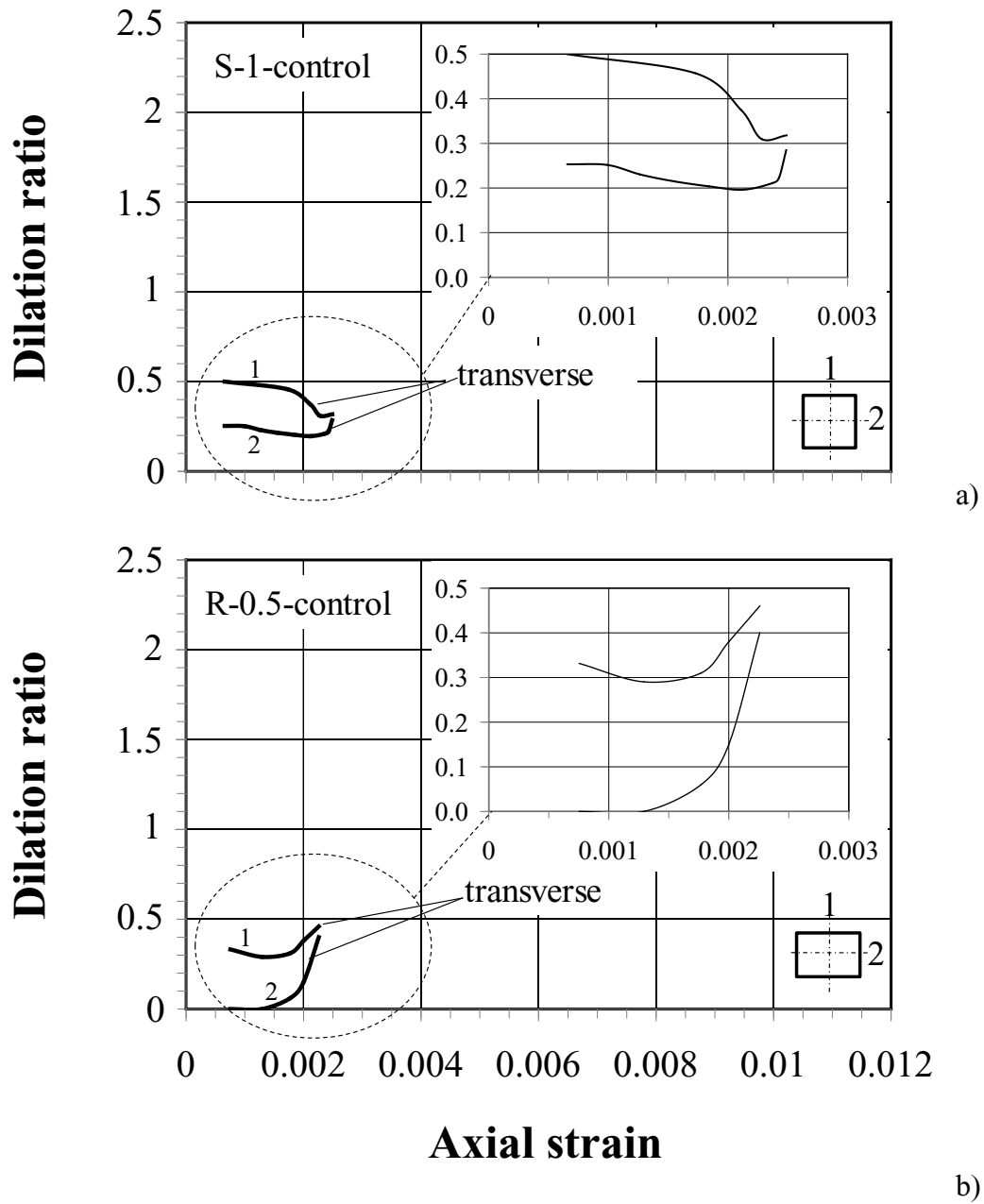


Fig. 17: Dilation ratio-axial strain relationships [specimens S-1-control (a) and R-0.5-control (b)].

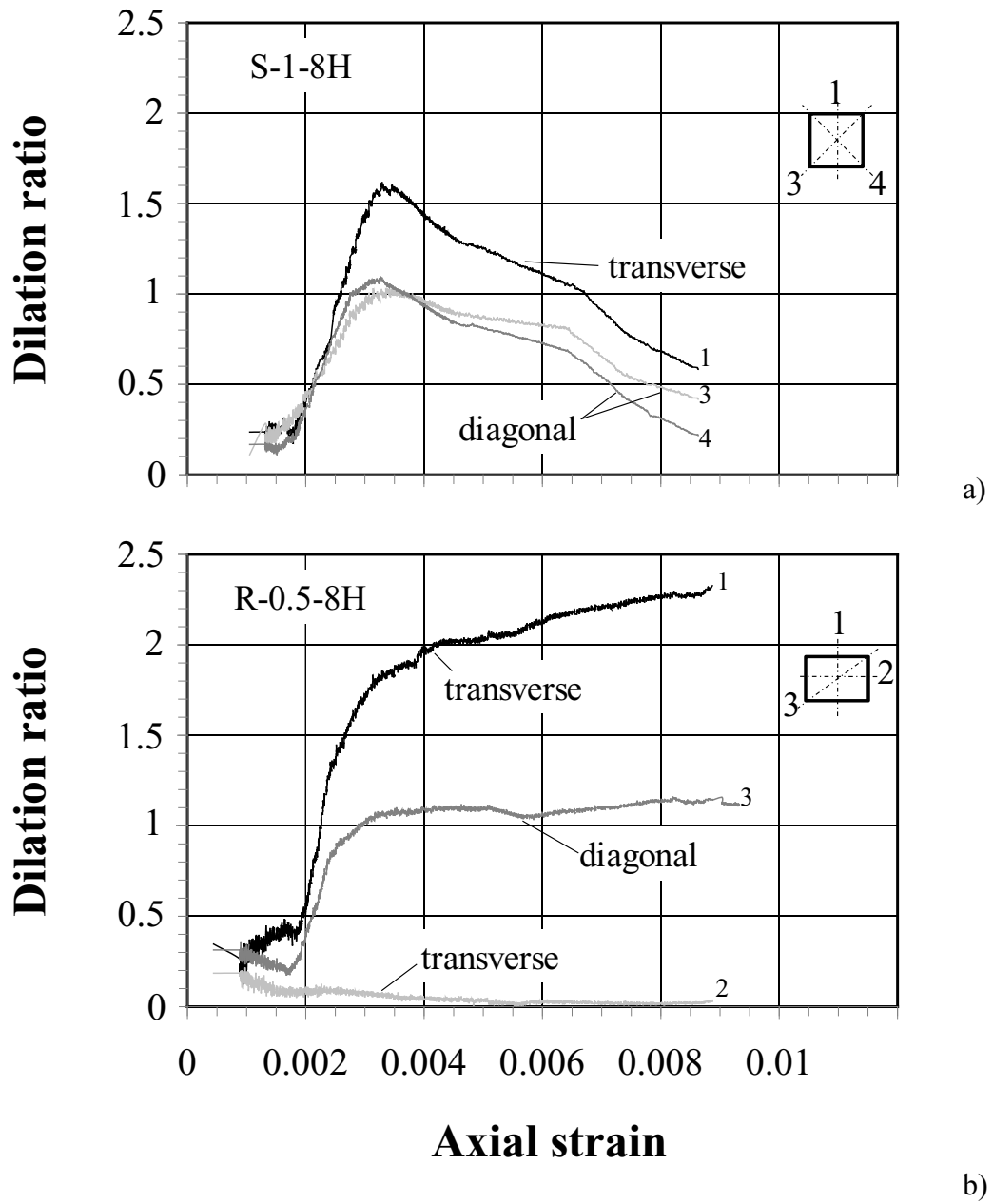


Fig. 18: Dilation ratio-axial strain relationships [specimens S-1-8H (a) and R-0.5-8H (b)].

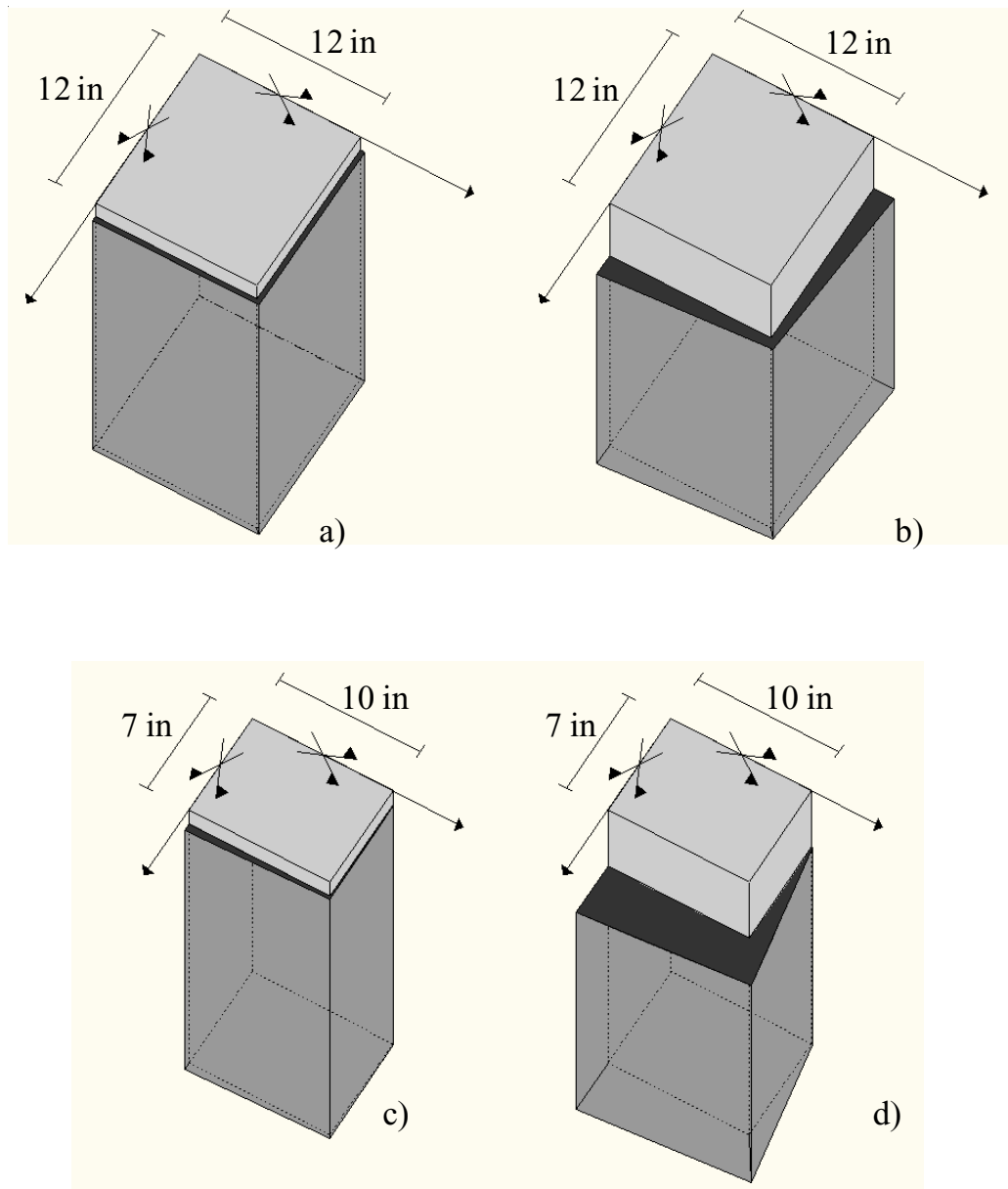


Fig. 19: Change in volume of representative one-quarter unit element for Specimen S-1-8H at peak load (a) and at failure (b) and Specimen R-0.5-8H at peak load (c) and at failure (d).

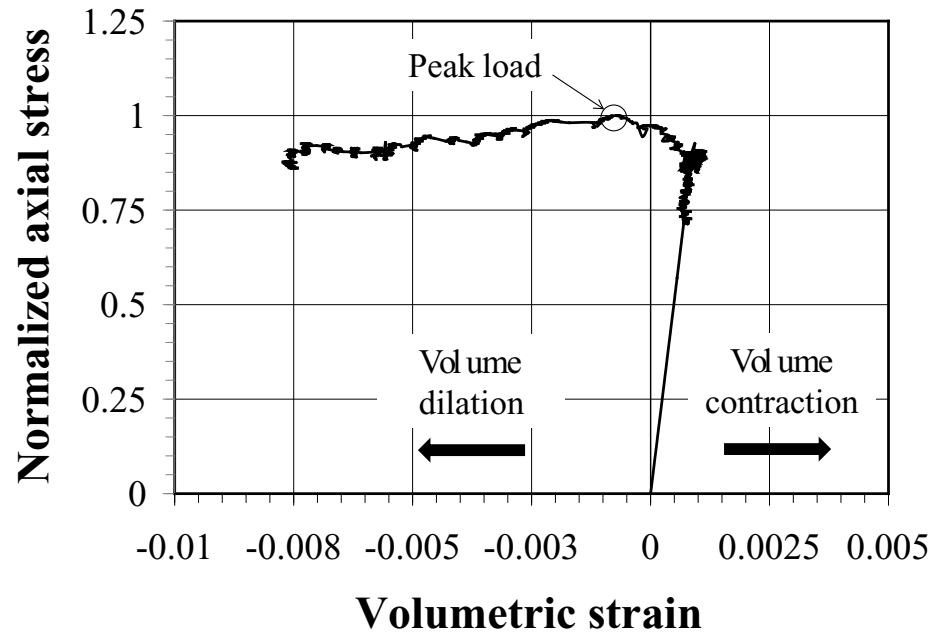


Fig. 20: Typical volumetric strain – normalized axial stress relation for FRP-confined prismatic concrete column.

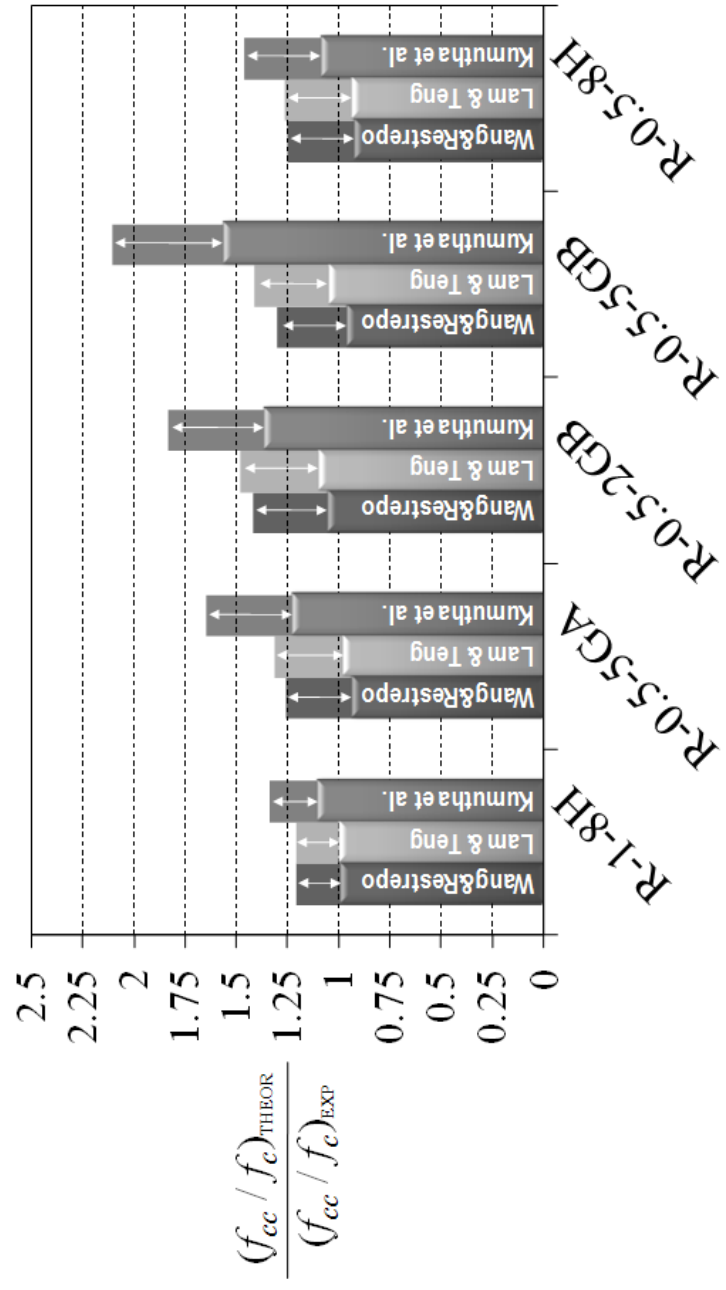


Fig. 21: Predicted concrete axial strength enhancement based on f_c and strength of control column (square columns).

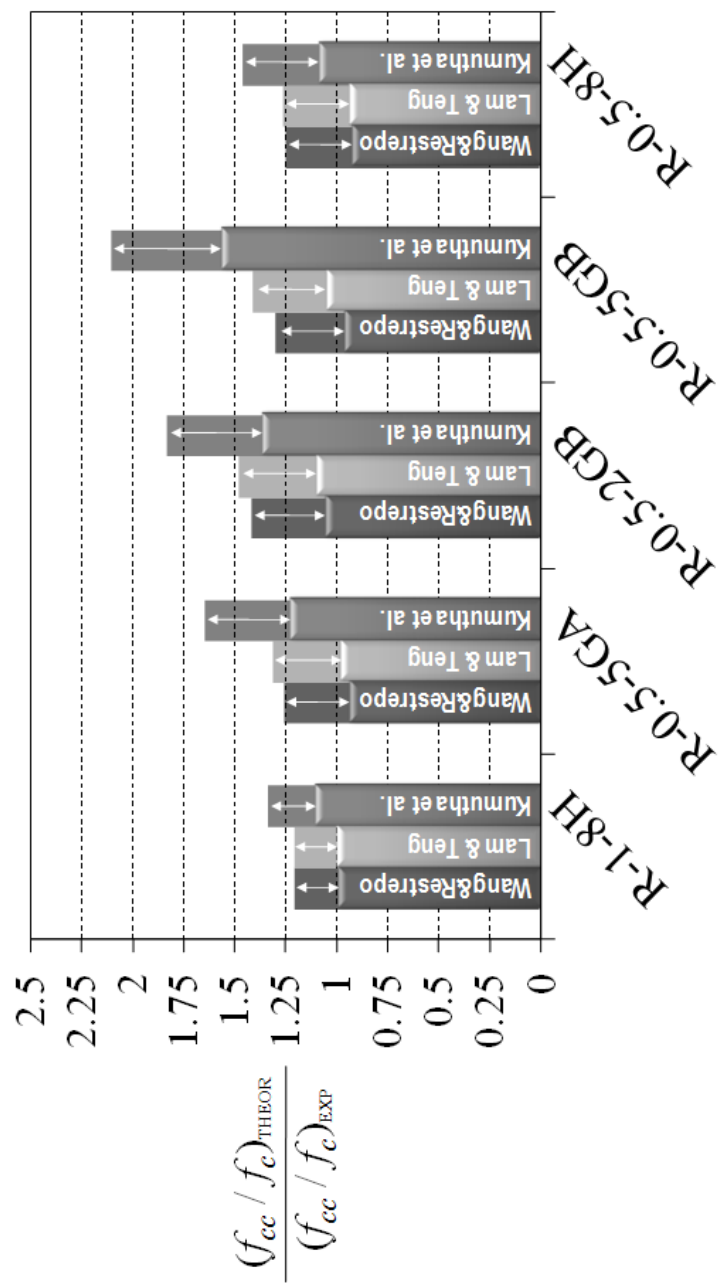


Fig. 22: Predicted concrete axial strength enhancement based on f_c and strength of control column (rectangular columns).

Chapter 4: Study 3 – Single–Parameter Methodology for the Prediction of the Stress- Strain Behavior of Fiber Reinforced Polymer Confined Reinforced Concrete Square Columns

Background

The external confinement of reinforced concrete (RC) columns by means of externally bonded fiber reinforced polymer (FRP) laminates is a well established technique for strengthening and deformability enhancement purposes. In FRP-confined concrete, the properties of the two materials are used in the most desirable and structurally effective manner. The transverse FRP is loaded in tension due to concrete dilation. In turn, concrete is subjected to the lateral pressure provided by the confining FRP jacket. This lateral pressure induces in the concrete a triaxial state of stress and, consequently, an increment in compressive strength and deformation capacity. The nature of the FRP confinement is passive as the lateral pressure induced by the FRP jacket is due to and increases with the growth in volume of the concrete.

The behavior of FRP-confined plain concrete cylinders subjected to pure axial loads has been extensively studied (Nanni and Bradford 1994; Mirmiran and Shahawy 1996; Karbhari and Gao 1997; Spoelstra and Monti 1999; Fam and Rizkalla 2001; Shehata et al. 2002; Campione and Miraglia 2003; Lam and Teng 2003a; Matthys et al. 2005). The

definition of the lateral confining pressure exerted by the FRP jacket on the concrete core is the key to the prediction of the increment of concrete strength. The lateral pressure depends on the strain in the FRP and is “ideally” uniformly distributed around the perimeter of the cross-section. It can be uniquely determined considering force equilibrium and radial displacement compatibility between concrete and FRP jacket. In circular RC columns, the confining effectiveness of the FRP jacket is optimal since the geometrical configuration allows the fibers to be effective on the entire cross section. The final point in the stress-strain curve of the column generally defines both the peak load and the ultimate axial strain. The peak stress is reached when the FRP ruptures and the lateral confining pressure is the maximum pressure possible.

Several analytical models have been developed to describe the behavior of FRP-confined concrete circular columns. The majority of them (Mirmiran and Shahawy 1997; Spoelstra and Monti 1999; Fam and Rizkalla 2001; Harries and Kharel 2002; and Teng et al. 2009) are based on the assumption that axial stress and axial strain of FRP-confined concrete at given lateral strain are the same as those of the same concrete actively confined with a constant confining pressure equal to that supplied by the FRP-jacket (Teng and Lam 2004). These models calculate the axial stress and axial strain of FRP-confined concrete at a given confining pressure by using an active confinement model for concrete. In other words, if the lateral strain – axial strain relationship is known, for a given axial strain the corresponding lateral pressure provided by the FRP jacket can be derived. The axial strain and the lateral pressure can be then used together with an active-confinement based model to evaluate the corresponding axial stress in the column. This incremental

approach ultimately leads to the definition of the entire stress-strain curve (Teng et al. 2009).

Many studies have been carried out on FRP-confined RC square columns in the past years (Pessiki et al. 2001; Shehata et al. 2002; Mirmiran et al. 1997; Rocca et al., 2006; Rocca et al., 2008). It has been widely recognized that the lateral pressure provided by the FRP jacket is not uniform along the cross-sectional perimeter: it is high in proximity of the corners and low along the sides so that the cross-section is only partially confined (Mander et al. 1988; Lam and Teng 2003b). The distribution of the lateral strain along the FRP jacket is not uniform either and the cross-section also changes in shape while concrete grows in volume. FRP confinement still enhances concrete strength and ultimate strain, but its effectiveness is not as tangible as that of jacketing a circular cross-section. While ultimate column failure coincides with rupture of the FRP, the peak capacity of the column occurs at an FRP strain much lower than its ultimate value.

Several theoretical models to predict the peak axial stress for prismatic columns have been developed and proposed (Mirmiran et al 1998; Wang and Restrepo 2001; Campione and Miraglia 2003; Lam and Teng 2003b; Kumutha et al 2007; Wu and Wang 2009). However, their predictive equations do not converge to the same values, and their validity for full-scale columns still has to be proven. Their limitation seems to be due to the fact that these models have been developed from the ones created for circular shapes and modified by means of factors intended to account for the change in cross-sectional shape and its effect on the confining pressure.

The work presented herein proposes a new theoretical methodology to interpret and capture the mechanics of the FRP confinement of square reinforced concrete (RC) columns subjected to pure compressive loads. A single-parameter study for predicting the axial stress – axial strain curve for FRP-confined concrete square columns is discussed.

Methodology fundamentals

The methodology presented herein aims at defining a theoretical frame-work that relates all the factors affecting the FRP confinement of square RC columns to a single independent parameter. It is believed that the increment in compressive strength and deformability capacity depends primarily on the FRP jacket properties (elastic modulus and thickness) if concrete properties and cross-sectional shape are fixed. The independent parameter has been, therefore, recognized in the stiffness of the FRP jacket, $E \cdot t$, defined as the product of the modulus of elasticity of the fibers, E , and the thickness of the jacket, t . The key concept of this methodology is the following: if the stiffness of the jacket is known, then the dilation ratio – axial strain relationship can be uniquely defined and the concrete axial stress – strain curve can be derived.

The main assumption of this methodology is that two boundary conditions can be defined. The lower-bound condition coincides to the case of no external FRP jacket. The upper-bound condition was meant to represent a field application for which an incredibly high quantity of FRP is applied, if compared with amounts conventionally used. It is, therefore, assumed that the stiffness of the FRP jacket, $E \cdot t$, can vary between 0, which is

the value corresponding to the lower bound, and $(E \cdot t)_0$, which is the value corresponding to the upper-bound. This value will be numerically defined in the next sections.

In order to base this methodology on a dimensionless parameter, the term α is then introduced. This parameter is defined as the ratio between the actual FRP jacket stiffness, $E \cdot t$, of the confined square RC column under consideration and the upper-bound FRP jacket stiffness $(E \cdot t)_0$. Lower-bound and upper-bound conditions are therefore defined by $\alpha = 0$ and $\alpha = 1$, respectively.

Description of the theoretical methodology

The experimental outcomes of tested specimens S-1-control, S-1-2GB and S-1-8H, described in Study 2, are herein discussed to validate some of the assumptions made. At this stage, the study refers only to the case of glass and hybrid glass-basalt fibers.

The following parameters are defined as follows:

- ε_0 : concrete axial strain beyond which concrete behavior deviates from the linear elastic behavior;
- ε_{cp} : concrete axial strain which corresponds to the peak axial stress;
- ε_1 : concrete axial strain at which the maximum transverse dilation ratio is

reached;

ε_{cp}^{UC} : lower-bound concrete axial strain corresponding to the peak axial stress;

ε_{cp}^* : upper-bound concrete axial strain corresponding to the peak axial stress;

ε_{cu} : concrete ultimate axial strain;

ε_{FRP} : strain in the FRP jacket in the jacket;

ε_y : steel yield strain;

u : displacement along the x-direction;

v : displacement along the y-direction;

δ_t : displacement of the side mid-point;

δ_{dt} : component of the displacement of the corner point along the x- and the y-directions and l is the cross-section side;

ν_c : Poisson's ratio for concrete;

$\mu_{t@peak}$: transverse dilation ratio when the axial strain corresponding to the axial stress is reached;

$\mu_{t,max}$: maximum transverse dilation ratio;

$\mu_{d,max}$: maximum diagonal dilation ratio;

σ_c : concrete axial stress;

σ_{cp} : concrete peak axial stress

σ_{cp}^{UC} : lower-bound concrete peak axial stress;

- σ_{cp}^* : upper-bound concrete peak axial stress;
 σ_{cu} : concrete ultimate axial stress;
 E_c : concrete stiffness of the initial linear elastic branch of the $\sigma_c - \varepsilon_c$ curve;
 f_c' : compressive strength of a concrete cylindrical sample;
 f_{cc} : compressive strength of a concrete cylindrical sample in a triaxial state of stress;
 f_l : effective lateral pressure confining the concrete core due to the FRP;
 f_y : steel yield stress
 W_{ext} : external work;
 W_{int} : internal work;
 A_g : gross cross-sectional area;
 A_c : net area of concrete;
 ρ_s : steel reinforcement ratio;
 $E \cdot t$: stiffness of the confining FRP jacket.

Experimental dilation ratio – axial strain relationship

Fig. 23a shows the experimental dilation ratio of specimen S-1-8H measured along one of the two transverse directions and along the two diagonals of the cross-section. The transverse dilation ratio, μ_t , is defined as the ratio between the average lateral strain in

the concrete along either one of the two orthogonal directions in the plane of the cross-section and the axial strain, ϵ_c . The diagonal dilation ratio, μ_d , is instead defined as the ratio between the average lateral strain along either one of the two diagonals and the axial strain, ϵ_c . Fig. 23b and Fig. 23c show the change in volume of a representative one-quarter unit element of specimen S-1-8H as the peak load is reached (b) and at failure (c) by plotting the displacements of the mid-points of the two sides and of the corner and the axial shortening. To make the change in volume visible, all changes in length are amplified using the same magnification factor. It is noted that, until the peak axial stress is reached, no cross-sectional shape change is observed. Then, both transverse and diagonal dilation ratios continue to increase until they reach a maximum value after which a slight decrement is observed. For axial strains larger than the peak strain the transverse expansion is higher than the diagonal one.

Theoretical dilation ratio – axial strain relationship

The dilation ratio for axially loaded, unconfined concrete is typically assumed to have a constant value equal to the Poisson's ratio for concrete (ν_c , assumed equal to 0.2), up to an axial stress level of approximately 70% of the axial strain corresponding to the compressive strength of concrete. Beyond 70%, the dilation ratio increases rapidly to a value of about 0.5 when the concrete compressive strength is achieved and is unstable in the post-peak response as the concrete dilates in an uncontrolled manner (Chen 1982).

A family of one-parameter curves is introduced to model the dilation ratio – axial strain behavior of confined concrete (Fig. 24). Each curve is identified as the parameter α is

determined. The transverse dilation ratio, for any $\alpha = \alpha^*$ with $0 < \alpha^* < 1$, is assumed constant and equal to ν_c for axial strains smaller than ε_0 . This value is based on the experimental evidence provided by specimen S-1-control and taken equal to 0.00125. The transverse dilation ratio first increases parabolically from ε_0 until ε_{cp} when it reaches $\mu_{t@peak}$, then linearly from ε_{cp} until ε_1 when it approaches its maximum value, $\mu_{t,max}$.

The FRP confinement becomes effective after that concrete starts deviating from its linear elastic behavior by delaying and limiting unstable crack propagation. As the dilation ratio is not significantly influenced by the FRP confinement until the peak load is reached, $\mu_{t@peak}$ is assumed equal to 0.5 as Chen's model for unconfined concrete does.

Despite the slight decrement of the transverse dilation ratio after reaching its maximum value as shown by the experimental results, at this stage of the analysis, for axial strains larger than ε_1 , the transverse dilation ratio is assumed constant and equal to $\mu_{t,max}$ until failure occurs. Fig. 25 shows the theoretical approximation of the experimental transverse dilation ratio – axial strain curve for specimen S-1-2GB.

The value of ε_1 is defined by the following function with respect to α :

$$\varepsilon_1(\alpha) = \frac{0.0015}{0.5 - 0.125 \cdot \alpha} \quad (3)$$

According to this equation, ε_1 is equal to 0.003 or 0.004 if α is equal to 0 or 1, respectively.

The condition of $\alpha = 0$ corresponds to the case of unconfined concrete (lower-bound). For this case, the axial strain corresponding to the peak stress, ε_{cp}^{UC} , and the ultimate axial strains were fixed equal to 0.0025 and 0.0030, respectively. These values are based on the experimental evidence: specimen S-1-control reaches its peak axial stress when the axial strain is 0.0025 and fails at a value of axial strain equal to 0.003. The maximum value of dilation ratio was assumed approaching infinity.

The condition of $\alpha = 1$ represents the upper-bound condition, for which the maximum transverse dilation ratio is arbitrarily assumed equal to 0.5. It is also assumed that, when $\alpha = 1$, the stiffness of the FRP jacket is so high that no change in shape is observed and therefore maximum transverse and diagonal dilation ratios are both equal to 0.5. The axial strain corresponding to the peak stress, ε_{cp}^* , is arbitrarily assumed equal to 0.004.

The diagonal dilation ratio coincides with the transverse dilation ratio for axial strains smaller than ε_{cp} . As already mentioned, after that the peak axial stress is achieved, the transverse expansion is larger than the diagonal counterpart. The widely acknowledged concept of an area of effective confinement defined by four parabolas within which the concrete is fully confined and outside of which negligible confinement and high dilation occur is herein accepted and justified by the higher dilation ratio along the transverse direction if compared with the ratio measured along the diagonal directions. It is,

therefore, assumed that the maximum value of the diagonal dilation ratio, $\mu_{d,\max}$, is smaller than the maximum transverse, $\mu_{t,\max}$. A window in Fig. 24 also shows the qualitative trend of the diagonal dilation ratio – axial strain curve and compares it with the transverse counterpart.

It is believed that the maximum values of the transverse and diagonal dilation ratios, $\mu_{t,\max}$ and $\mu_{d,\max}$ respectively, increase if the thickness of the FRP jacket decreases. Their dependence on α is as follows:

$$\mu_{t,\max} = \frac{0.5}{\alpha} \quad (4)$$

$$\mu_{d,\max} = \frac{1+\alpha}{4 \cdot \alpha} \quad (5)$$

Equations (4) and (5) are derived by interpolation based on the conditions that: for $\alpha = 1$, both $\mu_{t,\max}$ and $\mu_{d,\max}$ are equal to 0.5; for $\alpha = 1/3$, $\mu_{t,\max}$ and $\mu_{d,\max}$ are equal to 1.5 and 1.0 respectively; and for $\alpha = 0$, both $\mu_{t,\max}$ and $\mu_{d,\max}$ approach infinity.

FRP membrane strain

Fig. 26 shows the qualitative cross-section deformed shape at different levels of axial strain. As already mentioned, it is herein assumed that no change in shape is observed until the axial strain corresponding to the peak load, ε_{cp} , is reached. For axial strain larger than ε_{cp} , the cross-section deformed shaped is assumed to be approximated by four

identical parabolas which can be uniquely defined if the displacements of the side mid-point and the corner are known.

In order to describe the in-plane deformation of the cross-section, the following assumptions are made:

- the four sides of the FRP jacket are modeled as membranes;
- the corner radius is neglected;
- corners are modeled as internal hinges in the FRP;
- side mid-points displace along the transverse directions (orthogonally to the sides);
- corner points displace along the diagonal directions;
- x- and y-directions are axes of geometrical and mechanical symmetry; and
- the axial strain is constant over the entire cross-section.

Based on this, the displacement along the x- and the y- directions, named u and v , respectively, are defined as follows:

$$u = \frac{2}{l} \cdot \delta_{dt} \cdot x \quad (6)$$

$$v = \frac{4}{l^2} \cdot (\delta_{dt} - \delta_t) \cdot x^2 + \delta_t \quad (7)$$

where δ_t is the displacement of the side mid-point, δ_{dt} is the component of the displacement of the corner point along the x- and the y- directions and l is the cross-section side. They are defined by the following expressions:

$$\delta_t = \frac{1}{2} \cdot \mu_t \cdot \varepsilon_c \cdot l \quad (8)$$

$$\delta_{dt} = \frac{1}{2} \cdot \mu_d \cdot \varepsilon_c \cdot l \quad (9)$$

Because the FRP jacket is modeled as a membrane (bending stresses are disregarded), the strain in the FRP jacket in the jacket, ε_{FRP} , can be written as follows (Giangreco 1969):

$$\varepsilon_{FRP} = \frac{\partial u}{\partial x} + \frac{1}{2} \cdot \left(\frac{\partial v}{\partial x} \right)^2 = \mu_d \cdot \varepsilon_c + \frac{8}{l^2} \cdot (\mu_d - \mu_t)^2 \cdot \varepsilon_c \cdot x^2 \quad (10)$$

The maximum strain in the FRP is achieved in proximity of the corners (for $x = \pm l/2$) and is equal to:

$$\varepsilon_{FRP, \max} = \mu_d \cdot \varepsilon_c + 2 \cdot (\mu_d - \mu_t)^2 \cdot \varepsilon_c \quad (11)$$

Experimental concrete axial stress – axial strain curve

The experimental concrete axial stress – axial strain curves discussed herein are defined disregarding the contribution of the longitudinal reinforcing steel. The ultimate capacity of specimen S-1-control was attained when the average concrete axial stress was equal to about 78% of the average concrete compressive strength, f'_c (Fig. 27a). Peak and ultimate

axial strains were about 0.00214 and 0.00293, respectively. With respect to the unconfined specimen, the increment in concrete strength due to confinement was about 5% and 8% for S-1-2GB and S-1-8H, respectively (Fig. 27b). The peak axial strain was 0.00293 and .00211 for S-1-2GB and S-1-8H, respectively. The plots in Fig. 27b was interrupted when the load reached about 75% of the peak load.

Theoretical concrete axial stress – axial strain curve

The axial stress – axial strain model adopted for FRP-confined concrete is the one based on the equation originally proposed by Popovics (1973) and used in the model by Mander et al. (1988) for steel-confined concrete. The selection of this type of curve is based on the fact that both actively confined circular concrete columns and FRP-confined square concrete column (for FRP jackets of thickness representative of a real field application) feature a softening branch after reaching the peak load. The axial stress – axial strain equation is the following:

$$\sigma_c = \frac{(\varepsilon_c / \varepsilon_{cp}) \cdot r \cdot \sigma_{cp}}{r - 1 + (\varepsilon_c / \varepsilon_{cp})^r} \quad (12)$$

where σ_c and ε_c are the axial stress and the axial strain of concrete, σ_{cp} and ε_{cp} are the peak axial stress and the corresponding axial strain for a certain level of FRP confinement. The constant r is defined as in Carreira and Chu (1985) as:

$$r = \frac{E_c}{E_c - \sigma_{cp} / \varepsilon_{cp}} \quad (13)$$

The constant E_c is representative of the stiffness of the initial linear elastic branch of the $\sigma_c - \varepsilon_c$ curve and is defined as follows based on the experimental evidence of the control specimen:

$$E_c = 0.8 \cdot f'_c / \varepsilon_0 \quad (14)$$

where f'_c is the compressive strength of a concrete cylindrical sample and ε_0 is the axial strain after which the concrete is not linear elastic any more. This value is taken equal to 0.00125.

Concrete peak axial stress and corresponding axial strain

Based on the experimental evidence derived from testing specimen S-1-control, Popovics curve for unconfined concrete is plotted with the peak axial stress, σ_{cp}^{UC} , and its corresponding axial strain, ε_{cp}^{UC} , equal to $0.8 \cdot f'_c$ and 0.0025, respectively. Fig. 27a shows that the theoretical normalized axial stress – axial strain curve approximates quite well the experimental one.

To remedy the lack of experimental data, it is herein assumed that (this assumption will be justified later in this section) if the control specimen was confined with a jacket of stiffness, $(E \cdot t)_0$ (where E is the modulus of elasticity of the fibers and t is the thickness of the jacket), equal to 1,461,600 lb/in (256.2 kN/mm) the peak axial stress, σ_{cp}^* , would be equal to f'_c and the axial strain corresponding to the peak stress, ε_{cp}^* , equal to 0.004.

The normalized axial stress – axial strain curve corresponding to this theoretical upper-bound condition is shown in Fig. 27a.

It is also assumed that if the stiffness of the confining FRP jacket, $E \cdot t$, varies between 0 and $(E \cdot t)_0$, the corresponding peak axial strain, σ_{cp} , and axial stress, ε_{cp} , lie on the straight line b plotted in Fig. 27a. The equation of b can be written as follows:

$$\sigma_{cp} = \frac{\sigma_{cp}^* - \sigma_{cp}^{UC}}{\varepsilon_{cp}^* - \varepsilon_{cp}^{UC}} \cdot (\varepsilon_{cp} - \varepsilon_{cp}^{UC}) + \sigma_{cp}^{UC} \quad (15)$$

Experimental research (Richart 1928) has shown that in presence of a triaxial stress state, the effective pressure, f_{cc} , determining the failure of a cylindrical concrete specimen is:

$$f_{cc} = f_c' + k \cdot f_l \quad (16)$$

where f_l is the effective lateral pressure confining the concrete core due to the FRP and k is an experimental coefficient. As discussed above, when the peak load is reached, no significant change in cross-sectional shape is observed and the transverse dilation ratio, μ_t , can be assumed equal to 0.5. The lateral stress in the FRP jacket, σ_{FRP} , can be, therefore, approximated as constant over each side and equal to:

$$\sigma_{FRP} = E \cdot t \cdot \varepsilon_{FRP} = E \cdot t \cdot \mu_{t@peak} \cdot \varepsilon_{cp} \quad (17)$$

where ε_{FRP} is the membrane strain in the FRP jacket and $\mu_{t@peak}$ is the transverse dilation ratio when the peak axial strain is reached. By considering the equilibrium between FRP jacket and concrete, a fictitious lateral pressure, σ_{lat} , can be defined and expressed as follows:

$$\sigma_{lat} = 2 \cdot \frac{E \cdot t}{l} \cdot \mu_{t@peak} \cdot \varepsilon_{cp} \quad (18)$$

where l is the side of the cross-section. By replacing f_{cc} with σ_{cp} , f'_c with σ_{cp}^{UC} and f_l with σ_{lat} , equation (16) can be written as follows:

$$\sigma_{cp} = \sigma_{cp}^{UC} + k \cdot 2 \cdot \frac{E \cdot t}{l} \cdot \mu_{t@peak} \cdot \varepsilon_{cp} \quad (19)$$

The parameter α is then introduced. Posing:

$$k_1 = k \cdot 2 \cdot (E \cdot t)_0 / l = 100 \quad (20)$$

and solving simultaneously equations (15) and (19) for ε_{cp} and σ_{cp} , the peak axial stress and the corresponding axial strain can be written as function of the only parameter α :

$$\sigma_{cp}(\alpha) = \frac{k_1 \cdot \alpha \cdot \mu_{t@peak} \cdot (\varepsilon_{cp}^{UC} \cdot \sigma_{cp}^* - \varepsilon_{cp}^* \cdot \sigma_{cp}^{UC}) + \sigma_{cp}^{UC} \cdot (\sigma_{cp}^* - \sigma_{cp}^{UC})}{(\sigma_{cp}^* - \sigma_{cp}^{UC}) - k_1 \cdot \alpha \cdot \mu_{t@peak} \cdot (\varepsilon_{cp}^* - \varepsilon_{cp}^{UC})} \quad (21)$$

$$\varepsilon_{cp}(\alpha) = \frac{\varepsilon_{cp}^{UC} \cdot (\sigma_{cp}^* - \sigma_{cp}^{UC})}{(\sigma_{cp}^* - \sigma_{cp}^{UC}) - k_1 \cdot \alpha \cdot \mu_{t@peak} \cdot (\varepsilon_{cp}^* - \varepsilon_{cp}^{UC})} \quad (22)$$

The FRP jacket of specimen S-1-2GB is characterized by a thickness, t , of 0.0464 in (1.18 mm) and modulus of elasticity, E , of 10,500,000 psi (72.4 GPa) with a stiffness, $E \cdot t$, equal to 487,200 lb/in (85.4 kN/mm), which corresponds to α equal to 0.333. The stiffness, $E \cdot t$, of the jacket of specimen S-1-8H is 443.3 lb/in (76.9 kN/mm) which corresponds to α equal to 0.3. The theoretical curves for $\alpha = 0.333$ (S-1-2GB) and for $\alpha = 0.3$ (S-1-8H) are both plotted in Fig. 27b. By defining $(E \cdot t)_0$ equal to 1,461,600 lb/in (256.2 kN/mm) and k_1 equal to 100, Popovics' curve with σ_{cp} and ε_{cp} defined by (21) and (22) for $\alpha = 0.333$ and $\alpha = 0.3$ approximates quite well the experimental results.

Ultimate concrete compressive axial strain

To define the ultimate concrete compressive strain, ε_{cu} , an energy balance approach (Mander et al. 1988) is followed. The additional capacity in deformability available when concrete is confined is considered to be due to the energy stored in the FRP jacket. The energy balance consists in equating the external work to the internal work. The external work, W_{ext} , is equal to the energy adsorbed by the concrete and by the longitudinal internal steel reinforcement. The internal work, W_{int} , is equal to the energy stored in the FRP jacket, neglecting the contribution of the transverse steel reinforcement. Energy dissipation is also neglected. Under the assumption that $\varepsilon_{cu} > \varepsilon_y$, the external work, W_{ext} , can be written as follows:

$$W_{ext} = A_c \cdot \int_0^{\epsilon_{cu}} \sigma_c(\epsilon_c) \cdot d\epsilon_c + \rho_s \cdot A_g \cdot f_y \cdot (\epsilon_{cu} - 0.5 \cdot \epsilon_y) \quad (23)$$

where A_c is the net area of concrete, $\sigma_c(\epsilon_c)$ is the axial stress – axial strain curve defined for confined concrete, ρ_s is the steel reinforcement ratio, A_g is the gross cross-sectional area, f_y and ϵ_y are the steel yield stress and yield strain, respectively. The internal work, W_{int} , is given by the following expression:

$$W_{int} = 4 \cdot E \cdot t \cdot \int_{-l/2}^{l/2} [\epsilon_{FRP}(x)]^2 \cdot dx \quad (24)$$

where $E \cdot t$ is the stiffness of the FRP jacket, l is the length of the cross-section side and $\epsilon_{FRP}(x)$ expresses the lateral strain in function of the location along the side of the cross-section when the ultimate concrete axial strain is reached. By equating equations (23) and (24), the axial concrete compressive strain, ϵ_{cu} , at the stage of first rupture of the FRP jacket can be numerically solved for. An example is showed in Appendix 4.

Design approach

As an example, this methodology is applied to the case of a square concrete column of side, l , equal to 24 in. (610 mm) and concrete compressive strength of 5,000 psi (34.5 MPa). An example of design table is shown in Table 8. For different values of α , the following is derived: ratio in concrete compressive strength with respect to the

unconfined concrete strength, $\sigma_{cp}/\sigma_{cp}^{UC}$; concrete peak axial stress normalized with respect to the concrete compressive strength, σ_{cp}/f'_c ; concrete peak axial strain, ϵ_{cp} ; concrete ultimate axial stress normalized with respect to the concrete compressive strength, σ_{cu}/f'_c ; concrete ultimate axial strain, ϵ_{cu} ; concrete axial strain corresponding to 75% the peak axial stress, $\epsilon_{c@75\%\sigma_{cp}}$; tensile strain in the FRP jacket when failure occurs, $\epsilon_{lat,u}$; stiffness of the FRP jacket, $E \cdot t$. The last three columns translate the stiffness of the FRP jacket in number of plies for three different types of fibers, namely glass A, glass B and hybrid glass-basalt as their properties are defined in Study 2.

For example, if concrete compressive strength is to be increased of 10%, Table 8 can be used to define the necessary amount of FRP. Looking at the second column ($\sigma_{cp}/\sigma_{cp}^{UC}$), the value of α which induces the increment of concrete strength closest to 10% can be determined. For $\alpha=0.5$, $\sigma_{cp}/\sigma_{cp}^{UC}$ is equal to 1.096. If type A glass fibers are selected 7 plies are needed. The needed number of plies to induce the same increment of strength would be 4 and 14 for type B glass and for glass/basalt, respectively. Once the number of plies is designed, it has to be finally checked that tensile strain in the FRP jacket when failure occurs, $\epsilon_{lat,u}$, is smaller than the ultimate FRP tensile strain. Also, given the value of α , in this case $\alpha=0.5$, concrete axial stress – axial strain curve can be generated and ultimately used for the development of P-M diagrams.

Conclusions

All the assumptions made above are summarized and discussed as follows.

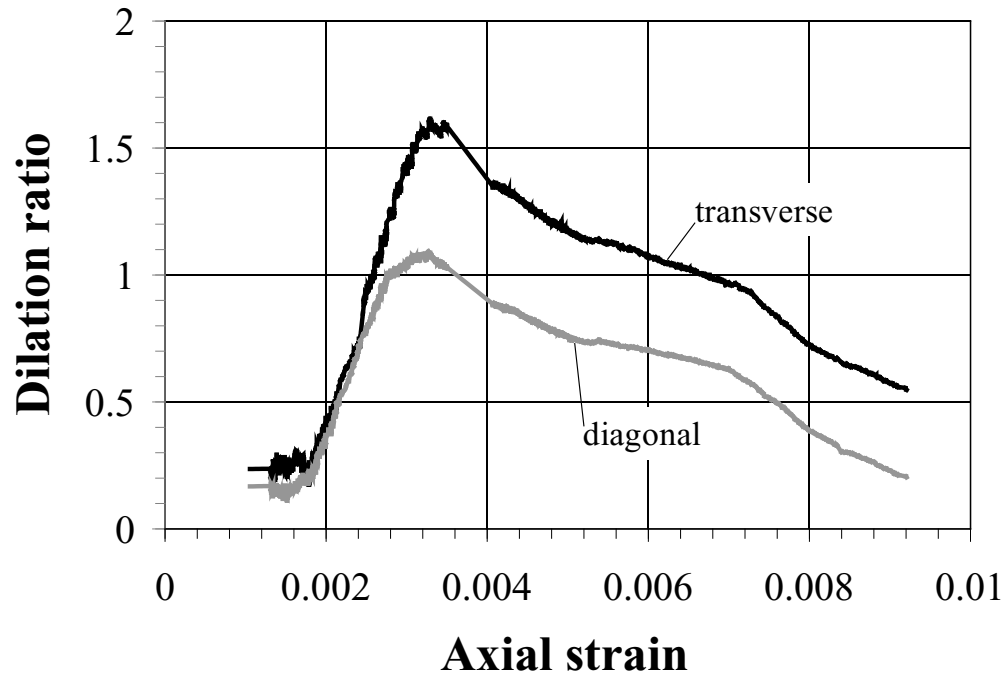
1. The highly-confined concrete (upper-bound limit) condition ($\alpha = 1$), necessary to the functionality of the methodology, was arbitrarily defined based on common-sense considerations given the lack of experimental data. It was meant to represent an uncommon field application for which a considerable quantity of FRP was applied, if compared with the amount usually used in real application. In particular, it was arbitrarily assumed that such high quantity of FRP was able to induce an increment of concrete strength of 25% with respect to an unconfined column.
2. The commonly accepted concept, according to which FRP confinement contributes to increase concrete axial peak stress and strain, was simplified by the relation (15). This simplification and the definition of the coefficient k_I , defined by (20), were based on the few data points available.
3. One of the three conditions imposed to derive relations (4) and (5) was based on the assumption that for a high level of confinement, such as the one represented by the condition $\alpha = 1$, the cross-section remains square until failure occurs. For this situation the maximum dilation ratio is assumed equal to 0.5. The other two conditions were based on experimental evidence: the second assumed that for unconfined concrete the dilation ratio approaches infinity at failure; the third assumed maximum transverse and diagonal dilation ratios equal to 1.5 and 1.0, respectively, for $\alpha = 0.333$.

4. The experimental results showed a slight decrement of the transverse/diagonal dilation ratio after reaching its maximum value. Given the small amount of experimental data to base the analysis on, it appears difficult to understand the nature of the slope and to identify the parameters on which it depends. Therefore, at this stage, the transverse/diagonal dilation ratio is assumed constant after it reaches its maximum value.
5. Transverse/diagonal dilation ratio – axial strain curves are influenced not only by the modulus of elasticity and the thickness of the jacket but also by the type of fibers. However, it is believed that the validity of the theoretical framework is independent from the type of fibers. At this stage, given the lack of data for the case of carbon fibers, this study refers only to the case of glass and hybrid glass-basalt FRP systems.

The lack of experimental data does not allow a complete validation of the methodology discussed above which, however, is believed to be theoretically sound. More experimental data would allow to validate the assumptions made or to modify them in agreement with new experimental evidence. Also, if the curves transverse/diagonal dilation ratio – axial strain were available for different lengths of cross-section sides, for different concrete compressive strengths and for different type of fibers (glass or carbon), then this framework could become a methodology useful to designers and practitioners to design the thickness of the FRP jacket (after that type of fibers has been selected) necessary to induce a needed increment of column compressive strength. Ultimately the axial stress – axial strain curve for concrete can be used for P-M diagram development.

Table 8: Example of design table

$\sigma_{cp}/\sigma_{cp}^{UC}$	σ_{cp}/f_c	ϵ_{cp}	σ_{out}/f_c	ϵ_{cu}	$\epsilon_{c@75\%}\sigma_{cp}$	$\epsilon_{lat,u}$	Et [lb/in]	No. plies Glass A	No. plies Glass B	No. plies Hybrid
1.037	0.830	0.00272	0.784	0.00350	-	0.0149	321,552	3	2	6
1.041	0.833	0.00275	0.721	0.00410	0.00385	0.0158	350,784	4	2	7
1.045	0.836	0.00277	0.653	0.00470	0.00390	0.0164	380,016	4	2	7
1.049	0.839	0.00279	0.596	0.00525	0.00400	0.0168	409,248	4	2	8
1.053	0.842	0.00282	0.547	0.00578	0.00405	0.0170	438,480	5	2	8
1.063	0.850	0.00288	0.448	0.00715	0.00420	0.0175	511,560	5	3	10
1.073	0.859	0.00294	0.382	0.00851	0.00441	0.0176	584,640	6	3	11
1.096	0.877	0.00307	0.297	0.0115	0.00485	0.0177	730,800	7	4	14
1.163	0.930	0.00348	0.199	0.0223	0.00623	0.0190	1,096,200	11	5	20
1.250	1.000	0.00400	0.159	0.0425	0.00850	0.0217	1,461,600	14	6	27



a)

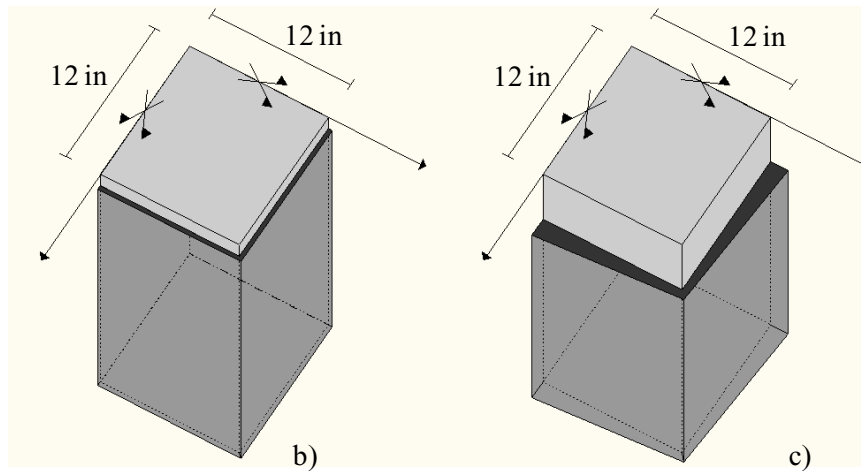


Fig. 23: Experimental transverse and diagonal dilation ratio – axial strain relationship (a). Change in volume of Specimen S-1-8H at peak load (b) and at failure (c).

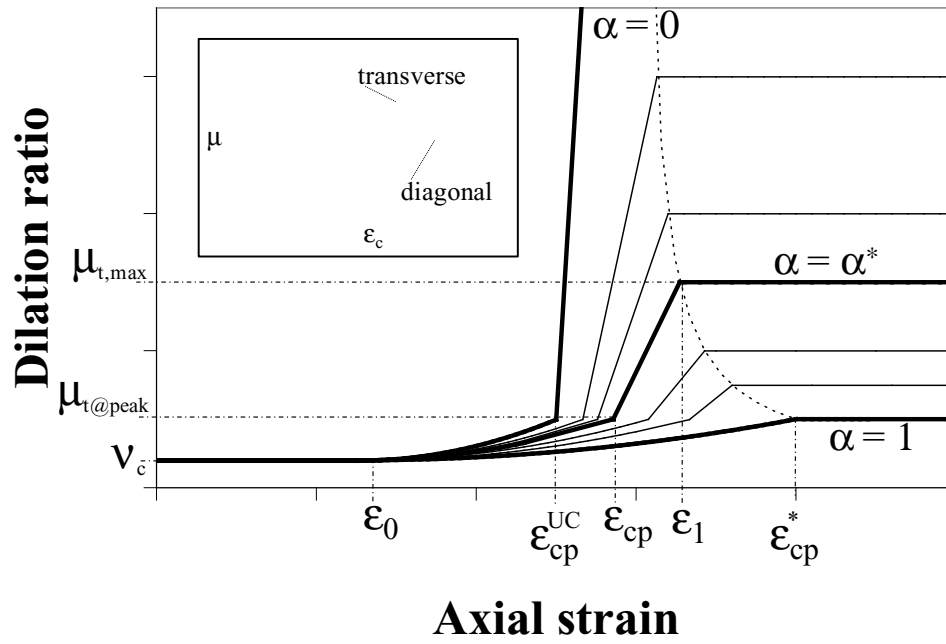


Fig. 24: Theoretical dilation ratio – axial strain curves.

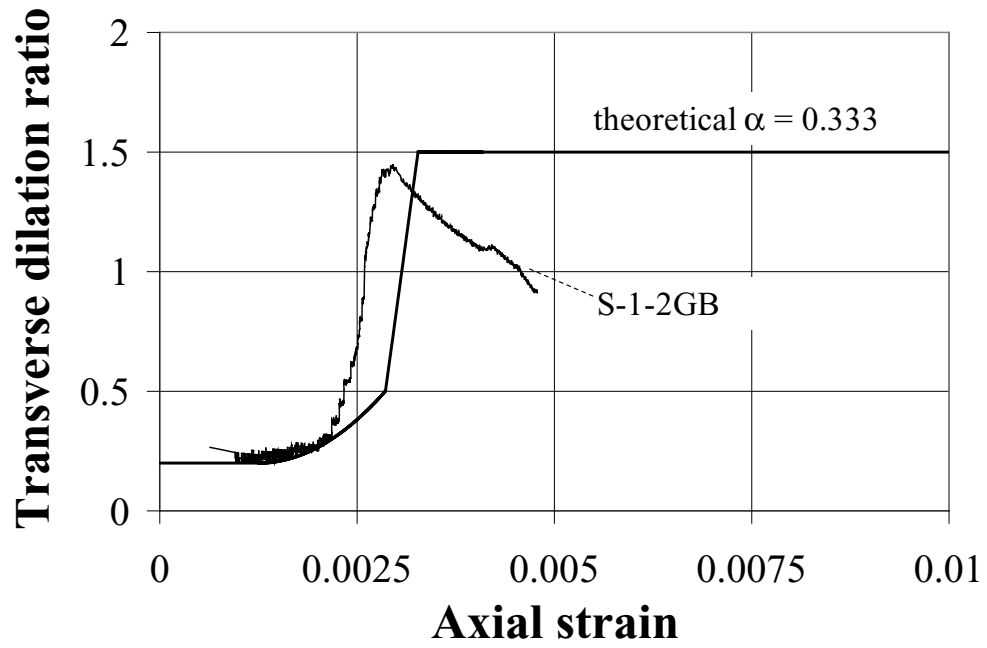


Fig. 25: Experimental versus theoretical transverse dilation ratio for specimen S-1-2GB.

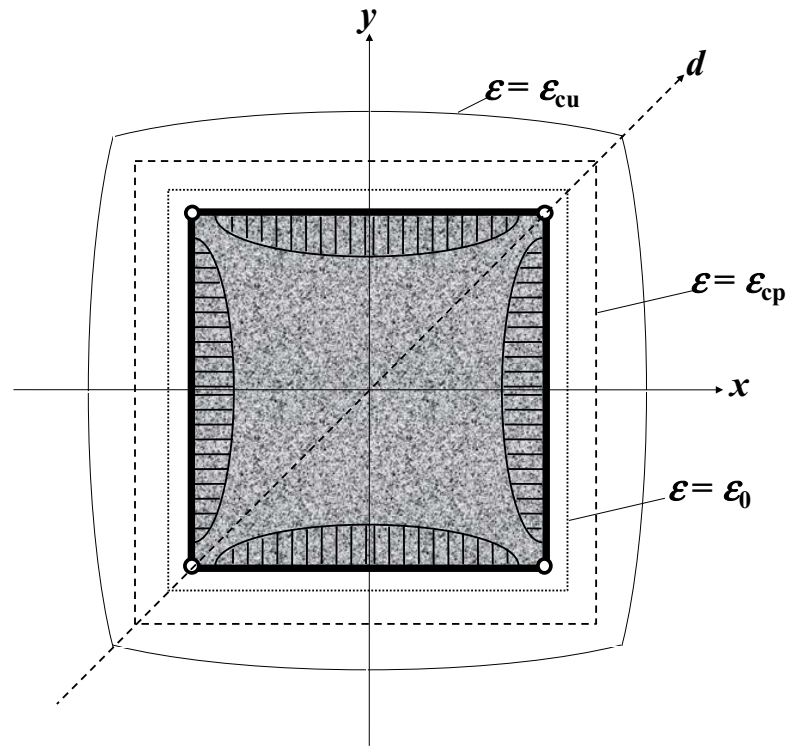


Fig. 26: Qualitative cross-section deformed shape at different levels of axial strain.

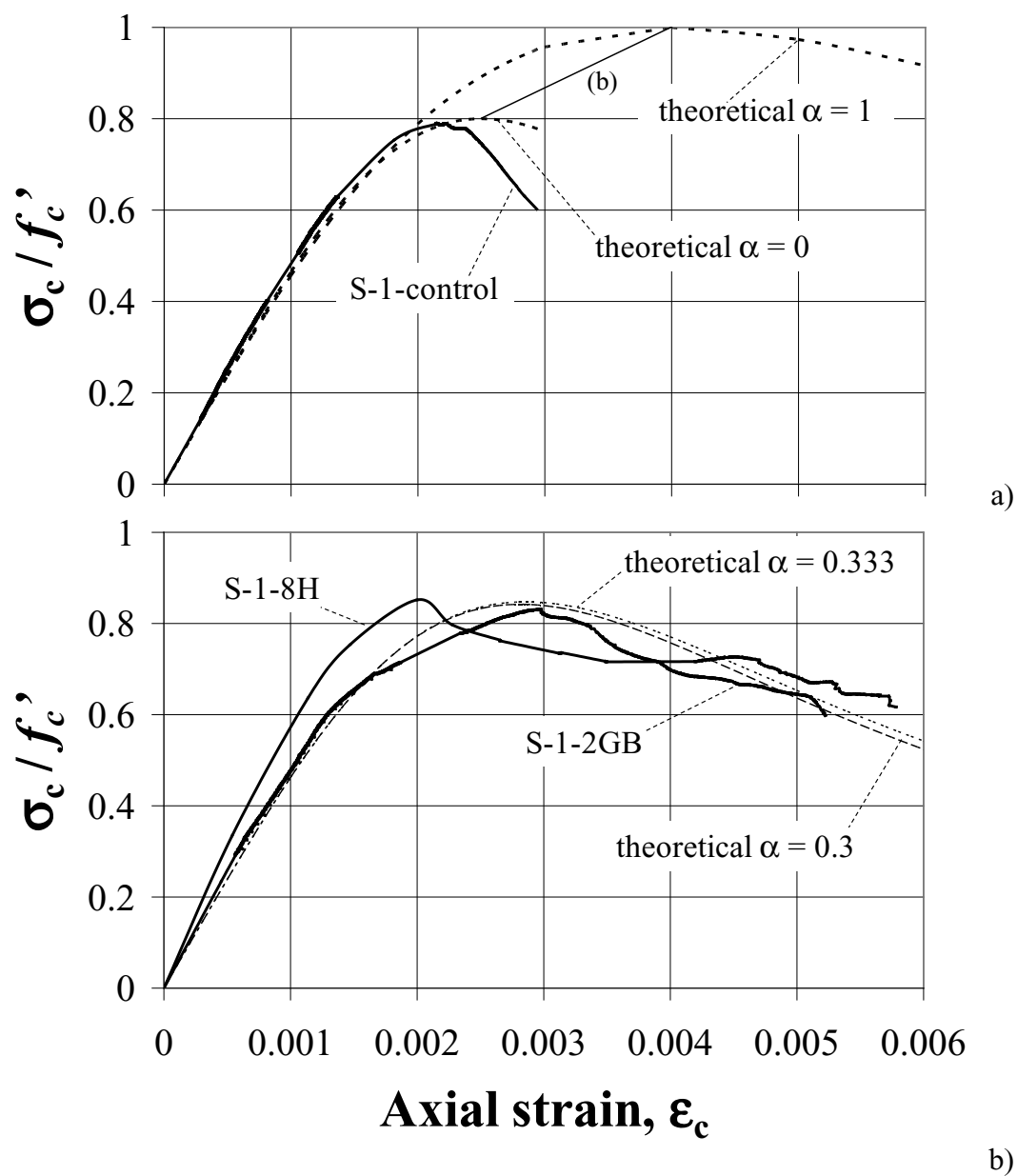


Fig. 27: Experimental curves for specimen S-1-control (a), S-1-2GB (b) and S-1-8H (b) compared with the theoretical ones, for α equal to 0, 0.333 and 0.3, respectively.

Chapter 5: Conclusions

Experimental outcomes

The experimental evidence gained through the full-scale experiments presented in Study 1 is herein summarized:

1. The behavior of RC columns internally reinforced with GFRP bars is similar to that of conventional steel RC columns if the longitudinal reinforcement ratio is equal to 1.0%. No appreciable difference was observed in terms of ultimate capacity.
2. The use of longitudinal GFRP bars is not detrimental to the performance of RC columns.
3. The smaller spacing of the GFRP ties does not contribute to increasing the ultimate capacity, but strongly influences the failure mode by delaying the buckling of the longitudinal bars, initiation and propagation of unstable cracks, and crushing of the concrete core.
4. Difference in the GFRP bar manufacturers does not affect the performance when bars are of comparable quality.

Based upon the experimental evidence gained through the full-scale experiments presented in Study 2, the following conclusions are drawn:

1. The axial load–axial deformation behavior of a prismatic concrete column laterally confined by means of an FRP jacket of thickness representative of field applications is characterized by a linear elastic branch almost up to the peak load and by a descending post-peak branch until failure.
2. FRP confinement effectiveness is more significant in terms of enhancement of concrete axial deformation rather than for the increment of concrete axial strength. The presence of the FRP jacket allows a stable “growth” in volume of the concrete core by offsetting buckling of the vertical reinforcing bars and restraining unstable crack propagation.
3. The shape of the cross-section influences the effectiveness of the confinement. Effectiveness is higher for the square shapes than for the rectangular ones. However, effectiveness decreases when the side aspect ratio of a rectangular cross-section increases. The transverse expansion of the concrete core in the plane of the cross-section, defined by means of the dilation ratio, changes with the direction along which it is evaluated.
4. Difference in the FRP material manufacturers does not affect the performance when confining materials are of comparable quality.

Intellectual merit

The behavior of GFRP RC columns and FRP-confined RC columns is investigated testing full-scale specimens subjected to pure axial load. The experimental programs

presented in Study 1 and Study 2 are unique activities to advance knowledge and understanding. The full-scale testing is the key novelty for both studies.

The condition of pure axial load is not representative of the true behavior of a column but it appears critical to understand the column behavior in terms of axial stress–axial strain relation. The volumetric response (at the level of the mid-height cross-section) of the column specimens is also investigated. The definition of the volumetric strain–axial strain and dilation ratio–axial strain relations is functional to the investigation of: the post-peak softening branch of the column axial stress – axial strain curve; the influence of the lateral GFRP ties at different spacings; and the effectiveness of the GFRP confinement on prismatic cross-sections of different shapes are explained.

Full-scale testing under pure axial load includes several problematic aspects. There are difficulties with aligning the center of loading with the center of the column which, if not taken care of, may compromise the outcomes of the tests. The high cost of a full-scale test limits its replication.

Study 3 shows a single-parameter methodology for interpreting and capturing the mechanics of the FRP confinement of square RC columns subjected to pure compressive loads. The methodology delineates a new theoretical frame-work based on which the entire axial stress – axial strain curve of concrete confined with glass and glass-basalt FRP can be predicted. The novelty of the method lies in the definition of the dilation ratio – axial strain relationship as the underpinning concept.

Broader impact

The limitation to specimens subjected to pure axial loading conditions and the lack of evidence on design-related issues such as creep and fire rating preclude this study from proposing an immediate change of the ACI 440.1R guidelines to include design criteria for compression members in terms of definition of longitudinal and transverse reinforcement. However, Study 1 provides more experimental evidence to understand the behavior of the GFRP bars as internal reinforcement in compression members.

Study 2 provides more experimental data on the performance of FRP-confined RC prismatic columns. In future research, small-scale tests may be designed based on the full-scale ones described herein to demonstrate whether specimen size affects column performance.

Study 3 offers a new theoretical frame-work for the design of the thickness of the glass or glass-basalt FRP jacket necessary to induce a needed increment of column compressive strength. The frame-work includes the prediction of the axial stress – axial strain for concrete which ultimately can be used for the development of P-M diagram.

Future development

To claim the inclusion of the GFRP reinforced columns into the current practice further research is needed. The effects of flexure and shear should be considered. Reliability-based strength-reduction factors should be defined. Economically-efficient tie spacing

that prevents brittle failure of the concrete column should be investigated.

The condition of concentric loads is quite uncommon for columns given that they always transmit axial compressive loads together with bending moments. More evidence is, therefore, needed to evaluate the effects of eccentric loads on the behavior of both FRP-reinforced and FRP-confined RC columns.

More experimental data are also necessary for a complete validation of the methodology discussed in Study 3. More experimental data would allow to corroborate the assumptions made or to modify them to reflect new experimental evidence. The methodology is at this stage limited to glass or glass-basalt fibers. Further research is needed to extent its validity to carbon fibers.

Recommendations for future research

To allow the inclusion of GFRP reinforced columns into the current practice, design issues related with creep and fire rating have to be addressed. Further research is needed in this direction.

Further research is also needed to investigate the behavior of FRP-confined RC columns subjected to cyclic lateral loads.

Tests done on rectangular hollow-core columns and wall-like columns externally confined by means of GFRP laminates and subjected to pure axial load only are described

in the Appendix 6 and 7, respectively. More research is needed to validate the efficiency of the confinement on this type of columns when vertical loads are combined with shear forces.

Appendix 1: Study 1 and Study 2 – Specimen Preparation, Instrumentation and Test Setup

Column specimens were cast at a precast plant located in Miami (Fig. A - 1) and let cure at the South Campus of the University of Miami (Fig. A - 2).

The GFRP bar cages (Study 1) were assembled at the Structural Laboratory of the Civil, Architectural and Environmental Engineering of the University of Miami (Fig. A - 3).

Confined column specimens (Study 2) were prepared at the South Campus of the University of Miami (Fig. A - 4 through Fig. A - 7).

Fig. A - 8 through Fig. A - 11 sketch the position of the LVDTs and the location of the internal strain gauges.

Photographs documenting testing equipments, test preparation and finale test setup are shown in Fig. A - 12 through Fig. A - 15.



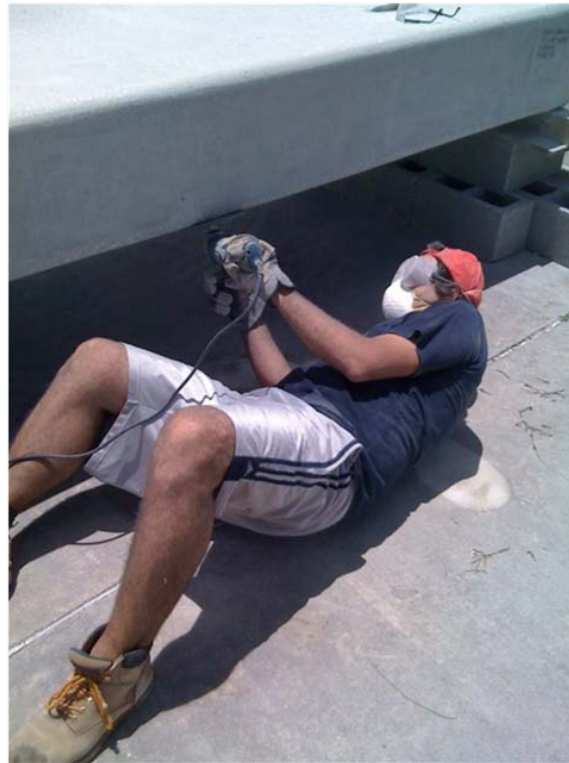
Fig. A - 1: Casting of a specimen.



Fig. A - 2: Cured specimens.



Fig. A - 3: Preparation of the GFRP cages (a-d).



a)



b)



c)

Fig. A - 4: Chamfering of the corners: grinding of the corner (a); corner before chamfering (b); corner after chamfering (c).



a)



b)



c)



d)

Fig. A - 5: Wrapping of the column specimens: cutting of the fiber sheet (a); installation of the fiber sheet (b-d).



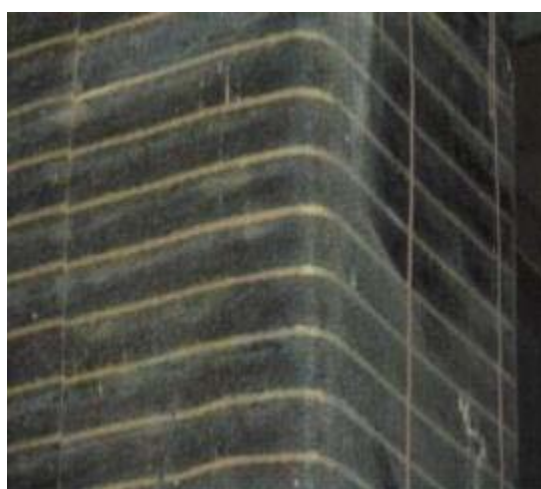
Fig. A - 6: Specimen preparation.



a)



b)



c)

Fig. A - 7: Type of fibers: Glass A (a); Glass B (b); Hybrid (c).

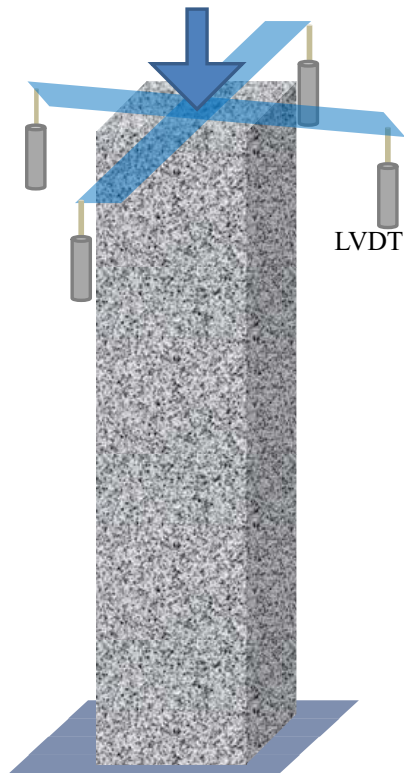


Fig. A - 8: Sketch illustrating the position of the vertical LVDTs (all specimens in Study 1 and Study2).

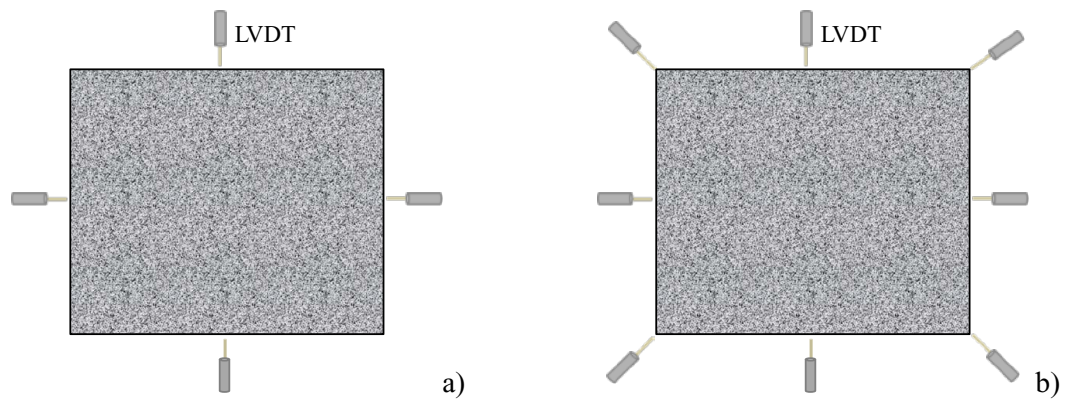


Fig. A - 9: Sketch illustrating the position of the horizontal LVDTs: all specimens in Study 1 and control specimens in Study2 (a); confined specimens in Study 2 (b).

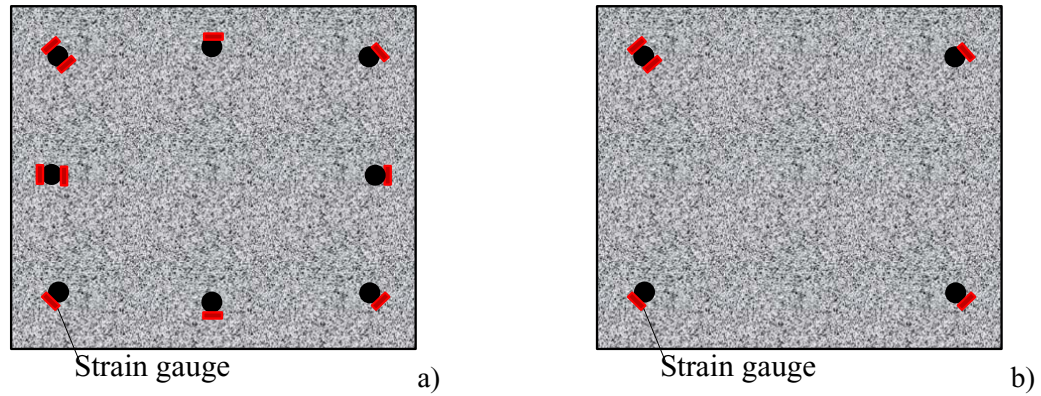


Fig. A - 10: Sketch illustrating the position of the strain gauges attached to the vertical bars at the level of the mid-height cross-section: all specimens in Study 1 and S-1 and R-1 specimens in Study2 (a); R-0.5 specimens in Study 2 (b).

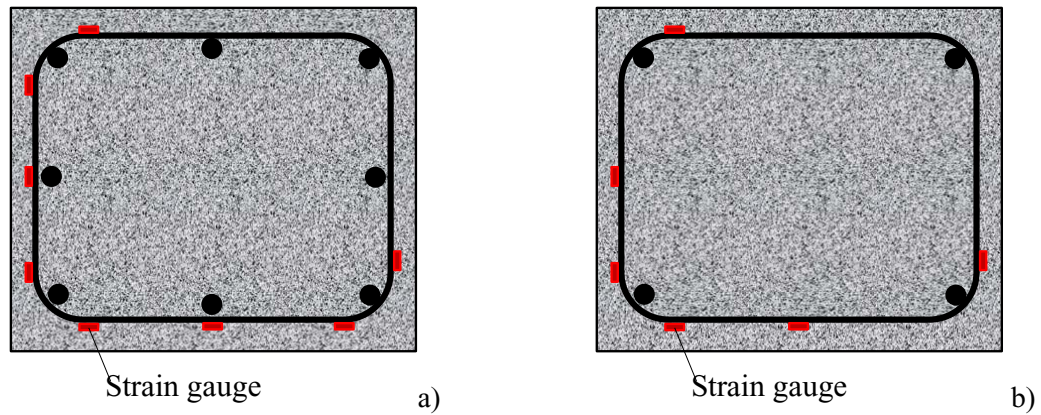


Fig. A - 11: Sketch illustrating the position of the strain gauges attached to the ties at the level of the mid-height cross-section: all specimens in Study 1 and S-1 and R-1 specimens in Study2 (a); R-0.5 specimens in Study 2 (b).



Fig. A - 12: Testing equipment at the Fritz Laboratories.



a)



b)



c)



d)

Fig. A - 13: Test setup: column specimen centered in the machine (a); column specimen centered and plumbed (b); hydro-stoning of the bottom surface (c); hydro-stoning of the top surface (d).



Fig. A - 14: Testing equipment at the NIST Laboratories.



a)

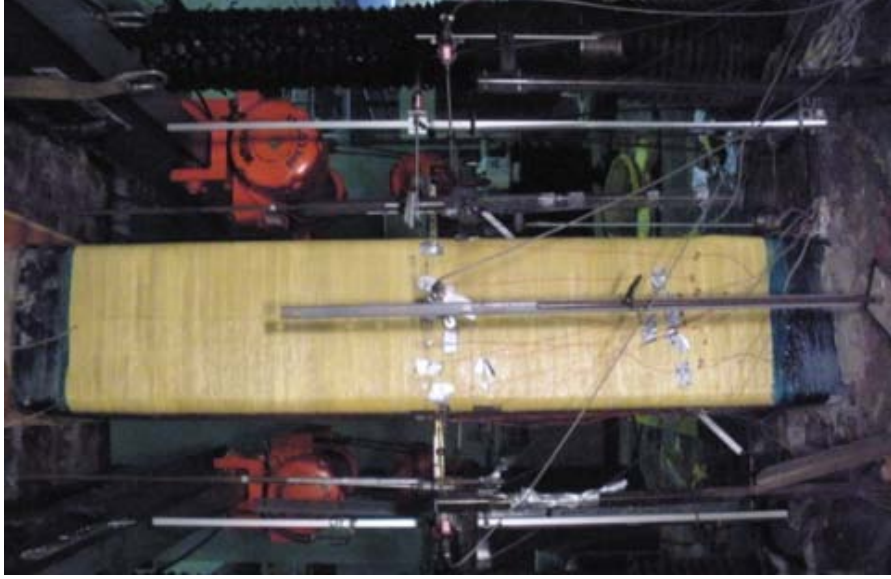


b)

Fig. A - 15: Test setup: grouting of top (a) and bottom (b) surface (NIST Laboratory).



a)



b)

Fig. A - 16: Final setup: Fritz Laboratory (a); NIST Laboratory (b).

Appendix 2: Study 1 – Photographs of Failed Specimens



a)



b)



c)



d)

Fig. A - 17: Failure of Specimen S-16 (a-d).



a)



b)



c)



d)

Fig. A - 18: Failure of Specimen A-12 (a-d).



a)



b)



c)



d)

Fig. A - 19: Failure of Specimen B-12 (a-d).



a)



b)



c)



d)

Fig. A - 20: Failure of Specimen A-3 (a-d).



a)



b)



c)



d)

Fig. A - 21: Failure of Specimen B-3 (a-d).

Appendix 3: Study 1 – News Releases

A press release in the University of Miami website covers the research presented in Study 1 (first link in the list shown below). Other links are listed as follows (2-10):

1. http://www.miami.edu/index.php/news/releases/why_reinforcing_concrete_columns_with_internal_bars_made_of_glass_fibers_can_make_a_building_sturdier/
2. http://www.engineersedge.com/technology_news/posts/812.html
3. <http://www.sciencedaily.com/releases/2009/07/090714165056.htm>
4. http://www.firstscience.com/home/news/breaking-news-all-topics/concrete-columns-with-internal-bars-made-of-glass-fibers-can-make-a-building-sturdier-page-2-1_67134.html
5. <http://www.sindhtoday.net/news/1/30860.htm>
6. <http://www.physorg.com/news166807178.html>
7. <http://scienceblog.com/cms/concrete-columns-internal-bars-made-glass-fibers-can-make-building-sturdier-23001.html>
8. http://pda.physorg.com/bars-concrete-columns_news166807178.html
9. http://www.eurekalert.org/pub_releases/2009-07/uom-ccw071409.php
10. <http://www.transtex.jp/gf/show/961> (in Japanese)

A paper on this research was presented at the 2009 American Composites Manufacturers Association “Composites & Polycon” conference and was also recognized as “Best Paper” in the “Infrastructure” category. Another paper was presented at the FRPRCS-9 Conference. A story was also published in the magazine *Concrete Technology Today*.

Appendix 4: Study 2 – Photographs of Failed Specimens



Fig. A - 22: Failure of Specimen S-1-control (a-c).



Fig. A - 23: Failure of Specimen S-1-5GA (a-c).



Fig. A - 24: Failure of Specimen S-1-2GB (a-d).



Fig. A - 25: Failure of Specimen S-1-8H (a-d).



Fig. A - 26: Failure of Specimen R-1-control (a-b).



Fig. A - 27: Failure of Specimen R-1-5GA (a-d).

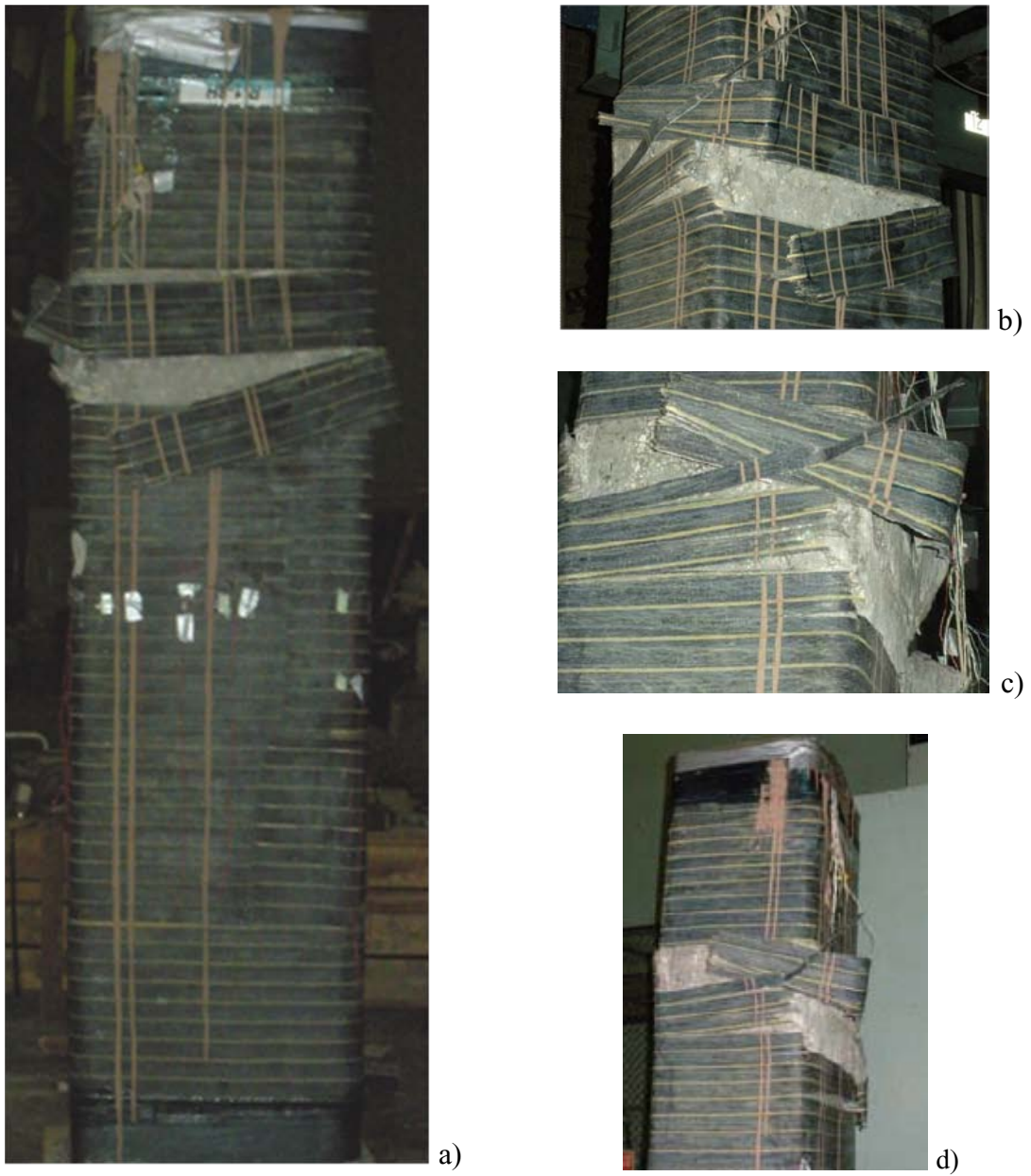


Fig. A - 28: Failure of Specimen R-1-8H (a-d).



Fig. A - 29: Failure of Specimen R-0.5-control (a-d).



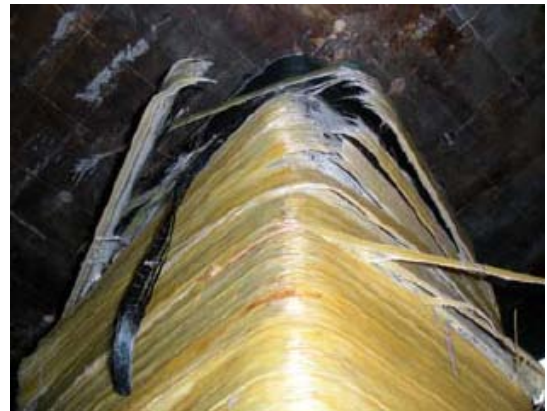
a)



b)



c)



d)

Fig. A - 30: Failure of Specimen R-0.5-5GA (a-d).



a)



b)



c)



d)

Fig. A - 31: Failure of Specimen R-0.5-2GB (a-d).



a)



b)



c)



d)

Fig. A - 32: Failure of Specimen R-0.5-5GB (a-d).



a)



b)



c)



d)

Fig. A - 33: Failure of Specimen R-0.5-8H (a-d).

Appendix 5: Study 3 – Example Algorithm

The algorithm used to calculate the ultimate concrete compressive strain is shown in this Appendix. The algorithm was implemented by using the software Mathematica 7.0 (Fig. A - 34 and Fig. A - 35).

```

Wolfram Mathematica 7.0 - [Conf - ultimate strainNEW.nb]
File Edit Insert Format Cell Graphics Evaluation Palettes Window Help

Conf - ultimate strainNEW.nb

epsConfPeak[alfa_] := -

$$\frac{0.0005}{-0.19999999999999996 + 0.075 \text{ alfa}}$$

sigConfPeak[alfa_] := -

$$\frac{0.15999999999999992 - 0.03500000000000002 \text{ alfa}}{-0.19999999999999996 + 0.075 \text{ alfa}}$$

epsCC = epsConfPeak[alfa]
sigCC = sigConfPeak[alfa]


$$\frac{0.0005}{-0.2 - 0.075 \text{ alfa}}$$


$$\frac{0.16 - 0.035 \text{ alfa}}{-0.2 - 0.075 \text{ alfa}}$$


Ec = 0.6 * fc / .00125
r = Ec / (Ec - sigCC * fc / epsCC)
sig[eps_] := fc * (eps / epsCC) * r * sigCC / (r - 1 + (eps / epsCC) ^ r)

480. fc

$$\frac{480. \text{ fc}}{480. \text{ fc} - 2000. (0.16 - 0.035 \text{ alfa}) \text{ fc}}$$


l = 24
fc = 5000
Et = 2 * .0232 * 10 500 000 * (3 * alfa)
epsP = epsConfPeak[alfa]
sigP = sigConfPeak[alfa]
DilationPeak =  $\frac{0.5}{\text{ alfa}}$ 
Poisson = 0.2
DilT =  $\frac{3 - \text{ alfa}}{4 * \text{ alfa}}$ 
DilDiag = (-0.5 * alfa ^ 2 + alfa - 0.01) / (alfa ^ 2)
epsLatMax[epsU_] := DilDiag * epsU + 2 * ((DilDiag - DilT) * epsU) ^ 2
epsLatMax[epsU]
epsLat[epsU_] := DilDiag * epsU + 8 / (1 ^ 2) * (x ^ 2) * ((DilDiag - DilT) * epsU) ^ 2
epsLat[epsU]

```

Fig. A - 34: Algorithm to calculate the ultimate concrete axial strain (Part 1 of 2).

```

Wolfram Mathematica 7.0 - [Conf - ultimate strainNEW.nb]
File Edit Insert Format Cell Graphics Evaluation Palettes Window Help

Conf - ultimate strainNEW.nb

24
5000
1.4616 × 106 alfa

$$\frac{0.0005}{-0.2 - 0.075 \text{ alfa}}$$


$$\frac{0.16 - 0.035 \text{ alfa}}{-0.2 - 0.075 \text{ alfa}}$$


$$\frac{0.5}{\text{alfa}}$$

0.2

$$\frac{3 - \text{alfa}}{4 \text{ alfa}}$$


$$\frac{0.01 - \text{alfa} - 0.5 \text{ alfa}^2}{\text{alfa}^2}$$


$$\frac{(0.01 - \text{alfa} - 0.5 \text{ alfa}^2) \text{ epsU}}{\text{alfa}^2} - 2 \left( -\frac{3 - \text{alfa}}{4 \text{ alfa}} - \frac{0.01 - \text{alfa} - 0.5 \text{ alfa}^2}{\text{alfa}^2} \right)^2 \text{ epsU}^2$$


$$\frac{(0.01 - \text{alfa} - 0.5 \text{ alfa}^2) \text{ epsU}}{\text{alfa}^2} - \frac{1}{72} \left( -\frac{3 - \text{alfa}}{4 \text{ alfa}} - \frac{0.01 - \text{alfa} - 0.5 \text{ alfa}^2}{\text{alfa}^2} \right)^2 \text{ epsU}^2 x^2$$


alfa = 1
epsU = 0.0425
r
Ec
(1^2) * Integrate[sig[eps], {eps, 0, epsU}] + 60000 * (0.01 * 1^2) * (epsU - 0.5 * 0.002) -
8 * Et * Integrate[(epsLat[epsU])^2, {x, 0, 1/2}]

1
0.0425
2.08696
2.4 × 106
-320.509

epsLatMax[epsU]
epsCC
sigCC
sigCC / (0.8)
Et
0.0216754
0.004
1.
1.25
1.4616 × 106

```

Fig. A - 35: Algorithm to calculate the ultimate concrete axial strain (Part 2 of 2).

Appendix 6: Study 2.1 – Structural Evaluation of GFRP-Confined Reinforced Concrete Hollow Columns

Background

Hollow-core concrete columns are an economically-attractive solution in concrete bridges to maximize the structural efficiency of the strength-mass and stiffness-mass ratios and to reduce the mass contribution of the column to seismic response and high carrying demand on foundations. To-date many concrete bridges incorporate hollow-core concrete piers particularly in areas where high seismic activity and natural boundaries require high-elevation infrastructures. However, modern codes of practice oriented to seismic design do not address any specific problem related to hollow sections. Many bridge hollow piers represented a threat in regions under high seismic risk due to insufficient shear or flexural strength, low ductility or inadequate seismic detailing and have been in need of retrofitting. Lately, retrofitting with fiber reinforced polymer (FRP) materials have become a valuable alternative to concrete or steel jackets as solution for strengthening, repairing and adding ductility with no significant increase of structural masses, no traffic disruption, rapid execution, long-term durability, and lower life-cycle costs (Karbhari and Zhao, 2000). Many studies have been carried out on FRP-confined reinforced columns (RC) circular and prismatic solid columns in the past years, and

several analytical models have been proposed. On the other hand, the behavior of FRP-jacketed RC hollow columns has been much less investigated.

A research by Osada et al. (1999) showed that the FRP jacket is capable of increasing the shear strength of the column and of avoiding premature buckling of longitudinal bars. Tests by Mo et al. (2004) showed that both ductility and shear strength can increase with the number of FRP sheets, preventing all shear cracks and changing the failure mode of the specimen from shear to flexure. Lignola et al. (2007a) investigated the behavior of square hollow columns subjected to flexure combined with compression and strengthened with CFRP wraps. Test outcomes proved that composite wrapping is able to enhance concrete strength and ductility and to delay premature mechanisms of failure such as compressed bar buckling and concrete cover spalling. Strength improvement was found to be more relevant in the case of specimens loaded with a small eccentricity, while ductility improvement was more relevant in case of bigger eccentricity. Lignola et al. (2007b) also discussed the behavior of unstrengthened and FRP-jacketed square hollow concrete piers subjected to combined axial load and flexure uncoupled from shear focusing on the analysis of cross-section curvature, member deformability, specific energy, and model restraints. Based on the above-cited studies, Lignola et al. (2009a) proposed a computation algorithm to model the nonlinear behavior of RC hollow columns confined with FRP.

The objective of this study was to understand how the presence of the external FRP confinement impacts column performance. Specifically, the effect of confinement was investigated with respect to strength and deformability enhancement, prevention of

instability of longitudinal bars, and confinement sensitivity to the confining reinforcement ratio.

Experimental program

The test matrix is designed considering different factors, summarized in Table A - 1: shape factor (side-aspect ratio), volume factor (volume-aspect ratio based on a benchmark volume of $24 \times 24 \times 120 \text{ in}^3$ [$0.61 \times 0.61 \times 3.05 \text{ m}^3$] solid column), type and amount of FRP sheet plies. The specimens are intended to represent scaled concrete piers designed according to dated codes (i.e., prior to 1970) for gravity loads only. Hollow column specimens are 120 in (3.05 m) in length with cross-sectional dimensions of 20 in by 29 in (508 by 737 mm) and a wall thickness of 4.5 in (114 mm). The total area of longitudinal bars was kept constant at 1.0% using eight No. 8 (25.4 mm diameter) bars. No. 4 (12.7 mm diameter) ties were used, spaced at 16 in. (406 mm) on center (which corresponds to the requirement to prevent bar buckling). Three specimens are considered: one unstrengthened RC column used as benchmark, and two columns confined with glass FRP (GFRP) reproducing a 5-ply and a 8-ply confinement ratio. The salient properties of the GFRP system are reported in Table A - 2.

Results and discussions

The control specimen failed abruptly due to longitudinal steel buckling and concrete cover splitting. Failure happened before the longitudinal steel reinforcement reached the yield point. Both the FRP-confined specimens failed due to rupture of the FRP jacket localized in a limited region in the proximity of a corner. The peak load was reached at a strain level close to yielding of the steel reinforcing bars. Cracking of the concrete progressed during the post-peak phase, while longitudinal bar buckling and concrete cover splitting were significantly restrained by the GFRP jacket. In Fig. A - 36, Fig. A - 37 and Fig. A - 38, the axial load is plotted versus the axial deformation for specimens HR-control, HR-5G and HR-8G, respectively. Photographs in Fig. A - 39a-c, Fig. A - 40a-b and Fig. A - 41a-b show the failed specimens.

The test results are summarized in Table A - 3. The following is reported: average concrete compressive strength, f_c ; maximum load applied to the column specimen, $F_{c,peak}$; average axial concrete stress (defined as the ratio between the maximum applied load and the gross cross sectional area), $\sigma_{c,peak}$; normalized axial stress (defined as the ratio between the average axial stress and the average concrete compressive strength), $(\sigma_{c,peak}/f_c)$; ratio between the average axial confined concrete stress with respect to the control specimen for the reference series, $(\sigma_{c,p}/\sigma_{c,pC})$; axial deformation at the peak load, $\Delta_{c,peak}$; post-peak axial deformation at failure, $\Delta_{c,max}$; ratio between the average axial stress at failure and the average concrete compressive strength; ratio between the post-peak axial deformation and the axial deformation at peak, $\Delta_{max}/\Delta_{c,peak}$. Fig. A - 42 also

shows the plot of the normalized axial stress with respect to the axial deformation for all the specimens.

No significant increment in concrete strength due to confinement has been observed. The normalized axial stress is 0.805 for the control specimen and varies between 0.832 and 0.864 for the confined ones. The increment in concrete strength due to confinement evaluated with the respect to the corresponding control specimen ranges between 3.3% and 7.3%. On the other hand, a significant improvement in post-peak deformability was experienced by the two confined specimens, as the ratio between axial deformation at failure and peak axial deformation is 2.90 and 3.23 for specimens HR-5G and HR-8G, respectively. Axial load at failure was about 72% and 65% the peak load for specimens WL-5G and WL-8G, respectively.

Table A - 1: Test matrix


Specimen code	Cross-section geometry	Internal steel reinforcement	Shape factor	Volume factor	Type of fibers	No. of plies
HR-control	 20'' by 29''	8 #8 longitudinal bars and #4 ties at a spacing of 16 in	1.45	0.61	benchmark specimen	5
HR-5G	corners chamfered with a radius of about 1 in				Glass	8
HR-8G					Glass	8

Table A - 2: GFRP system properties

Fiber type	Filament yarn properties			Laminate properties		
	Type of fibers	Tensile modulus (ksi)	Tensile strength (ksi)	Tensile strain (%)	Thickness (in)	Weight (lb/yd ²)
Glass fabric	E-Glass & high-performance Glass	11,160	493	4.7	0.0189	1.1

Note: 1 ksi = 6.895 MPa; 1 in = 25.4 mm; 1 lb/yd² = 0.542 g/m².

Table A - 3: Test results

Spec. ID	f_c [psi]	$F_{c,peak}$ [kips]	$\sigma_{c,peak}$ [psi]	$\sigma_{c,peak}/f_c$	$\sigma_{c,p}/\sigma_{c,pC}$	$\Delta_{c,peak}$ [in]	$\Delta_{c,max}$ [in]	σ_{cu}/f_c	$\Delta_{max}/\Delta_{c,peak}$
HR-control	6,236	1,775	5,018	0.805	---	0.220	0.233	0.795	1.06
HR-5G	6,439	1,897	5,366	0.832	1.033	0.248	0.720	0.529	2.90
HR-8G	6,773	2,070	5,859	0.864	1.073	0.200	0.646	0.616	3.23

Note: 1,000 psi = 6.895 MPa; 1,000 kip = 4,448 kN; 1 in = 25.4 mm.

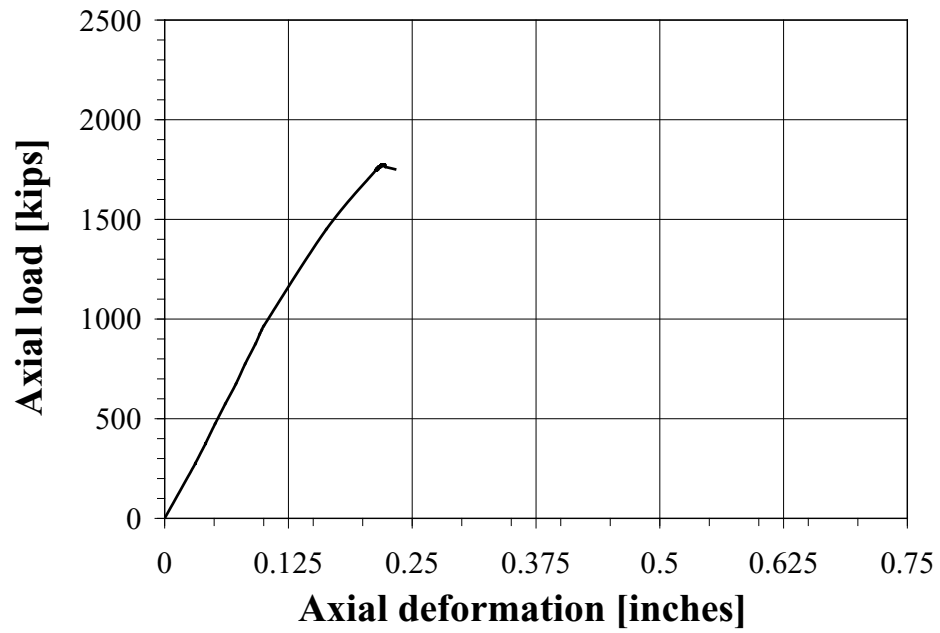


Fig. A - 36: Axial load vs. axial deformation diagram: Specimen HR-control.

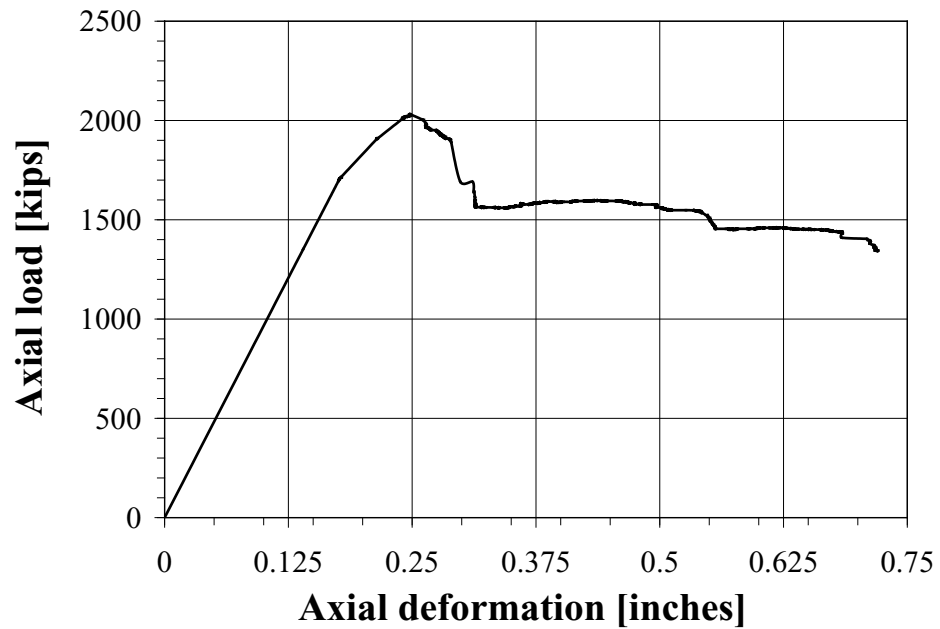


Fig. A - 37: Axial load vs. axial deformation diagram: Specimen HR-5GA.

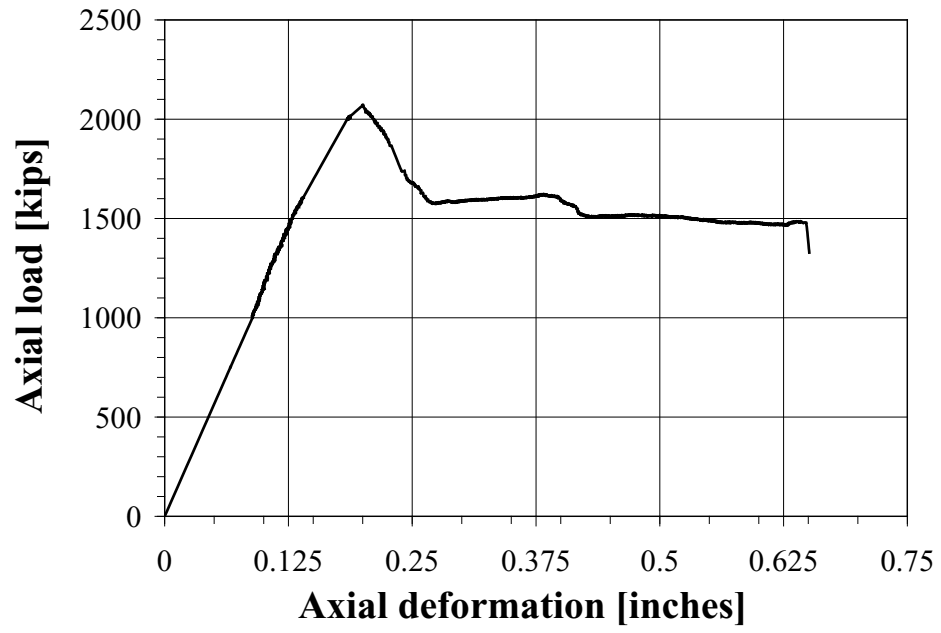


Fig. A - 38: Axial load vs. axial deformation diagram: Specimen HR-8GA.



Fig. A - 39: Photographs of failed Specimen HR-control (a-c).

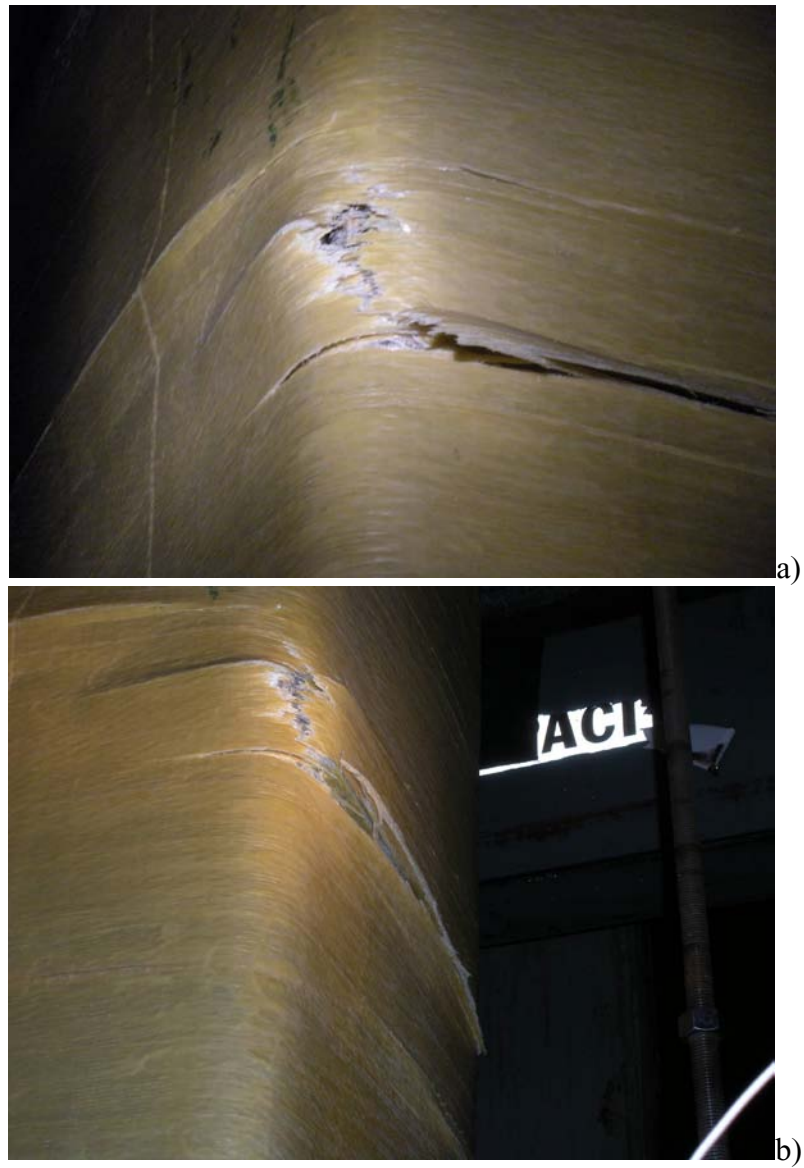


Fig. A - 40: Photographs of failed Specimen HR-5GA (a and b).



Fig. A - 41: Photographs of failed Specimen HR-8GA (a and b).

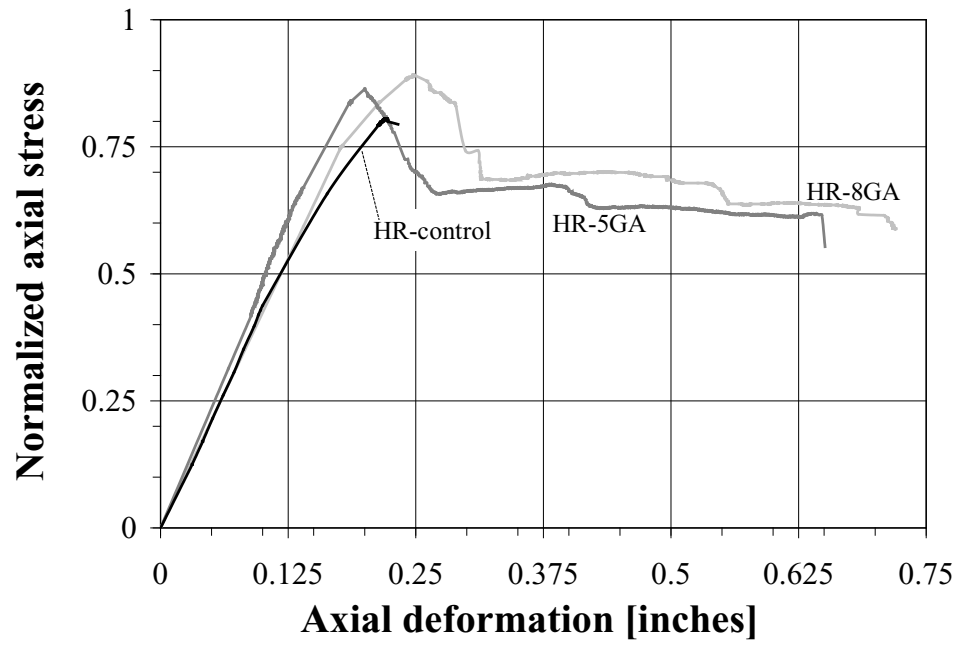


Fig. A - 42: Normalized axial stress vs. axial deformation response of all specimens.

Appendix 7: Study 2.2 – Structural Evaluation of GFRP-Confined Reinforced Concrete Wall-like Columns

Background

Dual wall-frame systems represent a solution often adopted in reinforced concrete (RC) earthquake resistant structures. When such structural solution is adopted, the capacity of the dual system is strongly dependent on the performance of the wall-like elements in compression. A prismatic column is defined as wall-like when the ratio between the two sides is higher than about 3.

Tanwongsvat et al. tested five wall-like RC columns having cross-section 4.5 in by 16.5 in (115 mm by 420 mm) and being 59 in (1.5 m) high; the longitudinal steel ratio was equal to 2.8%. Columns were externally bonded with GFRP laminates. Specimens with cross-section dimensions equal to the ones of the previous study were tested by Tan. Fifty-two RC columns were tested. The longitudinal steel ratio was equal to 2.2%. Both glass (GFRP) and carbon (CFRP) laminates with uni-directional fiber texture were used. Hosny et al. tested twelve RC rectangular columns with cross-section of 5.9 in by 17.7 in (150 mm by 450 mm) and height equal to 59 in (1.5 m). The longitudinal steel ratio was equal to 1%. The axially loaded members were confined using CFRP strips. Prota et al. tested a total of nine rectangular columns with cross-section 4.5 in by 16.5 in (115 mm by

420 mm), and height equal to 59 in (1.5 m). The longitudinal steel reinforcement ratio was equal to 2.2%. The columns were strengthened with GFRP laminates in the directions both parallel and perpendicular to the member axis. All these tests highlighted that FRP confinement could determine significant strength and ductility increases. However, the failure of FRP-confined wall-like columns is controlled by the shape of the cross-section and occurs at transverse strains in the jacket much lower than those ultimate of the fibers.

The main objectives of this study were: to define how the presence of the external FRP confinement impacts column strength and deformability enhancement; to evaluate whether the confinement is able to prevent and delay the instability of the longitudinal bars; and to understand the limitations of the confinement effectiveness due to the cross-sectional shape.

Experimental program

The test matrix is designed considering different factors, summarized in Table A - 4: shape factor (side-aspect ratio), volume factor (volume-aspect ratio based on a benchmark volume of $24 \times 24 \times 120 \text{ in}^3$ [$0.61 \times 0.61 \times 3.05 \text{ m}^3$] solid column), type and amount of FRP sheet plies. The specimens are intended to represent scaled concrete wall-like columns designed according to dated codes (i.e., prior to 1970) for gravity loads only. Column specimens are 120 in (3.05 m) in length with cross-sectional dimensions of 14 in by 41 in (356 by 1,041 mm). The total area of longitudinal bars was kept constant at

1.0% using eight No. 8 (25.4 mm diameter) bars. No. 4 (12.7 mm diameter) ties were used, spaced at 14 in. (356 mm) on center (which corresponds to the requirement to develop the maximum strength of the concrete core). Three specimens are considered: one unstrengthened RC column used as benchmark, and two columns confined with glass FRP (GFRP) reproducing a 5-ply and a 8-ply confinement ratio. The salient properties of the GFRP system are reported in Table A - 5.

Test results

The control specimen failed suddenly due to longitudinal steel buckling and concrete cover splitting. Failure happened after the longitudinal steel reinforcement reached the yield point. Both the FRP-confined specimens featured high axial deformations. They failed due to rupture of the FRP jacket localized in a limited region in the proximity of a corner. In Fig. A - 43, Fig. A - 44 and Fig. A - 45, the axial load is plotted versus the axial deformation for specimens WL-control, WL-5G and WL-8G, respectively. Photographs in Fig. A - 46a-c, Fig. A - 47a-b and Fig. A - 48a-b show the failed specimens.

The test results are summarized in Table A - 6. The following is reported: average concrete compressive strength, f_c ; maximum load applied to the column specimen, $F_{c,peak}$; average axial concrete stress (defined as the ratio between the maximum applied load and the gross cross sectional area), $\sigma_{c,peak}$; normalized axial stress (defined as the ratio between the average axial stress and the average concrete compressive strength),

$(\sigma_{c,peak}/f_c)$; ratio between the average axial confined concrete stress with respect to the control specimen for the reference series, $(\sigma_{c,p}/\sigma_{c,pC})$: axial deformation at the peak load, $\Delta_{c,peak}$; post-peak axial deformation at failure, $\Delta_{c,max}$; ratio between the average axial stress at failure and the average concrete compressive strength; ratio between the post-peak axial deformation and the axial deformation at peak, $\Delta_{max}/\Delta_{c,peak}$. Fig. A - 49 also shows the plot of the normalized axial stress with respect to the axial deformation for all the specimens.

No significant increment in concrete strength due to confinement was observed. On the other hand, a significant improvement in post-peak deformability was experienced by the two confined specimens, as the ratio between axial deformation at failure and peak axial deformation is 2.85 and 3.24 for specimens WL-5G and WL-8G, respectively. Axial load at failure was about 61% and 71% the peak load for specimens WL-5G and WL-8G, respectively.

Table A - 4: Test matrix

Specimen code	Cross-section geometry	Internal steel reinforcement	Shape Factor	Volume factor	Type of fibers	No. of plies
WL-control	□ 14" by 41"	8 #8 longitudinal bars and #4 ties at a spacing of 14 in	2.92	1.00	benchmark specimen	5
WL-5G	corners chamfered with a radius of about 1 in				Glass	8
WL-8G					Glass	8

Table A - 5: GFRP system properties

Fiber type	Filament yarn properties			Laminate properties		
	Type of fibers	Tensile modulus (ksi)	Tensile strength (ksi)	Tensile strain (%)	Thickness (in)	Weight (lb/yd ²)
Glass fabric	E-Glass & high-performance Glass	11,160	493	4.7	0.0189	1.1

Note: 1 ksi = 6.895 MPa; 1 in = 25.4 mm; 1 lb/yd² = 0.542 g/m²; in square brackets gross laminate properties.

Table A - 6: Test results

Spec. ID	f_c [psi]	$F_{c,peak}$ [kips]	$\sigma_{c,peak}$ [psi]	$\sigma_{c,peak}/f_c$	$\sigma_{c,p}/\sigma_{c,pC}$	$\Delta_{c,peak}$ [in]	$\Delta_{c,max}$ [in]	$\sigma_c(\Delta_{c,max})/f_c$	$\Delta_{max}/\Delta_{c,peak}$
IR-control	8,035	3,836	6,077	0.757	-	0.302	0.322	0.96	1.07
HR-5G	6,947	3,277	5,105	0.736	0.97	0.363	1.03	0.61	2.85
HR-8G	7,556	3,581	5,641	0.746	0.99	0.306	0.990	0.77	3.24

Note: 1,000 psi = 6.895 MPa; 1,000 kip = 4,448 kN; 1 in = 25.4 mm.

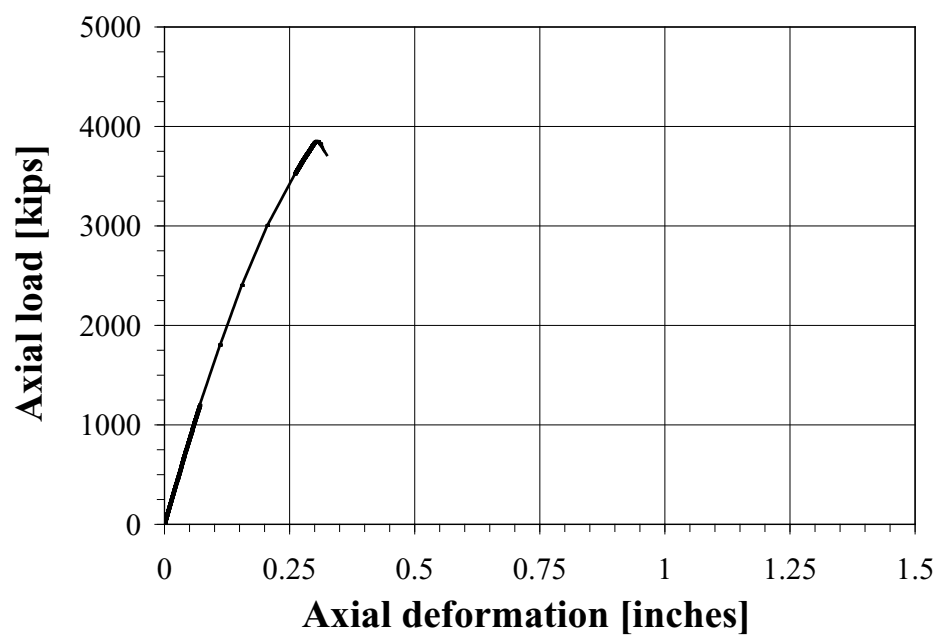


Fig. A - 43: Axial load vs. axial deformation diagram: Specimen WL-control.

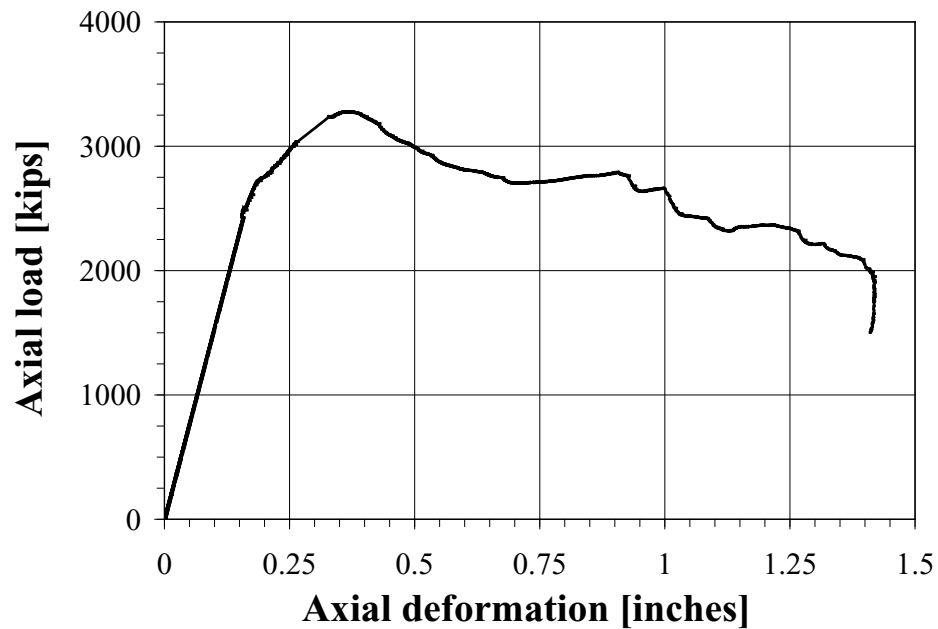


Fig. A - 44: Axial load vs. axial deformation diagram: Specimen WL-5GA.

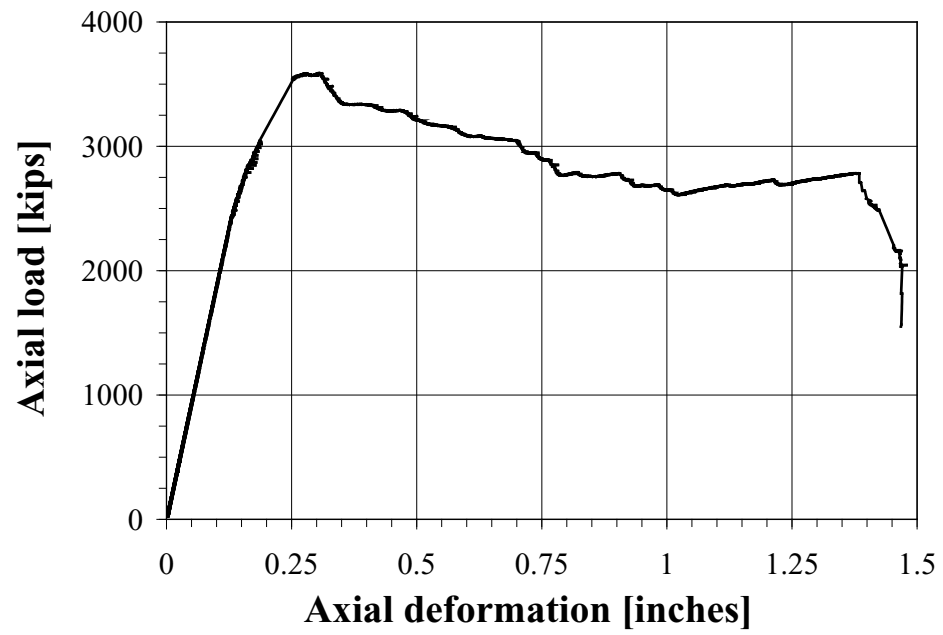


Fig. A - 45: Axial load vs. axial deformation diagram: Specimen WL-8GA.



a)



b)



c)

Fig. A - 46: Photographs of failed Specimen WL-control (a-c).



a)



b)

Fig. A - 47: Photographs of failed Specimen WL-5GA (a and b).



a)



b)

Fig. A - 48: Photographs of failed Specimen WL-8GA (a and b).

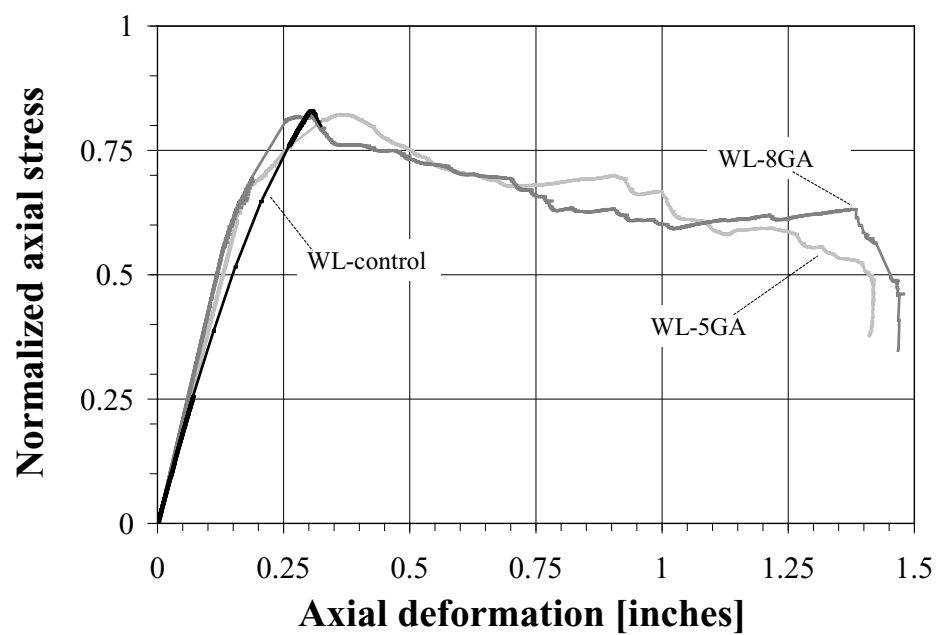


Fig. A - 49: Normalized axial stress vs. axial deformation response of all specimens.

Bibliography

1. Alsayed, S. H., Al-Salloum, Y. A., Almusallam, T. H., and Amjad, M. A, “Concrete Columns Reinforced by GFRP Rods.” *Fourth International Symposium on Fiber-Reinforced Polymer Reinforcement for Reinforced Concrete Structures* , SP-188, C. W. Dolan, S. H. Rizkalla, and A. Nanni, eds., American Concrete Institute, Farmington Hills, MI, 1999, pp. 103-112.
2. American Concrete Institute. (2008). “Building Code Requirements for Structural Concrete.” *ACI 318-08*, Farmington Hills, MI.
3. American Concrete Institute. (1963). “Building Code Requirements for Reinforced Concrete.” *ACI 318-63*, Detroit, MI.
4. American Concrete Institute. (2006). “Guide for the Design and Construction of Structural Concrete Reinforced with FRP Bars.” *ACI 440.1R-06*, Farmington Hills, MI.
5. American Concrete Institute. (2008). “Guide for the Design and Construction of Externally Bonded FRP Systems for Strengthening Concrete Structures.” *ACI 440.2R-08*, Farmington Hills, MI.
6. Bank, L.C. (2006). “Composites for Construction: Structural Design with FRP Materials.” *John Wiley & Sons*, New York, NY.
7. Bažant, Z. P. (1984a). “Size Effect in Blunt Fracture: Concrete, Rock, Metal.” *Journal of Engineering Mechanics*, ASCE, 110(4), 518–535.
8. Bažant, Z. P., and Kwon, Y. K. (1994). “Failure of Slender and Stocky Reinforced Concrete Columns: Tests of Size Effect.” *Materials and Structures*, 27, 79–90.
9. Bažant, Z. P., and Yavari, A. (2005). “Is the Cause of Size Effect on Structural Strength Fractal or Energetic-Statistical?” *Engineering Fracture Mechanics*, 72, 1–31.
10. Bresler, B., and Gilbert, P. H. (1961). “Tie Requirements for Reinforced Concrete Columns.” *Journal of the American Concrete Institute Proceedings*, 58(11), 555-570.

11. Campione, G., and Miraglia, N. (2003). "Strength and Strain Capacities of Concrete Compression Members Reinforced with FRP." *Cement and Concrete Composites*, 25, 31–41.
12. Canadian Standards Association. (2002). "Design and Construction of Building Components with Fibre-Reinforced Polymers." *CAN/CSA S806-02*, Mississauga, Ontario, Canada, 2002.
13. Carey, S. C., and Harries, K. A. (2005). "Axial Behavior and Modeling of Confined Small-, Medium-, and Large-Scale Circular Sections with Carbon Fiber-Reinforced Polymer Jackets." *ACI Structural Journal*, 102(4), 596-604.
14. Chen, W. F. (1982). "Plasticity in Reinforced Concrete." *McGraw Hill*, New York, NY.
15. Choo, C. C., Harik, I. E., and Gesund, H. (2006). "Minimum Reinforcement Ratio for Fiber-Reinforced Polymer Reinforced Concrete Rectangular Columns." *ACI Structural Journal*; 103(3), 460-466.
16. Fam, A. Z., and Rizkalla, S. H. (2001). "Confinement Model for Axially Loaded Concrete Confined by Circular Fiber-Reinforced Polymer Tubes." *ACI Structural Journal*, 98(4), 451–461.
17. Fardis, M. N., and Khalili, H. (1982). "FRP-Encased Concrete as a Structural Material." *Magazine of Concrete Research*, 34(121), 191–202.
18. Giangreco, E. (1969). "Teoria e Tecnica delle Costruzioni: Volume Terzo." *Liguori*, Napoli, IT.
19. Harajli, M. H. (2006). "Axial Stress-Strain Relationship for FRP Confined Circular and Rectangular Concrete Columns." *Cement and Concrete Composites*, 28(10), 938–948.
20. Harries, K. A., and Kharel, G. (2002). "Behavior of Variably Confined Concrete." *ACI Materials Journal*, 99(2), 180-189.
21. Hassan, M., and Chaallal, O. (2007). "Fiber-Reinforced Polymer Confined Rectangular Columns: Assessment of Models and Design Guidelines." *Journal of Composites for Construction*, 104(6), 693-702.
22. Hosny, A., Shaheen, H., Abdelrahman, A., Elafandy, T. (2002). "Uniaxial Tests on Rectangular Columns Strengthened with CFRP." *Proceedings of the Third Middle East Symposium on Structural Composites for Infrastructure Applications*, Aswan, Egypt.

23. Hsu, T. T. C., Slate, F. O., Sturman, G. M. and Winter, G. (1963). "Micro-cracking of Plain Concrete and the Shape of the Stress-Strain Curve." *ACI Journal, Proceedings*, 60(2), 209-224.
24. Hudson, F. M. (1966). "Reinforced Concrete Columns: Effects of Lateral Tie Spacing on Ultimate Strength." *Journal of the American Concrete Institute*, Special Publication, 13, 235-244.
25. Jiang, T., and Teng, J.G. (2007), "Analysis-Oriented Stress–Strain Models for FRP–Confined Concrete." *Engineering Structures*, 29, 2968-2986.
26. Karbhari, V. M., and Gao, Y. (1997). "Composite Jacketed Concrete under Uniaxial Compression—Verification of Simple Design Equations." *Journal of Materials in Civil Engineering*, 9(4), 185–193.
27. Karbhari, V. M., and Zhao, L. (2000). "Use of Composites for 21st Century Civil Infrastructure." *Computational Methods in Applied Mechanics and Engineering*, 185(2), 433–454.
28. Kaw, A. K. (2005). "Mechanics of Composite Materials (Second Edition)." *Taylor and Francis*, Boca Raton, FL.
29. Kumutha, R., Vaidyanathan, R., and Palanichamy, M. S. (2007). "Behaviour of Reinforced Concrete Rectangular Columns Strengthened using GFRP." *Cement and Concrete Composites*, 29(8), 609–615.
30. Kurt, C. E. (1978). "Concrete Filled Structural Plastic Columns." *Journal of the Structural Division*, 104(1), 55–63.
31. Lam, L., and Teng, J. G. (2003a). "Design-Oriented Stress-Strain Model for FRP-Confined Concrete." *Construction and Building Materials*, 17, 471–489.
32. Lam, L., and Teng, J. G. (2003b). "Design-Oriented Stress-Strain Model for FRP-Confined Concrete in Rectangular Columns." *Journal of Reinforced Plastics and Composites*, 22(13), 1149–1186.
33. Lignola, G.P., Prota, A., Manfredi, G., and Cosenza, E. (2007a). "Experimental Performance of RC Hollow Columns Confined with CFRP." *Journal of Composites for Construction*, 11(1), 42-49.
34. Lignola, G.P., Prota, A., Manfredi, G., and Cosenza, E. (2007b). "Deformability of RC Hollow Columns Confined with CFRP." *ACI Structural Journal*. 104(5), 629-637.

35. Lignola, G.P., Prota, A., Manfredi, G., and Cosenza, E. (2008). "Unified Theory For Confinement of RC Solid and Hollow Circular Columns." *Composites: Part B*, 39(7-8), 1151-1160.
36. Lignola, G.P., Prota, A., Manfredi, G., and Cosenza, E. (2009a). "Non Linear Modeling of RC Hollow Piers Confined with CFRP." *Composite Structures*, 88(1), 56-64.
37. Lignola, G.P., Prota, A., Manfredi, G., and Cosenza, E. (2009b). "Analysis Of Reinforced Concrete Hollow Square Piers Behavior: Benefits Of FRP Confinement." *International Journal of Advanced Structural Engineering* (ISSN 2008-3556), Islamic Azad University, South Tehran Branch, 1(1), 17-34.
38. Lyse, I., and Kreidler, L. (1932). "Fourth Progress Report on Column Tests at Lehigh University." *Journal of the American Concrete Institute Proceedings*, 28(1), 317-346.
39. Lyse, I. (1933). "Fifth Report on Column Tests at Lehigh University." *Journal of the American Concrete Institute Proceedings*, 29, 433-442.
40. Mallick, P. K. (1988). "Fiber Reinforced Composites Materials Manufacturing and Design." *Marcell Dekker, Inc.*, New York, 1988, 469.
41. MacGregor, J., G., and Wight, J., K. (2004). "Reinforced Concrete Mechanics and Design (4th Edition)." *Pearson Prentice Hall*, Upper Saddle River, NJ.
42. Mander, J.B., Priestley, M. J. N., and Park, R. (1988). "Theoretical Stressstrain Model for Confined Concrete." *Journal of Structural Engineering*, 114(8), 1804–1826.
43. Matthys, S., Toutanji, H., Audenaert, K., and Taerwe, L. (2005). "Axial Load Behavior of Large-Scale Columns Confined with Fiber-Reinforced Polymer Composites." *ACI Structural Journal*, 102(2), 258–267.
44. Mirmiran, A., and Shahawy, M. (1997). "Behavior of Concrete Columns Confined by Fiber Composite." *Journal of Structural Engineering*, 123(5), 583–590.
45. Mirmiran, A. (1998). "Length Effects on FRP-Reinforced Concrete Columns." *Proceedings of the 2nd International Conference on Composites in Infrastructure*, Tucson, AZ, 518-532.
46. Mirmiran, A., Shahawy, M., Samaan, M., El Echary, H., Mastrapa, J. C., and Pico, O. (1998b). "Effect of Column Parameters on FRP-Confined Concrete." *Journal of Composites for Construction*, 2(4), 175–185.
47. Mirmiran, A., Yuan, W., and Chen, X. (2001). "Design for Slenderness in Concrete Columns Internally Reinforced with Fiber-Reinforced Polymer Bars." *ACI Structural Journal*, 98(1), 116-125.

48. Mo, Y. L., and Yeh, Y.-K. (2004). "Seismic Retrofit of Hollow Rectangular Bridge Columns." *Journal of Composite for Construction*, 8(1), 43–51.
49. Nanni, A. (1993). "Flexural Behavior and Design of Reinforced Concrete Using FRP Rods." *Journal of Structural Engineering*, 119(11), 3344-3359.
50. Nanni, A., and Bradford, N. M. (1995). "FRP Jacketed Concrete under Uniaxial Compression." *Construction Building Materials*, 9(2), 115–124.
51. Nanni, A. (2001). "Relevant Applications of FRP Composites in Concrete Structures." *Proceedings Composites in Construction (CCC 2001)*, J. Figueiras, L. Juvandes and R. Furia, eds., (invited), Porto, Portugal, 661-670.
52. National Research Council CNR Advisory Committee on Technical Recommendations for Construction. (2006). "Guide for the Design and Construction of Concrete Structures with Fiber-Reinforced Polymer Bars." *CNR-DT 203/2006*, Rome, Italy.
53. Nemecek, J., and Bittnar, Z. (2004). "Experimental Investigation and Numerical Simulation of Post-Peak Behavior and Size Effect of Reinforced Concrete Columns." *Materials and Structures*, 37, 161- 169.
54. Osada, K., Yamaguchi, T., and Ikeda, S. (1999). "Seismic Performance and the Strengthening of Hollow Circular RC Piers Having Reinforced Cut-Off Planes and Variable Wall Thickness." *Concrete Research and Technology*, 10(1), 13–24.
55. Pantazopoulou, S. J., and Mills, R. H. (1995). "Microstructural Aspects of the Mechanical Response of Plain Concrete." *ACI Materials Journal*, 92(6), 605–616.
56. Pessiki, S., Harries, K. A., Kestner, J., Sause, R., and Ricles, J. M., "The Axial Behavior of Concrete Confined with Fiber Reinforced Composite Jackets." *Journal of Composites for Construction*, 5(4), 237-245.
57. Pfister, J. F. (1964). "Influence of Ties on the Behavior of Reinforced Concrete Columns." *Journal of the American Concrete Institute Proceedings*, 61(5), 521-536.
58. Prota, A., Manfredi, G., and Cosenza, E. (2006). "Ultimate Behavior of Axially Loaded RC Wall-Like Columns Confined with GFRP." *Composites: Part B*, 37, 670–678.
59. Richart, F. E., Brandtzaeg, A., and Brown, R. L. (1928). "A Study of the Failure of Concrete under Combined Compressive Stresses." *Engineering Experimental Station Bulletin No. 185*, Univ. of Illinois, Urbana, IL.
60. Richart, F., E. (1933). "Reinforced Concrete Column Investigation." *Journal of the American Concrete Institute Proceedings*, 29(2), 275-284.

61. Rocca, S., Galati, N., and Nanni, A. (2006). "Experimental Evaluation of FRP Strengthening of Large Size Reinforced Concrete Columns." *Center for Infrastructure Engineering Studies (CIES), Report No. 06-63*, Univ. of Missouri-Rolla, Rolla, MO.
62. Rocca, S., Galati, N., and Nanni, A. (2008). "Review of Design Guidelines for FRP Confinement of Reinforced Concrete Columns of Noncircular Cross Sections." *Journal of Composites for Construction*, 12(1), 80-92.
63. Saenz, N., and Pantelides, C. P. (2007). "Strain-Based Confinement Model for FRP-Confined Concrete." *Journal of Structural Engineering*, 133(6), 825–833.
64. Sener, S., Barr, B., I., G., and Abusiaf, H., F. (2004). "Size Effect in Axially Loaded Reinforced Concrete Columns." *Journal of Structural Engineering*, 130(4), 662-670.
65. Shehata, L. A. E. M., Carneiro, L. A. V., and Shehata, L. C. D. (2002). "Strength of Short Concrete Columns Confined with CFRP Sheets." *Materials and Structures*, 35, 50–58.
66. Slater, W. A., and Lyse, I. (1931). "First Progress Report on Column Tests at Lehigh University." *Journal of the American Concrete Institute Proceedings*, 27(2), 677-730.
67. Slater, W. A., and Lyse, I. (1931b). "Second Progress Report on Column Tests at Lehigh University." *Journal of the American Concrete Institute Proceedings*, 27(3), 791-835.
68. Slater, W. A., and Lyse, I. (1931c). "Third Progress Report on Column Tests at Lehigh University." *Journal of the American Concrete Institute Proceedings*, 28(11), 159-166.
69. Sonobe, Y., Fukuyama, H., Okamoto, T., Kani, N., Kimura, K., Kobatashi, K., Masuda, Y., Matsuzaki, Y., Mochizuki, S., Nagasaka, T., Shimizu, A., Tanano, H., Tanigaki, M., and Teshigawara, M. (1997b). "Design Guidelines of FRP Reinforced Concrete Building Structures." *ASCE Journal of Composites for Construction*, 1(3), 90-115.
70. Spoelstra, M. R., and Monti, G. (1999). "FRP-Confined Concrete Model." *Journal of Composites for Construction*, 3(3), 143-150.
71. Tan, K. H., (2002). "Strength Enhancement of Rectangular RC Columns using FRP." *Journal of Composites for Construction*, 6(3), 175–183.
72. Tanwongsva, S., Maalej, M., Paramasivam, P. (2003). "Strengthening of RC Wall-Like Columns with FRP under Sustained Loading." *Materials and Structures Journal*, 36(259), 282–290.

73. Teng, J. G., and Lam, L. (2004). "Behavior and Modeling of Fiber Reinforced Polymer-Confined Concrete." *Journal of Structural Engineering*, 130(11), 1713–1723.
74. Teng, J. G., Yu, T., Wong, Y. L., and Dong, S. L. (2007). "Hybrid FRP-Concrete-Steel Tubular Columns: Concept and Behavior." *Construction and Building Materials*, 21(4), 846–854.
75. Teng, J. G., Jiang, T., Lam, L., and Luo, Y. Z. (2009). "Refinement of a Design-Oriented Stress–Strain Model for FRP-Confined Concrete." *Journal of Composites for Construction*, 13(4), 269–278.
76. Wang, Y. C., and Restrepo, J. I. (2001). "Investigation of Concentrically Loaded Reinforced Concrete Columns Confined with Glass Fiber-Reinforced Polymer Jackets." *ACI Structural Journal*, 98(3), 377–385.
77. Wu, H. L., Wang, Y. F., Yu, L., Li, X. R. (2009). "Experimental and Computational Studies on High-Strength Concrete Circular Columns Confined by Aramid Fiber-Reinforced Polymer Sheets." *Journal of Composites for Construction*, 13(2), 125–134
78. Wu, W. P. (1990). "Thermomechanical Properties of Fiber Reinforced Plastic (FRP) Bars." *PhD dissertation*, West Virginia University, Morgantown, WV.